TOPICS IN THE ANALYSIS, MEASUREMENT, AND DESIGN

OF HIGH-PERFORMANCE SWITCHING REGULATORS

Thesis by

Arthur Raymond Brown

In Partial Fulfillment of the Requirements

for the Degree of

Doctor of Philosophy

California Institute of Technology

Pasadena, California

1981

(Submitted May 15, 1981)

to my parents

ACKNOWLEDGMENTS

It is a pleasure for me to acknowledge here the help I have received from various persons and agencies during my stay at Caltech. My only regret is that many debts of gratitude which I owe must go unpaid; otherwise, the length of these acknowledgments would exceed that of the main text!

First, let me express my sincere appreciation and respect for my advisors, Professors R. D. Middlebrook and S. Ćuk. During my five years at Caltech, I have watched their Power Electronics Laboratory grow from a small group of people in a single room to a large, thriving research group supported by well-equipped laboratory facilities. Moreover, in spite of the demands which this growth has imposed on them, they have always been available when I have needed them. Their help and support have unquestionably been major factors in the successful completion of my studies.

Another factor has been my interaction with the various members of the power electronics research group. Through discussions and seminars they have greatly enriched my learning experience. In addition, their enthusiasm and cooperation have made my research efforts both quicker and more productive. I shall miss these people.

I would also like to thank Mrs. Edith Huang and Miss Kiku Matsumoto for their valuable assistance in unraveling for me the mysteries of the computer system at Caltech. One result of their help is directly observable; this thesis was produced with the use of the word-processing facilities of the computer center.

For financial support I am indebted to the National Science Foundation for a fellowship grant, to the California Institute of Technology for several Teaching Assistantships, and to the International Business Machines Corporation and the

In a somewhat different vein, I want to express my gratitude to all of the people who, by their friendship, have made my stay here not only survivable but actually enjoyable. I shall remember all of you, both for the good times we have shared and for what you have taught me.

Finally, and most importantly, I would like to thank my parents, Franklin and Dorothy Brown. Throughout my life their support and encouragement have never wavered, even when the grounds for doubt were excellent. This debt is truly unpayable, and it is to them that this thesis is dedicated.

ABSTRACT

This thesis treats several issues in the analysis, measurement, and design of high-performance switching regulator systems. In Part I the high-frequency capabilities of two switching regulator modeling techniques, state-space averaging and discrete modeling, are compared, using the subharmonic instability in current-programmed regulators as a test. As a result of this comparison, a new small-signal, linear, time-invariant modeling technique, called *sampled-data modeling*, is developed. This new method retains the continuous form of state-space averaging but also possesses the accuracy of discrete modeling, and thus it combines the best features of the two techniques.

In Part II the newly developed sampled-data modeling technique is applied to the question of the interpretation of loop gain measurements in high-performance switching regulators. As a result of the inaccuracy of state-space averaging near one-half the switching frequency, conventional loop gain predictions are found to be inadequate in this regime. Sampled-data analysis is employed to develop new theoretical predictions which closely match various kinds of loop gain measurements in high-performance systems.

Finally, in Part III attention is turned to a potential sensitivity problem in high-performance switching regulators. For systems whose bandwidths lie close to one-half the switching frequency, even small changes in the operating environment of the power converter may result in dramatic degradation of the system's dynamic characteristics. Formulas for the estimation of this sensitivity are developed, and adaptive control, in which feedback gains are functions of certain important circuit quantities, is proposed as a means of curing the problem. Several different adaptive control schemes are proposed, and the imple-

mentation and testing of two of these strategies demonstrate their superiority over a conventional, non-adaptive design.

TABLE OF CONTENTS

INTRODUCTION

In the practice of engineering, the development of a new product requires efforts in the three separate but complementary areas of design, analysis, and measurement. Design is the creative work of engineers; their charge is to construct devices whose performance levels extend beyond those previously available. Such design would be impossible, however, were it not for supporting analysis. Only by the modeling of a proposed design can it be determined that the desired specifications can be achieved. Equally important, once an implementation of a design is available, are measurement techniques to verify that the specified performance levels have indeed been attained. If the measurement results are not satisfactory, additional design is required, along with more analysis and measurements. Clearly, it is of paramount importance for the engineer to possess accurate and well-understood analysis and measurement techniques, so that this process can converge to a satisfactory conclusion, that is, the finished product. As a consequence, a good deal of engineering work is spent on the development of new methods and interpretations of analysis, measurement, and design.

The branch of engineering known as power electronics is no stranger to this pattern. Largely as a result of these new developments, switching power supplies supplies have been evolving steadily in recent years. This thesis is concerned with one aspect of this growth, namely, the quest for improved transient performance. More and more often, regulators are being required to respond rapidly and accurately to changing loads and sources. As is evident from the above discussion, analysis, measurement, and design techniques are all needed for the implementation of these systems. Accordingly, aspects of all of these subjects are treated in this work.

With some notable exceptions, previous analysis and measurement efforts have been directed at understanding the low-frequency behavior of switching converters. The frequency domain in the vicinity of one-half the switching frequency of the converter has been largely ignored. In the search for better transient response, however, this *high-frequency* regime takes on crucial importance, and therefore an understanding of this region becomes vital. Consequently, the principal emphasis in this thesis is placed on the high-frequency aspects of converters and regulators; low-frequency phenomena are largely ignored. Though this approach seems to be just the opposite of those of earlier modeling efforts, that appearance is not quite accurate: while low-frequency modeling techniques are generally found to be inadequate at high frequencies, the methods developed in this thesis are shown to possess excellent accuracy in both the high-and-low-frequency regimes.

In Part 1 of this thesis, a new modeling technique is developed for use in the high-frequency region. At first, the need for such a new model may not seem obvious, since several analysis techniques already exist. However, these techniques all have certain deficiencies. One existing method possesses a very convenient form and is very accurate at low frequencies, but possesses inadequate high-frequency accuracy. A second method has excellent accuracy at all frequencies, but the form of this model is different from that of the usual models employed by circuit engineers, and consequently this technique is somewhat inconvenient to use. The new model to be developed in this thesis combines the convenient form of the first existing method with the superior accuracy of the second, and forms a powerful tool in the investigation of the high-frequency behavior of switching regulators.

In the second part of this thesis, the new modeling technique developed in

Part I is applied to the question of the interpretation of switching regulator measurements. Again high-frequency phenomena are stressed. It is found that previously formulated predictions either do not agree with measurements at high frequencies or, although agreeing, are not accurate criteria for stability and performance. With the new modeling technique, accurate predictions for various high-frequency measurements are developed, and their significance in stability analysis is determined.

Part III of this thesis is concerned with a design problem which may arise when high-performance regulators are constructed. This undesirable behavior consists of an excessive dynamic sensitivity to changes in the regulator's operating conditions. In some cases, even a small change in the system's environment can result in instability. This part of the thesis deals, first, with quantifying this effect, to determine when it is a significant problem, and, second, with developing a design method to reduce this acute sensitivity. This new approach uses adaptive techniques to make the formerly constant feedback gains functions of certain crucial circuit quantities, thereby increasing the regulator's resistance to operating point changes.

The interdependence of analysis, measurement, and design, which was discussed at the beginning of this Introduction, can also be seen in the preceding description of this thesis. The goal of high performance regulators spurred the development of a new analysis technique which was both accurate at high frequencies and convenient to use. This technique was also used to correctly interpret measurements made on such regulators. However, an unforeseen side-effect, consisting of excessive converter sensitivity, was discovered which could have plagued the operation of these systems. A new design idea was required to correct this problem, and further analysis and measurements were needed to

confirm the cure. Thus, surprisingly, although the primary purpose of this thesis is to develop new techniques in order to aid engineers in their work, the thesis itself forms a microcosm of that same engineering process.

PART I

SAMPLED DATA MODELING

OF SWITCHING REGULATORS

CHAPTER 1

INTRODUCTION

Switching converters and regulators do not fall into the class of linear, time-invariant circuits to which accurate and straightforward analysis tools, such as the Laplace transform and the Nyquist plot, can be applied. A major goal in the study of these systems, therefore, has been the development of modeling techniques for these circuits. The efforts invested in this area have generally been fruitful, and several new analytical tools are now in use. Two of these methods are the state-space averaging technique of Ćuk [1] and the discrete modeling technique of Packard [2]. Both result in small-signal, linear models, and both make it possible to analyze and design switching converters and regulators. However, each of these methods has a drawback. State-space averaging, while possessing a very convenient continuous, time-invariant form and having been successful in many applications, is inaccurate when the frequencies of interest approach one-half the fundamental switching frequency of the converter. On the other hand, the discrete modeling technique, while very accurate, requires the abandonment of the usual continuous time model in favor of difference equations, which are unfamiliar to the circuit designer and do not reflect the continuous nature of the converter waveforms.

The purpose of this first part of this thesis is to introduce a new small-signal, linear modeling technique, which incorporates both the continuous form of the state-space averaged model and the accuracy of the discrete model. Called the sampled-data modeling technique, this new method also serves as a bridge between the two previously developed methods, allowing the differences between them to be uncovered and appraised. In this capacity the sampled-data model can serve to indicate when the accuracy of state-space averaging is sufficient for

the purposes of a design task and when its own greater power at high frequencies is required.

The development of this new method begins with a careful second look at the developments of the state-space averaging and the discrete modeling techniques. In Chapter 2 a general discussion of switching converters and regulators is presented. In addition, a particular form of regulation known as current-programming is introduced. This control scheme possesses a well-defined, high-frequency instability, which makes its analysis useful as a test of the high-frequency capabilities of modeling methods. In Chapter 3, which is adapted from Packard [2], a series of equation manipulations is presented which can be used as the foundations for the development of both the state-space averaging and the discrete modeling techniques. The steady-state characteristics of switching converters are also discussed in this chapter.

Building on the base provided by Chapter 3, Chapter 4 proceeds to develop the state-space averaging method, noting with care all assumptions used. Both converter and regulator analysis are treated. Then an application of this technique to the current-programming scheme confirms the inaccuracy of state-space averaging at high frequencies, for the model fails to predict the instability inherent in current-programmed regulators. In Chapter 5 these steps of development and testing are repeated for the discrete modeling technique, showing that this method does possess accuracy at high frequencies.

With the insight obtained from the previous chapters, the creation of the new sampled-data modeling technique is undertaken in Chapter 6. While similar to the development of state-space averaging, the present derivation avoids an unjustified approximation used in the development of that model, and so results in a more accurate, yet still continuous and linear model. The increased

accuracy is seen in the ability of the sampled-data technique to predict correctly the occurrence of instability in a current-programmed regulator.

In Chapter 7 a detailed discussion of the sampled-data method is presented, emphasizing its similarities and differences with both state-space averaging and the discrete modeling technique and displaying some general properties of its loop gain. Sampled-data modeling and discrete modeling are seen to be essentially equivalent representations of the same process, although in any given case one representation may be more convenient to use than the other. On the other hand, the sampled-data and state-space averaged models are seen to differ solely in the presence of a sampler in the new model. Physical and mathematical relationships are developed which show that the two methods agree at low frequencies; in fact, state-space averaging is seen to form a limiting case of the more powerful sampled-data technique. Consideration of the sampled-data loop gain reveals several properties of this function, characteristics which make its plotted form quite striking and which provide insight into the design process. Finally, conclusions are presented in Chapter 8.

CHAPTER 2

FUNDAMENTALS OF SWITCHING REGULATORS

AND CURRENT-PROGRAMMING

2.1 Introduction

This chapter serves to introduce some of the basic principles which are used in this thesis. In Section 2.2 the fundamentals of switching regulators are reviewed. First, the four basic switching converters are introduced. Consideration of the operation of these circuits then leads to a realization of a common feature in their design, a feature which turns out to have extensive ramifications, via the *straight-line* approximation, for the analysis of these converters. After this discussion, the use of feedback to regulate the output of a converter is summarized, and the implementation of such control schemes is described.

In Section 2.3 a particular control scheme is introduced which will be used extensively in this part of this thesis. This feedback arrangement, known as *current-programming*, is described and illustrated, and several of its features are listed. A drawback in the form of a potential instability is then revealed. This instability is the basis of the usefulness of the current-programming concept for this work as a test of the high-frequency accuracy of modeling techniques. Conclusions are presented in Section 2.4.

2.2 Switching regulator basics

The circuits discussed in this thesis have as their function the conversion of electrical energy from one dc voltage level to another with an efficiency approaching one hundred per cent. The word *switching* in their name arises

from their mode of operation, in which periodic changes in circuit topology at a rate known as the switching frequency are caused to occur. This switching action converts the dc input into square waves, which are then filtered by low-pass networks, composed of inductors and capacitors, into a dc output.

Four basic switching converters are presented in Fig. 2.1. These circuits are shown both with ideal switches, to emphasize the principles of their operation, and with transistor and diode implementations of these switches. The simplest of the switching converters, the buck converter, is illustrated in Fig. 2.1a. The buck converter operates as a step-down voltage converter; the output voltage is always smaller than the input. This circuit operates by chopping the dc input and filtering the resultant square waves. Two other converters, shown in Figs. 2.1b and c, are known as the boost and buck-boost circuits, respectively. These converters operate by alternately storing energy from the source in an inductor and releasing that energy into a reservoir capacitor which feeds the load. The boost converter always steps up the input voltage, while the buck-boost circuit reverses the polarity of the input, with any desired scaling of the magnitude. The fourth converter, shown in Fig. 2.1d, is known, after its inventor, as the Ćuk converter and is a relatively recent development in this field [3]. It has the same output voltage polarity and magnitude as the buck-boost circuit, but possesses many advantages over that circuit and, indeed, over all of the other three topologies.

Although simple analyses treat the output voltages of switching converters as being purely dc, these waveforms are not actually constant. Along with the desired dc level there is also some ac ripple, consisting of frequency components at the switching frequency and higher. Clearly, for a converter to be a usable source of dc voltage, this high-frequency ripple must be much smaller than the
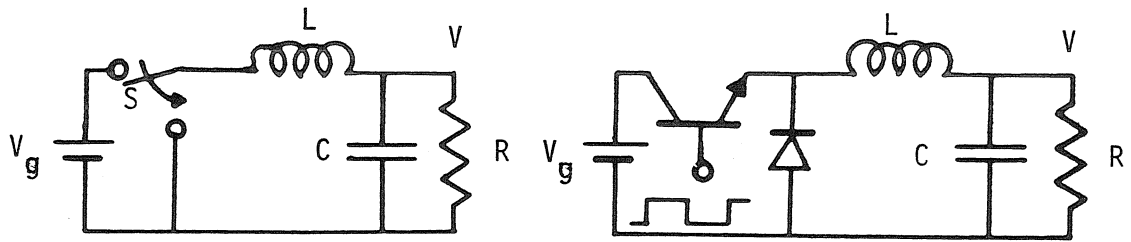
(a) buck converter
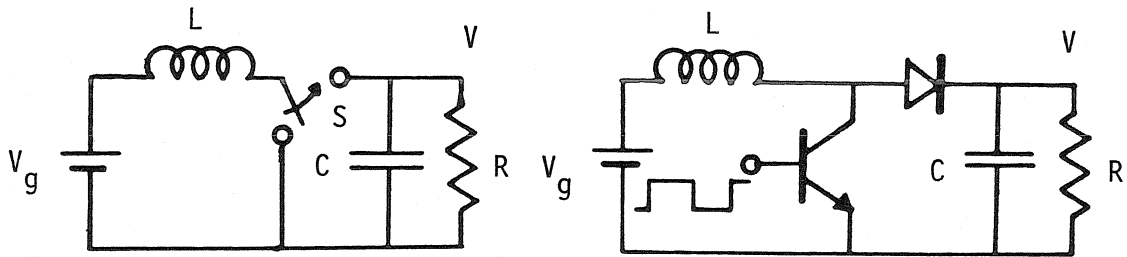
(b) boost converter
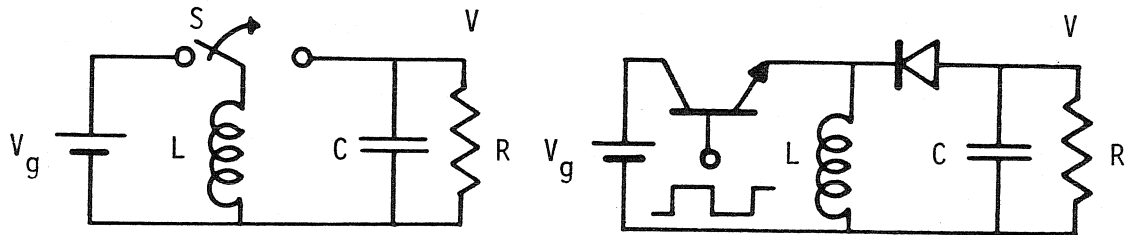
(c) buck-boost converter
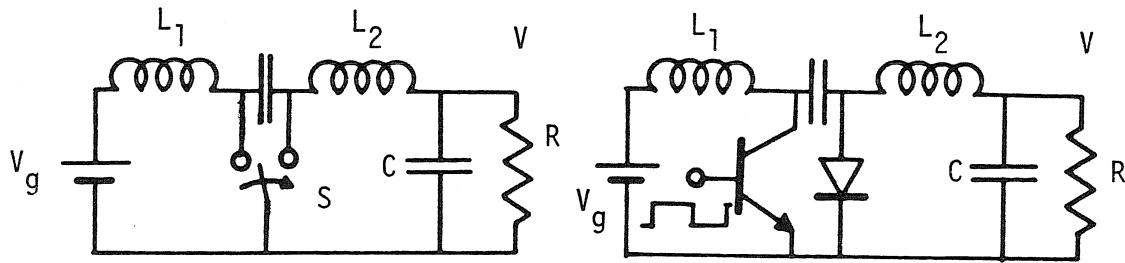
(d) Ćuk converter

Figure 2.1. *Four basic switching converters, presented with both ideal switches and transistor-diode implementations.*

dc component of the output. Since it is the job of the low-pass networks to attenuate these high-frequency components, this requirement means that the cutoff frequencies of these combinations of inductors and capacitors must be much less than the switching frequency.

This design rule has important and useful applications in the analysis of switching converters. Converter waveforms are generally exponential in form. However, since the time constants of the converter circuits are much longer than the switching period, the converter waveforms are always interrupted by a switching action before they can deviate significantly from linear shapes, as shown in Fig. 2.2. The algebraic equivalent of this characteristic is that the exponential matrices e^{At} which describe the evolution of these waveforms can be approximated, during the intervals of interest, by the first two terms of their Taylor series expansions.

$$e^{At} \approx I + At \, , \quad 0 < t < T_s \tag{2.1a}$$

$$A = \text{a converter state matrix} \tag{2.1b}$$

$$T_s = \text{the switching period} \tag{2.1c}$$

This approximation is commonly known as the straight-line approximation, alluding to the piecewise linearity of the converter waveforms, and is frequently used in converter analysis.

The timing of the switching instants helps to determine the output voltage of a converter. With the input voltage held fixed, variation of the on-time of the power transistor, variation of its off-time, or even variations of both can change the output voltage. Conversely, in a regulator, in which a constant output
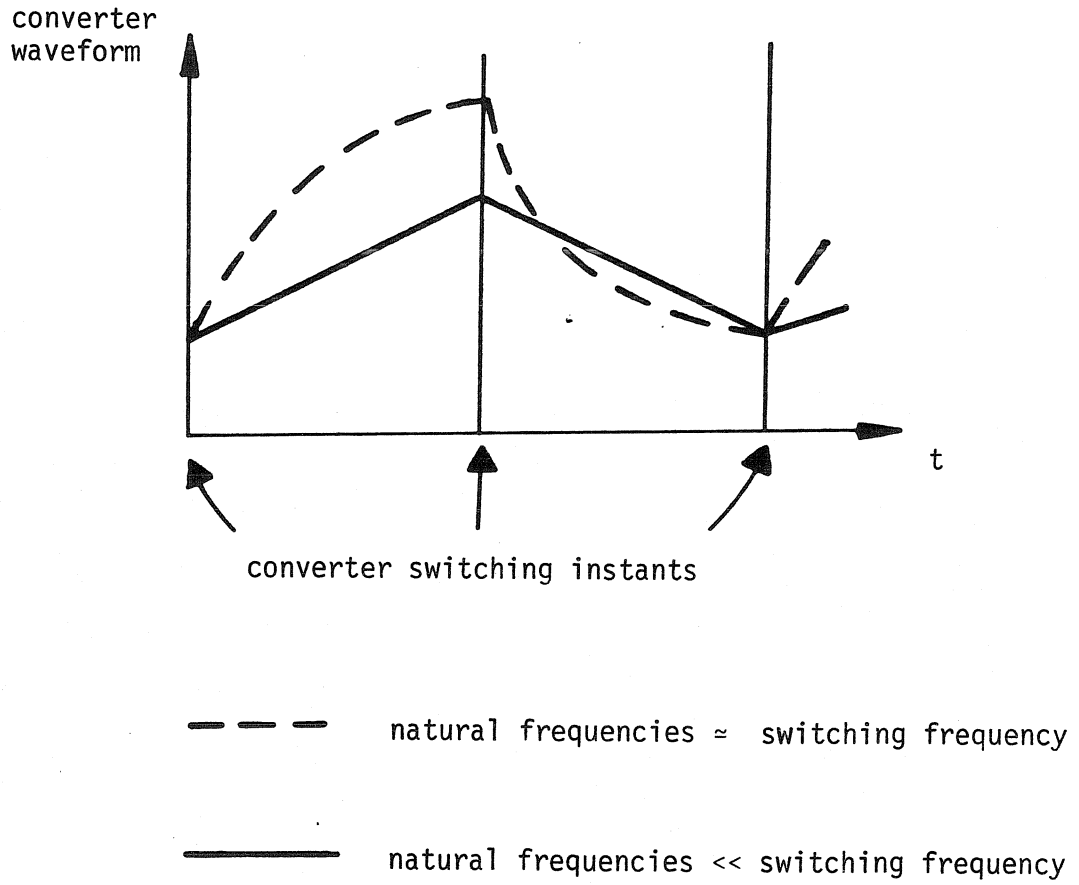
Figure 2.2. *Effect of sizes of natural frequencies relative to the switching frequency on the linearity of converter waveforms.*

voltage is desired, the timing of the switching instants is varied in a controlled manner so as to maintain a constant output in the face of a varying input. This thesis considers only the operating mode in which both the on-time and off-time of the power transistor are varied in such a manner that their sum, the switching period, remains constant. The ratio of the transistor on-time to the switching period is called the duty ratio, and control of the output voltage is said to be exercised through duty ratio modulation.

In a regulator, this duty ratio variation is accomplished through feedback: certain important quantities in the converter are monitored, and controller circuitry determines the appropriate duty ratio as a function of the measured quantities. In a general switching regulator controller, illustrated in Fig. 2.3, a combination of voltage and current measurements, possibly filtered, sampled, scaled by constant or variable gains, or otherwise processed, is subtracted from a reference value and then compared to an artificially generated ramp function to determine the duty ratio. The power transistor of the converter is turned on by a clock pulse at the same time that the ramp begins rising, and is turned off when the modulator signal v_m intersects the ramp. Note that the ramp need not necessarily be linear; in practice, however, a linear waveform is usually chosen. Note also that, owing to the presence of switching ripple, the modulator signal itself possesses a ramp-like shape. The slope of this signal, which acts exactly like an additional ramp waveform, may or may not be significant compared to the artificial ramp slope, depending on the details of a specific controller.

Feedback is clearly indispensable in the construction of a regulator. However, the introduction of feedback raises the problem of potential oscillations. Indeed, the goal of attainment of stable regulators with good transient charac-
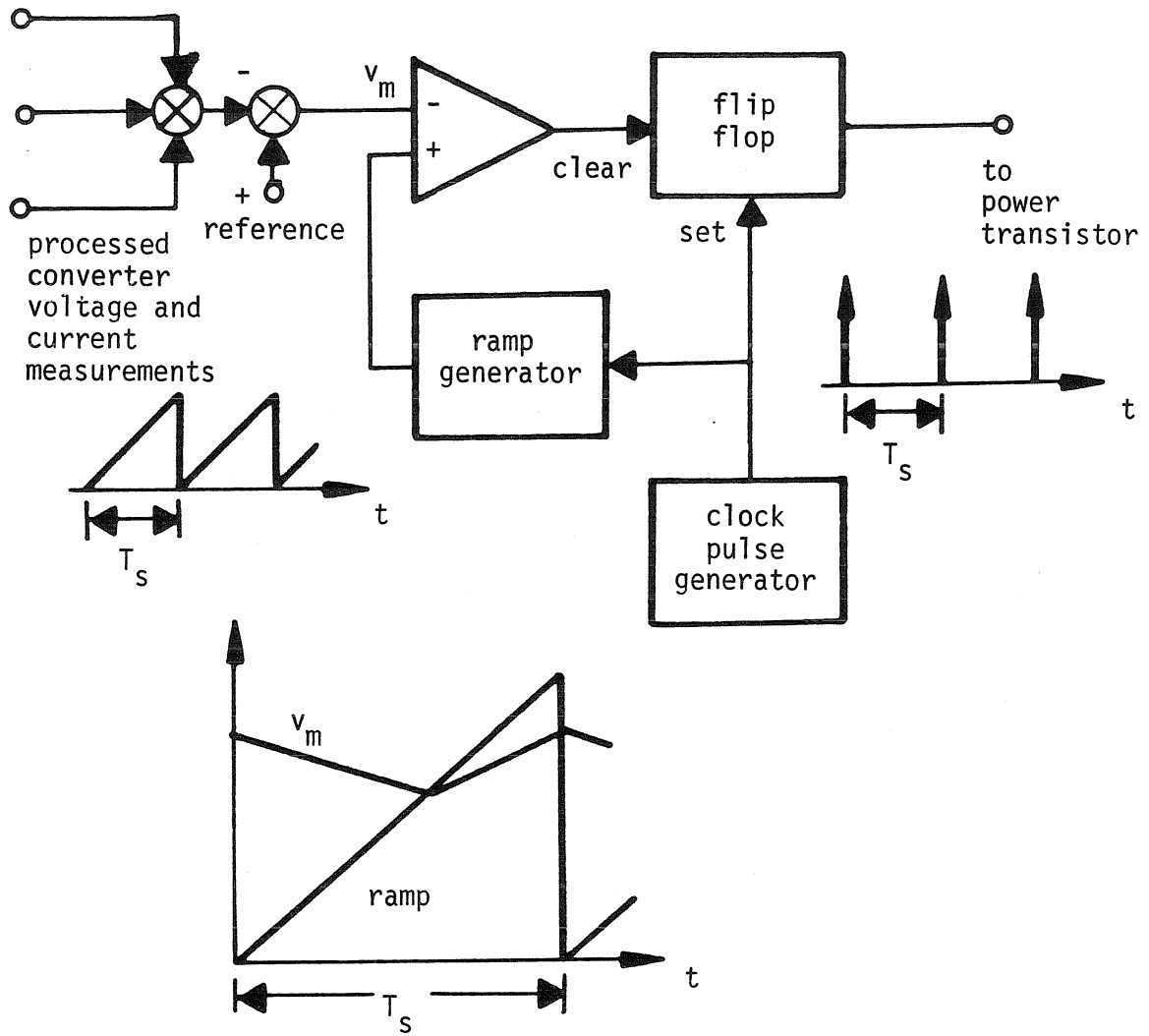
Figure 2.3. *General controller topology and waveforms.*

teristics has been the major motivation in the search for means to model switching converters. Hence, the modeling of controllers as well as of switching converters, and the combination of these models for purposes of regulator design, are all included in any reference to modeling and analysis of switching regulators.

2.3 Current-programming basics

Throughout Part I of this thesis, a method of feedback control known as current-programming will be used as a test of the various modeling techniques. This technique has been the subject of extensive research [4,5,6]. It is illustrated in Fig. 2.4, with use of a boost converter as an example, although the method can be applied to any converter. The controller in this figure is drawn in the same style as that in Fig. 2.3, in order to emphasize that the current-programming controller is a special case of that general controller. Specifically, it is a controller in which an inductor current is fed back and in which the slope of the artificially generated ramp is zero. Thus the only ramp-like slope is that of the switching ripple on the fed-back inductor current. Note that, as shown in Fig. 2.4, the current-programmed converter is not, in its basic form, a voltage regulator; to achieve regulation of the output voltage an additional signal derived from the output is fed back in parallel with the inductor current signal. Equivalently, and as is usually the case in practical systems, the output voltage feedback signal can be added to the reference.

A current-programmed converter has several features which make it quite attractive to designers. First, since the current of the turned-on power transistor is just the fed-back inductor current, a limit on the maximum value of the current reference automatically limits the transistor current, providing built-in
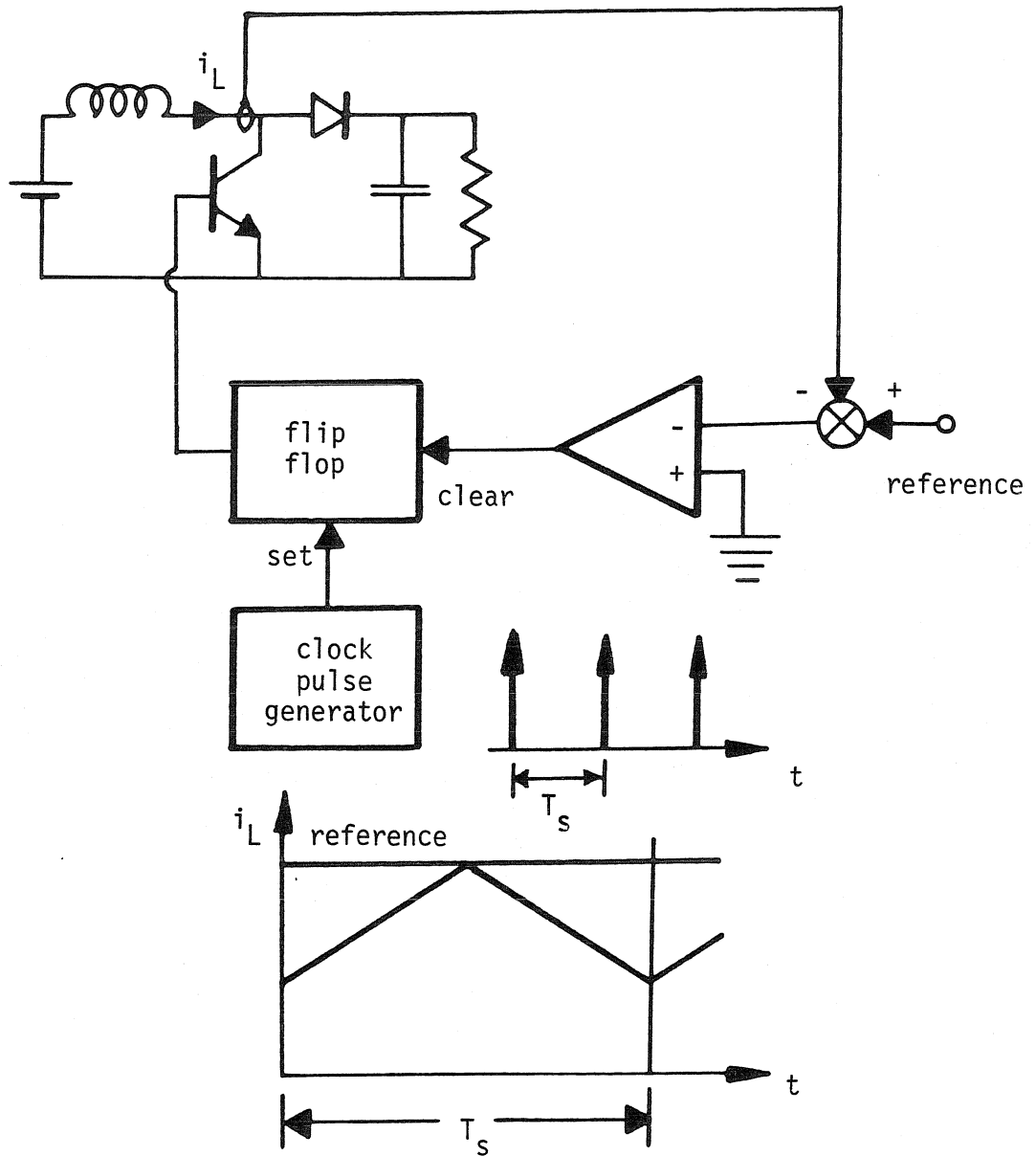
Figure 2.4. *Application of current-programming to a boost converter.*

protection. Second, several converters can be connected in parallel without any load-sharing problems by the establishment of a single, overall voltage feedback loop, with each component converter receiving the same current reference signal. Third, the low-frequency dynamic characteristic of a current-programmed converter possesses one less pole than the same converter without current-programming.

These three features have been studied extensively [4], and will not be discussed further here. Instead, another distinctly disadvantageous feature of current-programming will be used in this work. This characteristic is the uniform propensity of constant-frequency current-programmed converters to oscillate at one-half the switching frequency when the duty ratio of the power transistor attempts to exceed one-half [4]. Though this phenomenon has been discussed, its nature has seemed somehow different from other converter dynamic behavior, probably because the frequency of oscillation is so high. Usually the analysis of the instability is carried out separately, with different techniques, from low-frequency dynamic analysis [4].

An instability is an instability, however, and, whether at a low or a high frequency, its consequences are usually disastrous. Hence, an accurate modeling technique should provide predictions of both high-and-low-frequency dynamic behavior, including instabilities. The well-defined nature of the current-programming oscillation (occurring as it does in all the basic converters for duty ratios greater than one-half, at one-half the switching frequency) makes it a natural choice to serve as a test of the high-frequency capabilities of various modeling techniques.

2.4 Conclusions

In this chapter the fundamental concepts of switching regulators which will be used in this thesis were introduced. The four basic converters and their methods of operation were described, and the straight-line approximation, of great importance in converter design and analysis, was uncovered. The construction of regulators from switching converters was also discussed.

A particular kind of control scheme, known as current-programming, was then introduced, and some of its properties were noted. Among them, an instability associated with this feedback arrangement was described, and it was shown that this instability can be used as a high-frequency test of converter modeling methods.

CHAPTER 3

FUNDAMENTALS OF SWITCHING CONVERTER ANALYSIS.

3.1 Introduction

This chapter reviews a series of fundamental steps in the analysis of switching converters. In Section 3.2 a derivation adopted from Packard [2] is used to develop steady-state and small-signal differential equations for switching converters. The small-signal equation will be the starting point from which various modeling techniques are derived. Section 3.3 discusses the steady-state equation briefly, showing how the average values of the steady-state waveforms can be obtained without the solution of the differential equation. Finally, Section 3.4 presents conclusions.

3.2 Basic equations and analysis of switching converters

The analysis in this thesis will be carried out for the case of a constant-frequency switching regulator operating in the *continuous conduction* mode, in which no constraints on state variables are effective. Generally, in this operating mode, two different circuit topologies appear in the course of a complete switching cycle. Let $x(t)$ be the state vector, $v_g(t)$ the (nominally dc) source voltage, and T_s the switching period. Then such a converter is characterized by two state equations during a switching cycle.

$$\dot{x} = A_1 x + b_1 v_g \quad , \ nT_s < t < (n + d_n)T_s \tag{3.1a}$$

$$\dot{x} = A_2 x + b_2 v_g \quad , \ (n + d_n)T_s < t < (n + 1)T_s \tag{3.1b}$$

$$n = \dots, -1, 0, +1, \dots$$

Here A_1 and A_2 are square matrices which describe the two circuit topologies, and b_1 and b_2 are vectors that determine the effects of the source v_g. The duty ratio is represented by the fractional quantity d_n, $0 < d_n < 1$.

These two matrix equations can be combined into one by the definition of two switching functions, shown in Fig. 3.1.

$$d(t) = \begin{cases} 1 & \text{if } nT_s < t < (n + d_n)T_s \\ 0 & \text{if } (n + d_n)T_s < t < (n + 1)T_s \end{cases} \qquad (3.2a)$$

$$d'(t) = 1 - d(t) \qquad (3.2b)$$

With use of these functions, a single state equation suffices to describe the converter.

$$\dot{x} = [d(t)A_1 + d'(t)A_2]x + [d(t)b_1 + d'(t)b_2]v_g \qquad (3.3)$$

As a brief aside, consider the character of this equation. If d_n is a constant for all n, that is, if the converter is operated at constant duty ratio, without control, then Eq. (3.3) is a linear equation with periodic coefficients. If, on the other hand, control is exercised, with d_n a function of the state vector x and possibly v_g as well, then the equation becomes nonlinear.

Since control must be utilized in the design of a regulator, small-signal analysis must be used to obtain a linear equation. For this purpose, assume that the source consists of a dc quantity and a perturbation.

$$v_g(t) = V_g + \hat{v}_g(t) \qquad (3.4)$$

The notation used throughout this thesis is that dc or average values are represented by upper-case letters, and that perturbations are indicated by
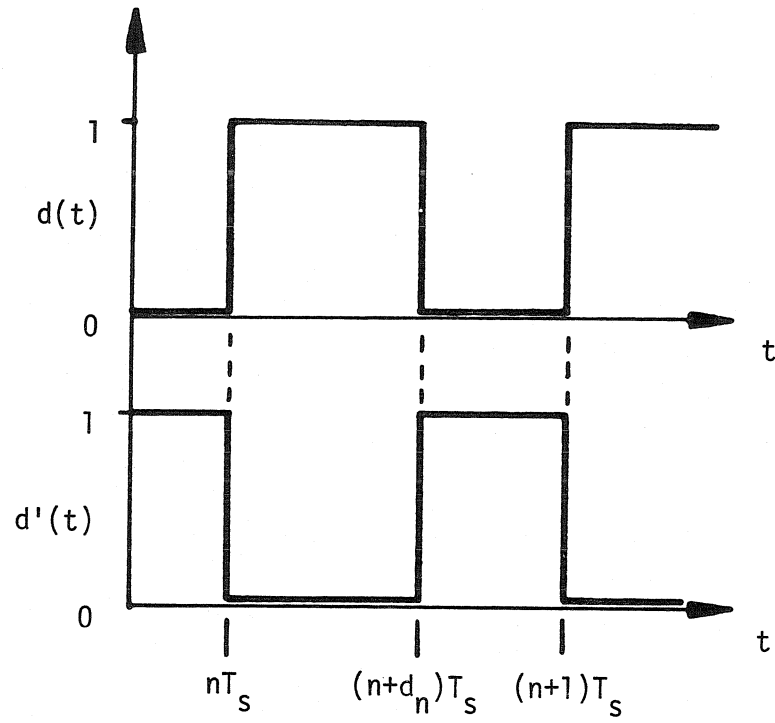
Figure 3.1. *Definitions of switching functions d(t) and d'(t).*

lower-case letters with carets. Similarly, suppose that the duty ratio consists of a constant plus a perturbation.

$$d_n = D + \hat{d}_n \tag{3.5}$$

Then the switching functions consist of a steady-state, time-varying part and a perturbation. In the notation used here, functions' steady-state forms, which may be time-varying, are denoted by bars.

$$d(t) = \overline{d}(t) + \hat{d}(t) \tag{3.6a}$$

$$d'(t) = 1 - d(t) \tag{3.6b}$$

$$\overline{d}(t) = \begin{cases} 1 & \text{if } nT_s < t < (n+D)T_s \\ 0 & \text{if } (n+D)T_s < t < (n+1)T_s \end{cases} \tag{3.6c}$$

$$\hat{d}(t) = \begin{cases} \text{sgn}(d_n - D) & \text{if } t \ \varepsilon \ [(n+D)T_s , \ (n+d_n)T_s] \\ 0 & \text{otherwise} \end{cases} \tag{3.6d}$$

$$\text{sgn}(y) = \begin{cases} +1 & \text{if } y > 0 \\ 0 & \text{if } y = 0 \\ -1 & \text{if } y < 0 \end{cases} \tag{3.6e}$$

These functions are illustrated in Fig. 3.2.

As a result of these perturbations, the state vector $x(t)$ will also consist of a steady-state, time-varying part (the state vector in the absence of perturbations) and a perturbation.

$$x(t) = \overline{x}(t) + \hat{x}(t) \tag{3.7}$$
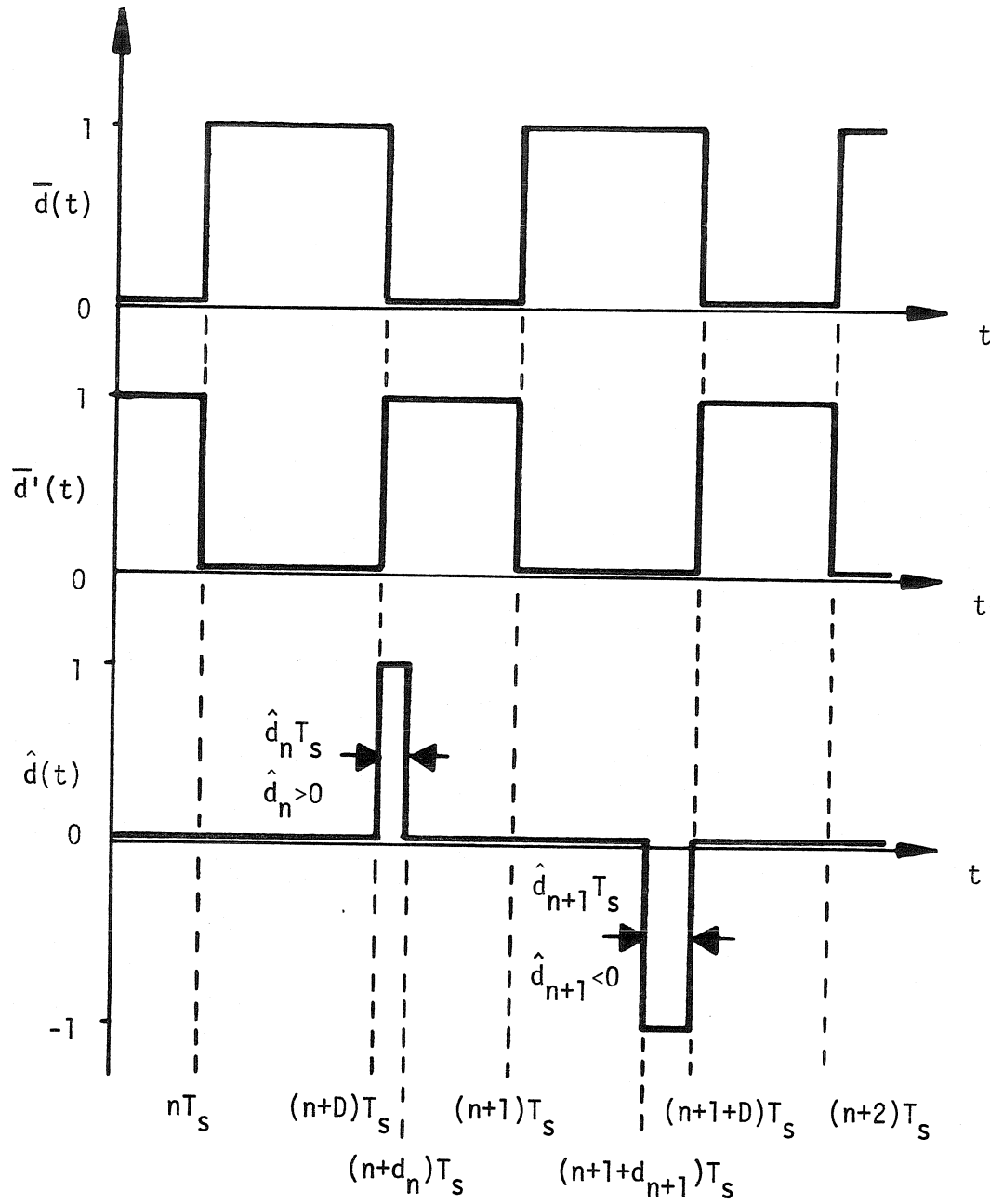
Figure 3.2. *Definitions of steady-state switching functions $\overline{d}(t)$ and $\overline{d}'(t)$, and of the perturbation $\hat{d}(t)$.*

These expansions are then substituted into the state equation, Eq. (3.3).

$$\dot{\overline{x}} + \dot{\hat{x}} = [(\overline{d} + \hat{d})A_1 + (\overline{d}' - \hat{d})A_2][\overline{x} + \hat{x}]$$

$$+ [(\overline{d} + \hat{d})b_1 + (\overline{d}' - \hat{d})b_2][V_g + \hat{v}_g] \qquad (3.8)$$

After collection of terms, the steady-state portion can be separated from the perturbation's influence.

$$\dot{\overline{x}} + \dot{\hat{x}} = [\overline{d}A_1 + \overline{d}'A_2]\overline{x} + [\overline{d}b_1 + \overline{d}'b_2]V_g$$

$$+ [\overline{d}A_1 + \overline{d}'A_2]\hat{x} + [\overline{d}b_1 + \overline{d}'b_2]\hat{v}_g$$

$$+ [(A_1 - A_2)(\overline{x} + \hat{x}) + (b_1 - b_2)(V_g + \hat{v}_g)]\hat{d} \qquad (3.9)$$

If there are no perturbations ($\hat{d}(t) = 0$, $\hat{v}_g(t) = 0$), the steady-state equation is obtained.

$$\dot{\overline{x}}(t) = [\overline{d}(t)A_1 + \overline{d}'(t)A_2]\overline{x}(t) + [\overline{d}(t)b_1 + \overline{d}'(t)b_2]V_g \qquad (3.10)$$

The subtraction of Eq. (3.10) from Eq. (3.9) results in an equation for the perturbation.

$$\dot{\hat{x}}(t) = [\overline{d}(t)A_1 + \overline{d}'(t)A_2]\hat{x}(t) + [\overline{d}(t)b_1 + \overline{d}'(t)b_2]\hat{v}_g(t)$$

$$+ [(A_1 - A_2)\overline{x}(t) + (b_1 - b_2)V_g]\hat{d}(t)$$

$$+ [(A_1 - A_2)\hat{x}(t) + (b_1 - b_2)\hat{v}_g(t)]\hat{d}(t) \qquad (3.11)$$

This equation is then linearized by the assumption that the perturbations are small enough that the products of perturbations in the final term make this quantity negligible compared to the other terms.

$$\dot{\hat{x}}(t) = [\overline{d}(t)A_1 + \overline{d}'(t)A_2]\hat{x}(t) + [\overline{d}(t)b_1 + \overline{d}'(t)b_2]\hat{v}_g(t)$$

$$+ [(A_1 - A_2)\overline{x}(t) + (b_1 - b_2)V_g]\hat{d}(t) \qquad (3.12)$$

Because of the small-signal restriction, the function $\hat{d}(t)$ now consists of a series of narrow pulses at the times $(n + D)T_s$, of height +1 if $\hat{d}_n > 0$ and -1 if $\hat{d}_n < 0$. This function is approximated very well by a string of delta functions of appropriate areas, as shown in Fig. 3.3.

$$\hat{d}(t) \approx \hat{p}(t) = \sum_{n=-\infty}^{\infty} \hat{d}_n T_s\, \delta[t - (n + D)T_s] \qquad (3.13a)$$

$$= \hat{u}(t)T_s \sum_{n=-\infty}^{\infty} \delta[t - (n + D)T_s] \qquad (3.13b)$$

Here $\hat{u}(t)$ is any continuous time function which matches $\hat{d}_n$ at the appropriate instants.

$$\hat{u}[(n + D)T_s] = \hat{d}_n \qquad (3.14)$$

While this function $\hat{u}(t)$ is not uniquely defined, its existence proves to be useful in controller modeling, where continuous converter waveforms are used to generate the duty ratio modulation. Note the resemblance of Eq. (3.13) to a sampling operation. This resemblance is exploited heavily in Chapter 6, in which a new modeling technique is developed.

The string of delta functions $\hat{p}(t)$ can now be substituted for $\hat{d}(t)$ in the small-signal state equation, Eq. (3.12).
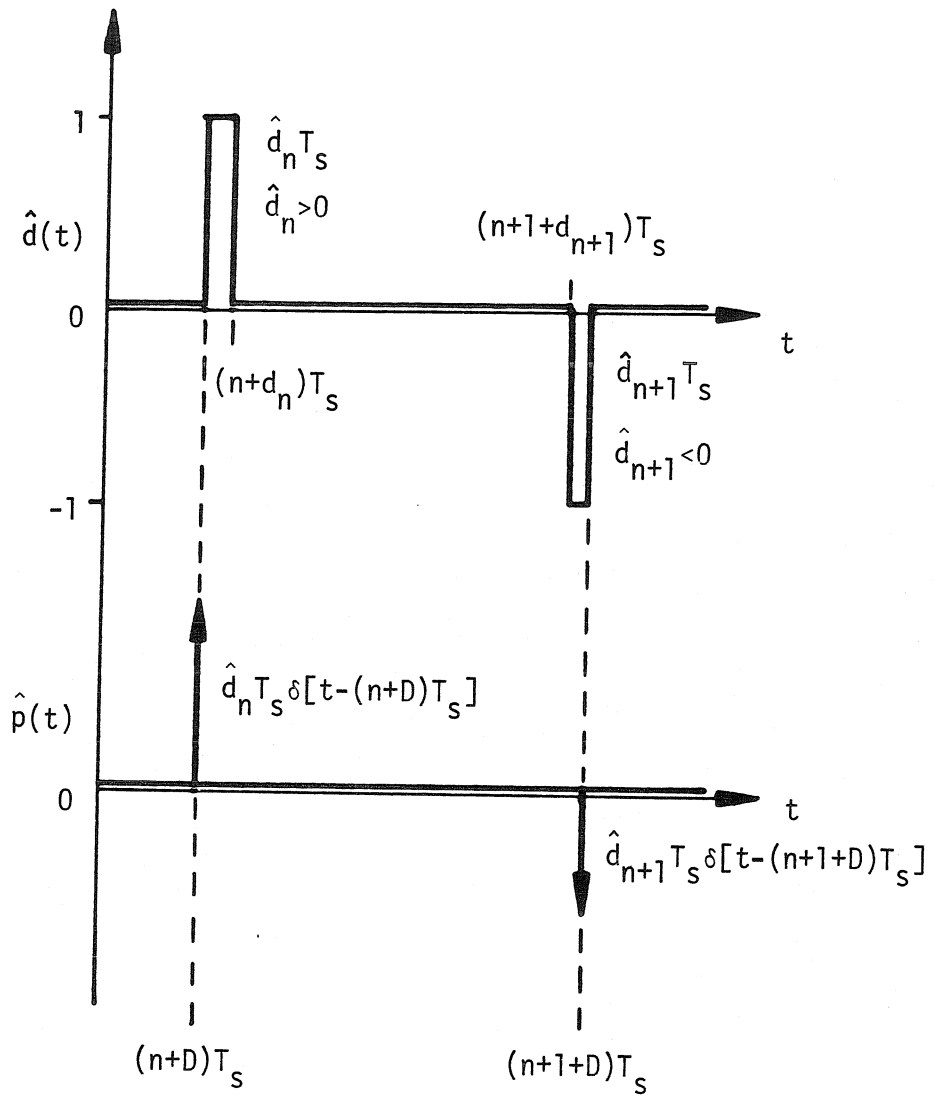
Figure 3.3. *Replacement of $\hat{d}(t)$ by the string of delta functions $\hat{p}(t)$.*

$$\dot{\overline{x}}(t) = [\overline{d}(t)A_1 + \overline{d}'(t)A_2]\hat{x}(t) + [\overline{d}(t)b_1 + \overline{d}'(t)A_2]\hat{v}_g$$

$$+ [(A_1 - A_2)\overline{x}[(n+D)T_s] + (b_1 - b_2)V_g]\hat{p}(t) \qquad (3.15)$$

The delta functions pick out only the value of $\overline{x}[(n+D)T_s]$ from $\overline{x}(t)$ in the final term. Because of the small-signal approximation, this equation is linear. However, it is definitely not time-invariant. Furthermore, it is driven by a string of delta functions. To obtain a useful result, further simplification is necessary. In succeeding chapters various means of simplification will result in the state-space averaging and discrete analysis techniques, as well as the new sampled-data modeling method.

3.3 Steady-state analysis of switching converters

Before an investigation of these derivations is undertaken, however, a digression will be made in order to consider the steady-state state equation, Eq. (3.10). This differential equation's steady-state, periodic solution represents the steady-state operation of the switching converter, including the switching ripple. However, information about the average values of the steady-state waveforms can be obtained more easily by use of the straight-line approximation discussed in Chapter 2.

Suppose Eq. (3.10) is integrated over one switching period, from time nT_s to time $(n+1)T_s$. The periodicity of the steady-state solution guarantees that the left-hand side of the equation vanishes.

$$\int_{nT_s}^{(n+D)T_s} \dot{\overline{x}}(t)dt = \overline{x}[(n+1)T_s] - \overline{x}[nT_s] = 0 \qquad (3.16)$$

The integration removes the time dependence from the right-hand side.

$$0 = A_1 \int_{nT_s}^{(n+D)T_s} \overline{x}(t)dt + A_2 \int_{(n+D)T_s}^{(n+1)T_s} \overline{x}(t)dt + (Db_1 + D'b_2)T_sV_g \quad (3.17a)$$

$$D' = 1 - D \qquad (3.17b)$$

The expression $(1 - D)$ occurs so frequently that it is assigned a special symbol, D'. The two integrals in Eq. (3.17) can be written in terms of time averages of $\overline{x}(t)$.

$$\int_{nT_s}^{(n+D)T_s} \overline{x}(t)dt = D T_s <\overline{x}>_1 \qquad (3.18a)$$

$$\int_{(n+D)T_s}^{(n+1)T_s} \overline{x}(t)dt = D'T_s <\overline{x}>_2 \qquad (3.18b)$$

Here $<\overline{x}>_1$ is the time average of $\overline{x}(t)$ during the interval $[nT_s, (n+D)T_s]$, and $<\overline{x}>_2$ is the time average of $\overline{x}(t)$ during the interval $[(n+D)T_s, (n+1)T_s]$. However, owing to the periodicity of the waveform and the straight-line approximation, as seen in Fig. 3.4, these two averages are the same. With the definition of this common value as the average state vector X, Eq. (3.17) can be rewritten.

$$X = <\overline{x}>_1 = <\overline{x}>_2 \qquad (3.19a)$$

$$0 = (DA_1 + D'A_2)T_sX + (Db_1 + D'b_2)T_sV_g \qquad (3.19b)$$

With some further definitions, a simple expression for the steady-state average state vector can be written.
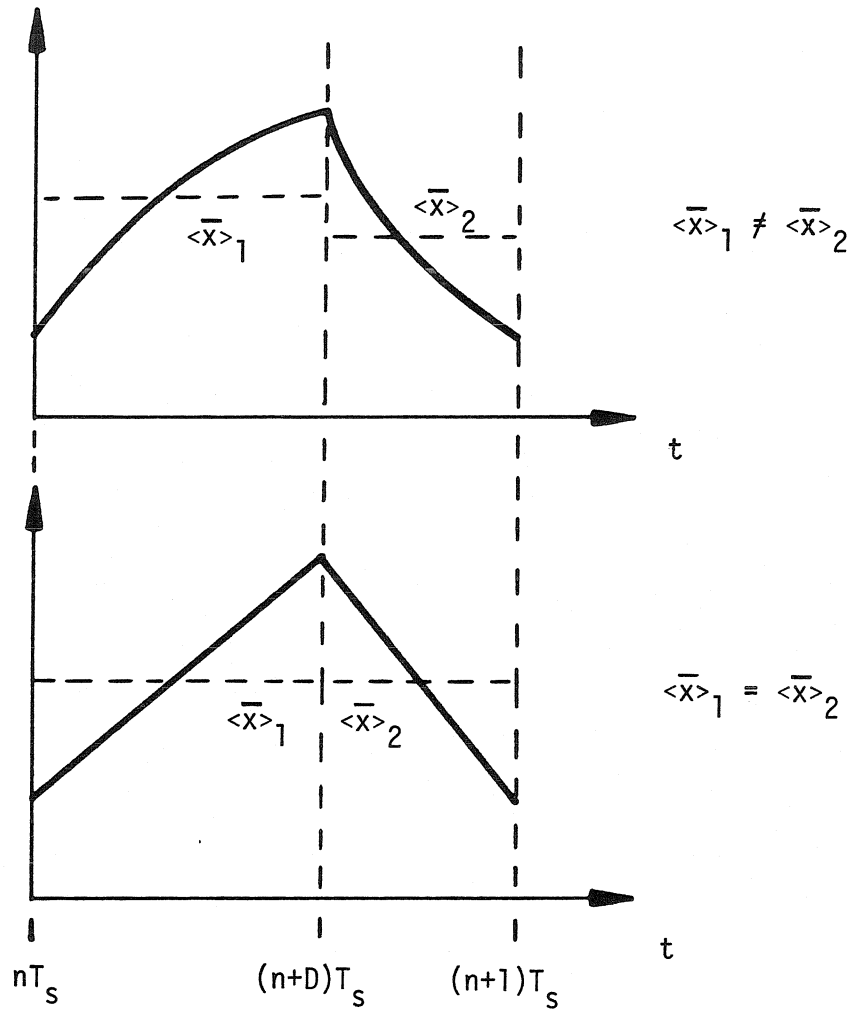
Figure 3.4. *Effect of straight-line approximation on the averages* $<\bar{x}>_1$ *and* $<\bar{x}>_2$.

$$X = -A^{-1}bV_g \qquad (3.20a)$$

$$A = DA_1 + D'A_2 \ , \quad b = Db_1 + D'b_2 \qquad (3.20b)$$

This result is the same as that obtained by Ćuk [1]. Thus, the average steady-state conditions of a converter can be found without the actual solution of a differential equation. In many designs, the switching ripple is so small that the average state vector X can be used in place of $\overline{x}[(n+D)T_s]$ in the small-signal state equation Eq. (3.15) with negligible error.

3.4 Conclusions

In this chapter the fundamentals of switching converter analysis were reviewed. In Section 3.2 a small-signal differential equation describing the transient behavior of switching converters was derived. While too complicated to be directly useful for analysis, this result is the starting point for the development of modeling techniques in subsequent chapters. A differential equation describing the steady-state behavior of switching converters was also formulated. In Section 3.3 it was demonstrated that, because of the straight-line approximation, the average values of steady-state converter waveforms can be found without the solution of the steady-state differential equation.

CHAPTER 4

REVIEW OF STATE-SPACE AVERAGING

AND ITS APPLICATION TO CURRENT-PROGRAMMING

4.1 Introduction

In this chapter the state-space averaging modeling technique, originated by Ćuk, is examined, with an emphasis on the method's accuracy at high frequencies. In Section 4.2 the state-space averaged model of switching converters is derived from the results of the previous chapter, with careful attention given to all assumptions used. The development followed here is not the same as that in the original work [1]; the intent here is to use a common form of derivation for several different analysis methods so that these various techniques can be more easily compared. It is found that for state-space averaging the straight-line approximation and a smoothing of the control function must be invoked to obtain the desired result. The analysis is extended from converters to regulators in Section 4.3, where feedback is discussed and the important concept of loop gain is introduced.

The resulting state-space averaging analysis technique is, in Section 4.4, applied to the case of a current-programmed regulator. It is found that the analysis does not predict the known subharmonic oscillation in this regulator, calling into question the high-frequency capabilities of state-space averaging. Section 4.5 presents conclusions.

4.2 Converter modeling

The starting point in this development of state-space averaging is the set of results from the previous chapter, Eqs. (3.13)-(3.15), repeated here as Eq. (4.1).

$$\dot{\hat{x}}(t) = [\overline{d}(t)A_1 + \overline{d}'(t)A_2]\hat{x}(t) + [\overline{d}(t)b_1 + \overline{d}'(t)b_2]\hat{v}_g(t) + K\hat{p}(t) \qquad (4.1a)$$

$$K = (A_1 - A_2)\overline{x}[(n+D)T_s] + (b_1 - b_2)V_g \qquad (4.1b)$$

$$\hat{p}(t) = \hat{u}(t)T_s \sum_{n=-\infty}^{\infty} \delta[t - (n+D)T_s] \qquad (4.1c)$$

$$\hat{d}_n = \hat{u}[(n+D)T_s] \qquad (4.1d)$$

The only approximation used in the derivation of these results is to assume that the perturbations in the switching function $d(t)$ and input $v_g(t)$ are small, so that nonlinear terms can be neglected and the finite-width pulses of $\hat{d}(t)$ can be replaced by the string of delta functions $\hat{p}(t)$.

Clearly, an existing modeling technique cannot be reproduced without prior knowledge of its form. State-space averaging represents the small-signal behavior of switching converters in terms of a linear, time-invariant state equation, driven by a continuous duty ratio modulation function. Now Eq. (4.1) is linear, but it is definitely not time-invariant, and the driving term consists of a string of delta functions. To arrive at a state-space averaging type of result, some further manipulation is necessary.

Each of the terms of the differential equation in Eq. (4.1a) must be modified in order to obtain a time-invariant result. The first two terms have time-varying coefficients, while the third, driving term actually samples the continuous signal $\hat{u}(t)$. The simplest way to remedy the situation is to replace the undesirable time-varying quantities by their average values. Of course, this change will result in a loss of accuracy. The following analysis attempts to determine the degree of error introduced.

Suppose first that no duty ratio modulation is present, that is, $\hat{p}(t)=0$. Suppose further that $\hat{v}_g(t)$ consists solely of components which vary slowly with respect to the switching frequency, so that it may be considered constant over a switching period. Then Eq. (4.1a) can easily be solved for the state at time $(n+1)T_s$ in terms of the state at time nT_s via a two-step integration over the intervals $[nT_s, (n+D)T_s]$ and $[(n+D)T_s, (n+1)T_s]$.

$$\hat{x}[(n+D)T_s] = e^{A_1 DT_s}\hat{x}[nT_s] + \int_{nT_s}^{(n+D)T_s} e^{A_1[(n+D)T_s-\tau]}b_1\hat{v}_g\,d\tau \qquad (4.2a)$$

$$= e^{A_1 DT_s}\hat{x}[nT_s] + A_1^{-1}(e^{A_1 DT_s} - I)b_1\hat{v}_g \qquad (4.2b)$$

$$\hat{x}[(n+1)T_s] = e^{A_2 D'T_s}e^{A_1 DT_s}\,\hat{x}[nT_s] + e^{A_2 D'T_s}A_1^{-1}(e^{A_1 DT_s} - I)b_1\hat{v}_g$$
$$+ \int_{(n+D)T_s}^{(n+1)T_s} e^{A_2[(n+1)T_s-\tau]}b_2\hat{v}_g\,d\tau \qquad (4.3a)$$

$$= e^{A_2 D'T_s}e^{A_1 DT_s}\hat{x}[nT_s] + e^{A_2 D'T_s}A_1^{-1}(e^{A_1 DT_s} - I)b_1\hat{v}_g$$
$$+ A_2^{-1}(e^{A_2 D'T_s} - I)b_2\hat{v}_g \qquad (4.3b)$$

Although this result appears complex, it can be reduced to a simple form by another invocation of the extremely useful straight-line approximation, first discussed in Chapter 2. In this instance, the exponential matrices of Eq. (4.3) can be accurately represented by the first two terms of their Taylor series expansions, with all higher-order terms neglected. The use of this approximation, together with the neglect of all terms of order greater than T_s, gives a simple yet accurate approximation of Eq. (4.3).

$$\hat{x}[(n+1)T_s] = [I + (DA_1+D'A_2)T_s]\hat{x}[nT_s] + (Db_1+D'b_2)T_s\hat{v}_g \qquad (4.4)$$

However, this result is precisely the straight-line approximation to the solution of another, simpler, differential equation.

$$\dot{\hat{x}}(t) = A\hat{x}(t) + b\hat{v}_g(t) \qquad (4.5a)$$

$$A = DA_1 + D'A_2 \quad , \quad b = Db_1 + D'b_2 \qquad (4.5b)$$

This equation is both linear and time-invariant, as desired for state-space averaging. In fact, it is the result of the averaging of the time-varying coefficients in the original equation, as suggested earlier. Hence, with little loss in accuracy, Eq. (4.5) can replace Eq. (4.1) for the case $\hat{p}(t)=0$, and the original equation has been partly reduced to the state-space averaging form.

The third term of Eq. (4.1a) remains to be examined. This driving term, which inserts the effects of duty ratio modulation, consists of a string of delta functions, effectively sampling the continuous function $\hat{u}(t)$.

$$K\hat{p}(t) = K \left\{ T_s \sum_{n=-\infty}^{\infty} \delta[t - (n+D)T_s] \right\} \hat{u}(t) \qquad (4.6)$$

As stated earlier, the state-space averaged model employs a continuous duty ratio modulation function. Hence, it is natural to interpret the function $\hat{u}(t)$ as this input, and to treat the bracketed factor in Eq. (4.6) as an unwanted (for state-space averaging) time-dependent coefficient. As before, a simple way to remove this offending quantity is to take its time average.

$$\frac{1}{T_s} \int_{kT_s}^{(k+1)T_s} T_s \sum_{n=-\infty}^{\infty} \delta[t - (n+D)T_s] dt = 1 \qquad (4.7)$$

This step effectively replaces the pulsed duty ratio modulation function $\hat{p}(t)$ in

the differential equation by the continuous function $\hat{u}(t)$. Of course, as for the previous modifications of Eq. (4.1), this change introduces errors into the model, principally in allowing $\hat{u}(t)$ to affect the model at all times, rather than only at a single instant in each switching cycle as in the original equation. Because of this qualitative change in the nature of the driving term, this modification, in contrast to the previous manipulations, is not easily justified.

With these changes, Eq. (4.1) appears in quite different form.

$$\dot{\hat{x}}(t) = A\hat{x}(t) + b\hat{v}_g(t) + K\hat{u}(t) \tag{4.8a}$$

$$A = DA_1 + D'A_2 \;,\; b = Db_1 + D'b_2 \tag{4.8b}$$

$$K = (A_1 - A_2)\bar{x}[(n+D)T_s] + (b_1 - b_2)V_g \tag{4.8c}$$

$$\hat{d}_n = \hat{u}[(n+D)T_s] \tag{4.8d}$$

Except for the appearance of $\bar{x}[(n+D)T_s]$ instead of the average steady state vector X, this equation is just the state-space averaging model. Indeed, since the ripple on a state waveform is usually much less than the average value of that waveform, the average state X can usually be substituted in Eq. (4.8) for $\bar{x}[(n+D)T_s]$, as remarked in Section 3.3. A block diagram of the state-space averaged model is shown in Fig. 4.1.

4.3 Controller and regulator modeling

The fact that the converter model is only valid for small perturbations means that the controller model need only be a small-signal model. Hence, nonlinearities can be neglected in the usual fashion, and duty ratio modulation can be
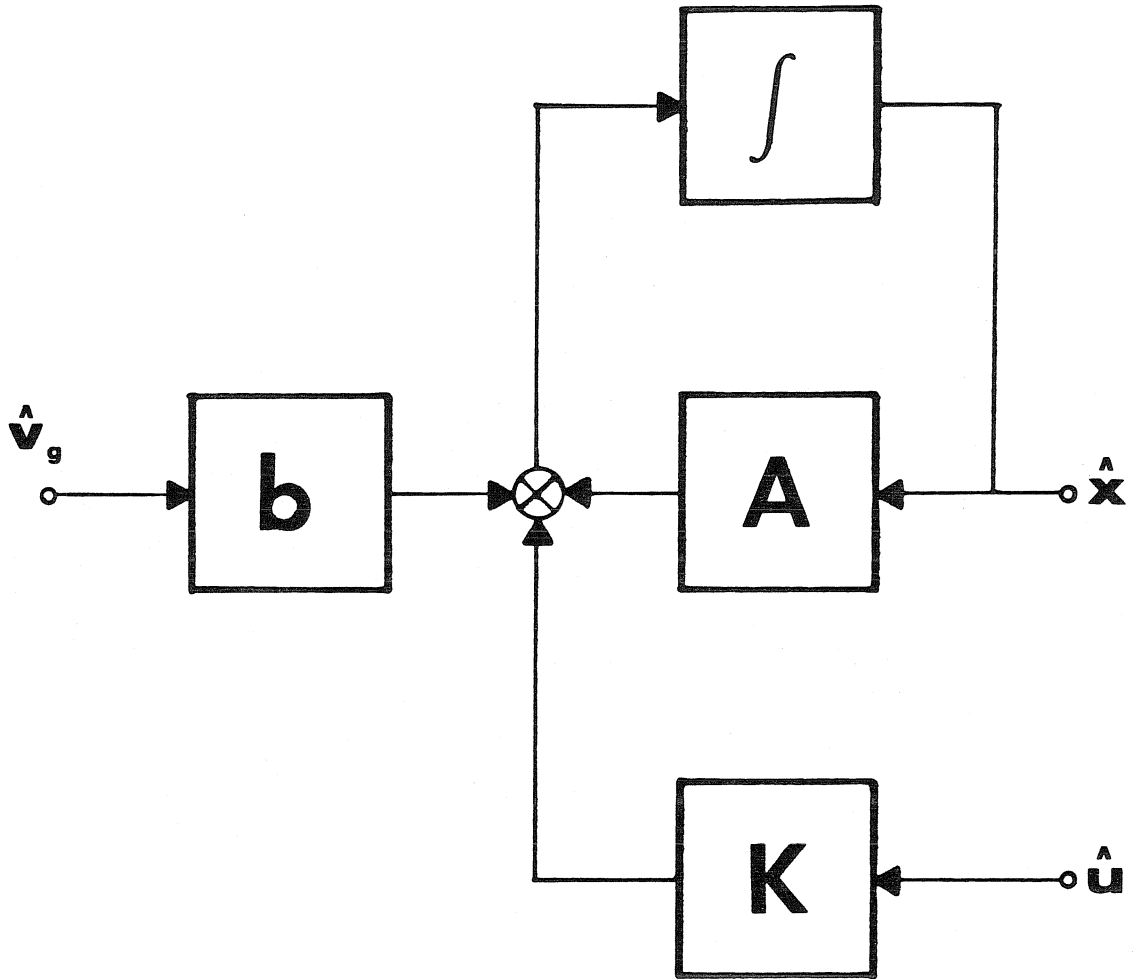
Figure 4.1. *Block diagram of the state-space averaged converter model.*

described, in the Laplace transform domain, as a linear combination of possibly processed state waveforms.

$$\widehat{U}(s) = -H_e^T \widehat{X}(s)$$

<div align="right">(4.9)</div>

The effective gain vector H_e (the superscript T means transposed) may vary with operating point but is fixed once an operating point is chosen. It may contain frequency-dependent terms representing, for example, filtering or time delays.

The combination of Eq. (4.9) with the Laplace transform of the state-space averaged equation, Eq. (4.8), gives an equation for the duty ratio modulation.

$$\widehat{U}(s) = \frac{-H_e^T(sI-A)^{-1}b}{1 + H_e^T(sI-A)^{-1}K}\widehat{V}_g(s)$$

<div align="right">(4.10)</div>

From Eq. (4.10), a loop gain $T(s)$ can be defined, since by definition the closed-loop poles s_p of a system with loop gain $T(s)$ satisfy $T(s_p)=-1$.

$$T(s) = H_e^T(sI - A)^{-1}K$$

<div align="right">(4.11)</div>

The stability criterion is that the system is unstable if any of the closed-loop poles s_p lie in the right-half s-plane.

The state-space averaging approach has been a very fruitful one [1,4,7,8,9]. The model it presents provides a simple yet accurate picture of converter operation, allowing the confident design of regulator systems. In addition, the linear, time-invariant form of its state equation allows an equivalent, linear, time-invariant circuit model to be developed, which can then be embedded as an element in a surrounding circuit system.

However, one step in the development of state-space averaging does not seem to be entirely justified. Specifically, the replacement of the pulsed duty ratio modulation function $\hat{p}(t)$ by the continuous function $\hat{u}(t)$ seems somewhat questionable. In effect, this replacement of pulses by a smooth function amounts to the elimination of a sampler. For low modulation frequencies compared to the sampling frequency (equal to the switching frequency), the presence or absence of a sampler will have little effect, but for systems whose bandwidths approach half the switching frequency it seems probable that the effects of sampling cannot be safely neglected. In the next section a current-programmed regulator provides an example in which state-space averaging provides incorrect information.

4.4 State-space averaged analysis of current-programming

Consider the current-programming modulator waveforms shown in Fig. 4.2. From Fig. 4.2b, the form of the controller equation is easily seen.

$$\hat{d}_n T_s = -\frac{\hat{i}_L[(n+D)T_s]}{r_1} \quad , \quad \hat{u} = -\frac{\hat{i}_L}{r_1 T_s} \qquad (4.12)$$

Here r_1 is the slope of the steady-state rising current waveform, and r_2 is the magnitude of the steady-state falling current slope.

The loop gain, as given by Eq. (4.11), will now be evaluated for a current-programmed regulator. Consider a circuit which consists of two states, an inductor current i_L and a capacitor voltage v_C.

$$\hat{x} = \begin{bmatrix} \hat{i}_L \\ \hat{v}_C \end{bmatrix} \qquad (4.13)$$
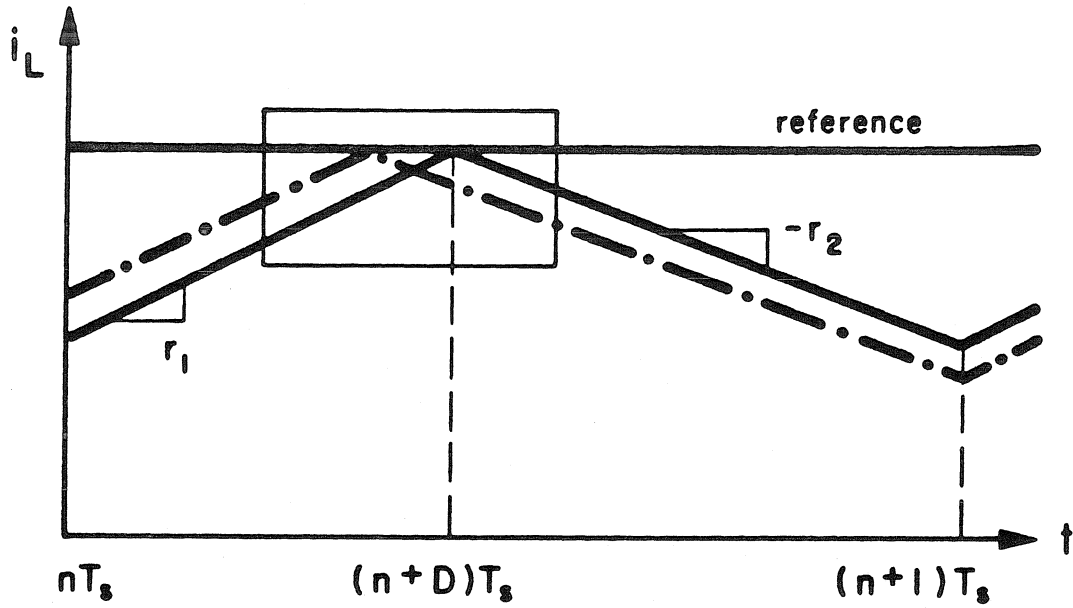
- 40 -

(a) current-programming modulator waveforms

steady-state
perturbed
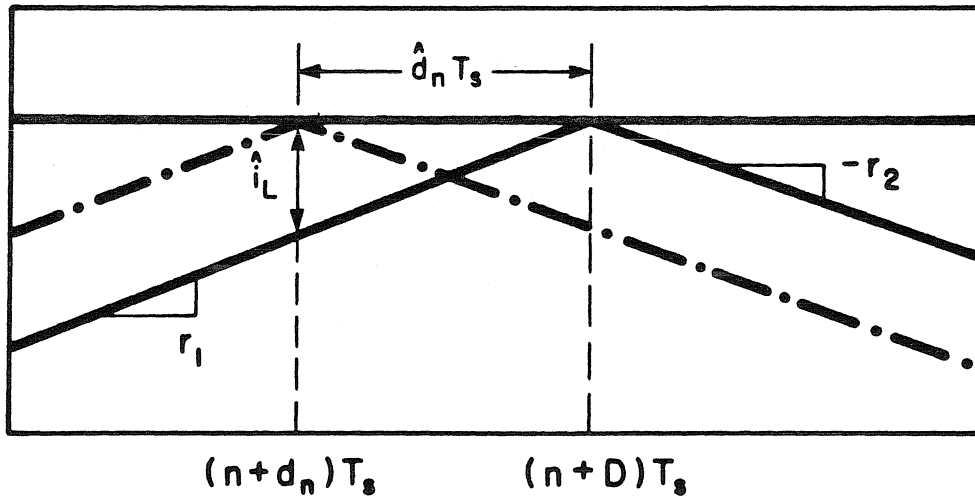
(b) expanded view of (a)

Figure 4.2. *Current-programming modulator waveforms.*

Because the converter is a low-pass system, the dynamics of the state matrix A are low-frequency in nature. In a discussion of a high-frequency phenomenon such as the subharmonic oscillation of current-programming, the low-frequency effects can be ignored by the substitution $A=0$. This step also generalizes the analysis by making it applicable to any two-state converter, and is in contrast to a previous current-programming analysis [4], which concentrated on low-frequency effects and neglected high-frequency terms. From Eqs. (4.9) and (4.12) the effective gain vector H_e can be determined.

$$H_e = \begin{bmatrix} \dfrac{1}{\tau_1 T_s} \\ 0 \end{bmatrix} \qquad (4.14)$$

It remains to determine the vector K. Examination of the expression for K in Eq. (4.8) and the original converter state equations, Eq. (3.1), shows that the components of K are just the differences between the steady state rates of change of each state just before and just after the time $(n+D)T_s$. For the inductor current these slopes are τ_1 and $-\tau_2$, respectively. The other component of K will prove to be irrelevant.

$$K = \begin{bmatrix} \tau_1 + \tau_2 \\ - \end{bmatrix} \qquad (4.15)$$

Substitution of Eqs. (4.14) and (4.15) into the loop gain formula, Eq. (4.11), with $A=0$ gives an explicit expression for this particular loop gain.

$$T(s) = \left(1 + \frac{\tau_2}{\tau_1}\right)\frac{1}{sT_s} \qquad (4.16)$$

Since the closed-loop pole s_p satisfies $T(s_p)=-1$, its location can be easily found.

$$s_p = -\frac{1}{T_s}\left(1+\frac{\tau_2}{\tau_1}\right) \tag{4.17}$$

This high-frequency pole is the one which appeared to vanish in previous analysis [4], where the order of the system was apparently reduced by one. This disappearance occurred because high-frequency effects were purposely neglected in that study. Conversely, because of the substitution $A=0$, this analysis neglects low-frequency effects, and hence does not uncover the low-frequency pole and zero uncovered previously [4].

The crucial aspect of the pole s_p in Eq. (4.17) is that it always lies in the left-half s-plane. This position implies a stable system. Hence, state-space averaging has failed to predict the known instability in this feedback technique.

It may be argued that the reason no instability was uncovered was that the analysis was too simple and that a more detailed calculation would reveal the instability. This criticism would be valid except that, as will be seen, equally simple analyses by two other modeling techniques do correctly predict the instability.

It is not difficult to see why state-space averaging might lose accuracy at high frequencies in light of the previous discussion of the model's development. It might very well be suspected that it is impossible to achieve both such a simple model and good accuracy at high frequencies. In the next two chapters two other methods will be discussed which, at the expense of some of the simplicity of state-space averaging, do correctly predict the current-programming instability.

4.5 Conclusions

The state-space averaging modeling technique for switching converters was derived from the foundations developed in Chapter 3. It was found that, besides the small-signal assumption, two other approximations are needed to complete the development. One of these was shown to be related to the straight-line approximation, and therefore is justified. However, the other, which consists of the replacement of a pulsed waveform with a continuous one, effectively removing a sampler, could not be supported. These suspicions were strengthened when a state-space averaged analysis of current-programmed regulators failed to reveal the potential high-frequency instability in these systems. Thus, although state-space averaging is very accurate in the low-frequency regime, its capabilities appear to be overextended at frequencies approaching one-half the switching frequency.

CHAPTER 5

REVIEW OF DISCRETE MODELING

AND ITS APPLICATION TO CURRENT-PROGRAMMING

5.1 Introduction

State-space averaging has as its goal the creation of the simplest possible continuous model for the small-signal behavior of switching converters, a linear, time-invariant state equation. The previous chapter discussed this model's considerable success and also noted a shortcoming, specifically, the high-frequency performance of the model. In this present chapter a different analysis technique is reviewed. This alternate method, the discrete modeling technique of Packard, seeks to describe the small-signal behavior of the converter at only one instant of time during each switching cycle, saying nothing about the waveforms between these points.

The treatment in this chapter parallels that of state-space averaging in Chapter 4, although the results are of course different. In Section 5.2, the model is developed from the fundamental equation derived in Chapter 3, the method of development being the same as that originally used by Packard [2]. It is found that no approximations besides the small-signal assumption are needed in the derivation, implying that the resulting model should be quite accurate. However, its form is unusual, requiring a new transform technique for its interpretation.

The development of the discrete method is extended to regulators in Section 5.3, where a loop gain analogous to the state-space averaged loop gain is defined. This discrete modeling method is then, in Section 5.4, applied to a current-programmed regulator. There the expected accuracy of the method is

verified, for it correctly predicts the stability characteristics of the current-programmed system, both for the original control arrangement and for a modified scheme in which an artificial ramp is added to the feedback circuit to avoid subharmonic oscillations. Advantage is then taken of this accurate analysis technique to treat several aspects of current-programmed regulators. The qualitative differences in the high-frequency performances and the forms of the state-space averaging and discrete modeling techniques are also discussed. Conclusions are presented in Section 5.5.

5.2 Converter modeling

The development of the discrete modeling technique begins, as in the case of state-space averaging, with the fundamental Eqs. (3.13) and (3.15), rewritten here as Eq. (5.1).

$$\dot{\hat{x}}(t) = [\overline{d}(t)A_1 + \overline{d}'(t)A_2]\hat{x}(t) + [\overline{d}(t)b_1 + \overline{d}'(t)b_2]\hat{v}_g(t)$$

$$+ [(A_1 - A_2)\overline{x}[(n+D)T_s] + (b_1 - b_2)V_g]\hat{p}(t) \qquad (5.1a)$$

$$\hat{p}(t) = \hat{d}_n T_s \sum_{n=-\infty}^{\infty} \delta[t - (n+D)T_s] \qquad (5.1b)$$

It is important to remember that the only approximation used in the derivation of this equation was the assumption that the perturbations in $d(t)$ and $v_g(t)$ were small, which made the nonlinear terms small enough to be neglected and which also allowed the replacement of the pulses of $\hat{d}(t)$ by the delta functions of $\hat{p}(t)$. Note also that the continuous, non-unique function $\hat{u}(t)$ is not introduced in this development.

The derivation begins with the integration of Eq. (5.1) over a switching period.

The starting point of the integration is arbitrary, but if it is chosen based on the type of controller to be used, the control equation can be simplified. One controller which has been successfully employed [10] uses uniform sampling: the fed-back signal is sampled at the instants nT_s, and this value, by comparison with a ramp, is used to determine the duty ratio d_n for the n-th cycle. A second method, in widespread use, involves natural sampling, in which the fed-back waveform is compared directly against a ramp to determine the duty ratio. In this case, it is the values of the fed-back state at the instants of switching, $(n+D)T_s$, which determine the duty ratio.

Since, as has been mentioned, discrete modeling gives predictions only for certain instants of time, it is convenient to choose those instants to correspond to those moments at which the fed-back state determines the duty ratio. This choice makes the problem of regulator design simpler. The special instants correspond to the choice of the initial point for the integration of Eq. (5.1). In this chapter, it will be assumed that natural sampling is to be employed; consequently, the integration will begin at the moment $(n+D)T_s$. An analysis based on a uniformly sampling controller is outlined in Part III of this thesis.

The first portion of the integration covers the interval $[(n+D)T_s, (n+1)T_s]$. The state equation in this interval reduces to a simpler form because $\overline{d}(t)=0$ and $\overline{d}'(t)=1$.

$$\dot{\hat{x}} = A_2\hat{x} + b_2\hat{v}_g + KT_s\hat{d}_n\delta[t-(n+D)T_s], \quad (n+D)T_s < t < (n+1)T_s \quad (5.2a)$$

$$K = (A_1 - A_2)\overline{x}[(n+D)T_s] + (b_1 - b_2)V_g \quad (5.2b)$$

Note that the delta function at $(n+D)T_s$ is included in the integrand for this period, rather than at the end of the previous period. The reason for this

procedure is somewhat subtle. In regulator analysis the duty ratio modulation at time $(n+D)T_s$ will be determined by $\hat{x}[(n+D)T_s]$, the state vector at that instant. If this state value were to include the effects of the duty ratio modulation delta function at time $(n+D)T_s$, the controller would know the results of its actions before they happened, a clear contradiction. To maintain causality in the model, the duty ratio modulation at time $(n+D)T_s$ must be assumed to affect the state only at times later than $(n+D)T_s$, not at $(n+D)T_s$ itself. This rule is automatically followed by the integration procedure chosen.

After this digression the formal integration of Eq. (5.2) continues.

$$\hat{x}[(n+1)T_s] = e^{A_2 D'T_s}\hat{x}[(n+D)T_s] + e^{A_2 D'T_s}KT_s\hat{d}_n$$

$$+ \int_{(n+D)T_s}^{(n+1)T_s} e^{A_2[(n+1)T_s - \tau]} b_2 \hat{v}_g \, d\tau \tag{5.3}$$

Note that a problem now arises because of the source modulation $\hat{v}_g$. It is not possible to evaluate this integral explicitly. However, since the main point of the discrete modeling technique is to predict stability, not the effects of input variation, the difficulty is eliminated by the assumption $\hat{v}_g = 0$, as will be assumed from now on for this method.

$$\hat{x}[(n+1)T_s] = e^{A_2 D'T_s}\hat{x}[(n+D)T_s] + e^{A_2 D'T_s}KT_s\hat{d}_n \tag{5.4a}$$

$$\hat{v}_g(t) = 0 \tag{5.4b}$$

To complete the integration over the remainder of the switching period, it is necessary to examine the differential equation in the interval $[(n+1)T_s, (n+1+D)T_s]$.

$$\dot{\hat{x}} = A_1 \hat{x} \quad , \quad (n+1)T_s < t < (n+1+D)T_s \qquad (5.5)$$

This equation is readily solved.

$$\hat{x}[(n+1+D)T_s] = e^{A_1 DT_s} e^{A_2 D'T_s} \hat{x}[(n+D)T_s] + e^{A_1 DT_s} e^{A_2 D'T_s} KT_s \hat{d}_n \qquad (5.6)$$

This result is one of the principal findings of the discrete modeling method. It is a difference, as opposed to a differential, equation, and is both linear and shift invariant. Shift invariance is the discrete equivalent of time invariance in continuous equations. In Eq. (5.6) shift invariance is a consequence of the constant coefficients. An important point to notice is that no additional assumptions or approximations were used to derive this result from Eq. (5.1), in contrast to the derivation of state-space averaging. Thus, it seems that, at least in some sense, discrete modeling is a more natural method for the analysis of switching converters than state-space averaging.

In another sense, however, discrete modeling is distinctly unnatural, since it gives up the continuous methods engineers are accustomed to using, and therefore renders the Laplace transform ineffective. Fortunately, another tool is available for these linear, shift-invariant difference equations. This new technique is the z-transform [11], which converts sequences of numbers into analytic functions in a z-plane, much as the Laplace transform converts continuous functions into analytic functions in an s-plane. Some properties of the one-sided z-transform used in this thesis are reviewed in Appendix A. Application of one of these to the transformation of Eq. (5.6) gives a corresponding equation in the z-plane.

$$\hat{X}(z) = (zI - M)^{-1} M K T_s \hat{D}(z) + (zI - M)^{-1} z \hat{x}(0) \qquad (5.7a)$$

$$M = e^{A_1 D T_s} e^{A_2 D' T_s} \qquad (5.7b)$$

Transformed quantities are represented by upper-case letters, with the type of the transform, Laplace or z, denoted by the functional dependence, s or z, respectively.

5.3 Controller and regulator modeling

In a formal sense controller and regulator modeling in the discrete case are very similar to the corresponding analyses for state-space averaging. Since the converter was analyzed in such a fashion that the instants at which the states are available are the same as the instants at which the duty ratio modulation is determined, a simple expression can be used to account for many feedback schemes.

$$\hat{d}_n = -H_e^T \hat{x}_n \qquad (5.8)$$

Here subscripts, rather than a specific time, are used with the state vector because the exact time instant within a cycle at which the duty ratio modulation is determined depends on the controller in question. H_e is a vector of effective gains, which may vary with operating point but are constants once the operating point is fixed.

The combination of the z-transform of the controller equation, Eq. (5.8), with the converter equation, Eq. (5.7), which was for natural sampling, it should be remembered, gives an expression for the behavior of the duty ratio in response

to a state disturbance.

$$\hat{D}(z) = \frac{-H_e^T(zI-M)^{-1}z\hat{x}(0)}{1 + H_e^T(zI-M)^{-1}MKT_s} \tag{5.9}$$

From this equation a loop gain $T_z(z)$ can be defined according to the definition that the closed-loop poles z_p of a system satisfy $T_z(z_p)=-1$.

$$T_z(z) = H_e^T(zI-M)^{-1}MKT_s \tag{5.10}$$

The stability criterion is that the system is unstable if any of the closed-loop poles z_p lie outside the unit circle in the z-plane.

5.4 Discrete analysis of current-programming

The current-programmed waveforms of Fig. 4.2 are reproduced here as Fig. 5.1. Examination of the waveforms reveals the discrete control law.

$$\hat{d}_n = -\frac{\hat{i}_L[(n+D)T_s]}{r_1 T_s} \tag{5.11}$$

Note that the converter model of Section 5.2 gives the states at exactly the instants required by the control law, as desired.

The discrete loop gain $T_z(z)$ of a current-programmed regulator will now be evaluated. Again, only converters with two state variables, an inductor current and a capacitor voltage, are considered.

$$\hat{x} = \begin{bmatrix} \hat{i}_L \\ \hat{v}_C \end{bmatrix} \tag{5.12}$$
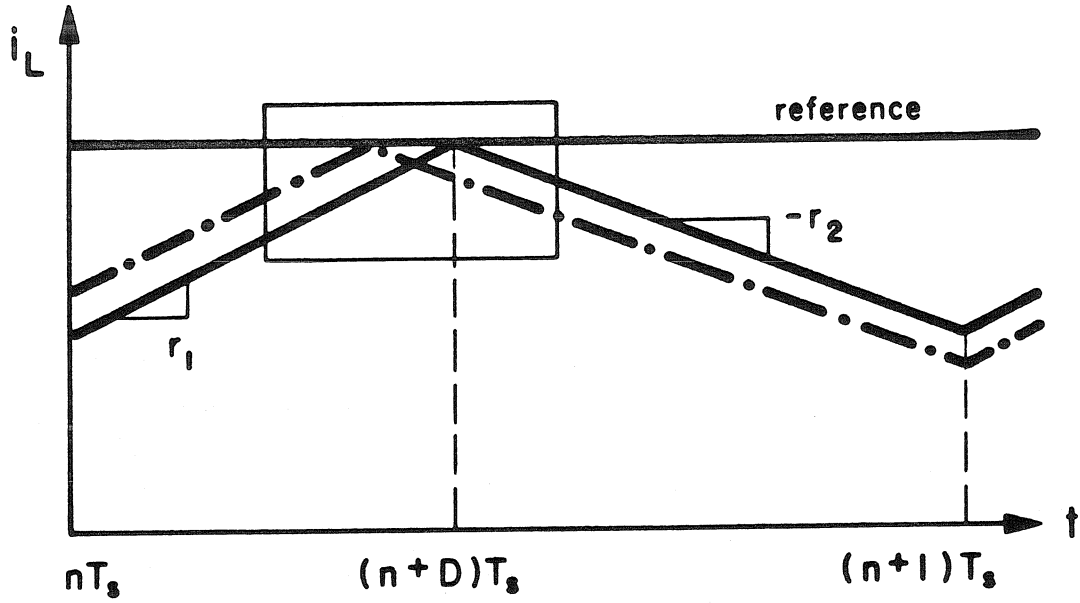
(a) current-programming modulator waveforms

steady-state
perturbed
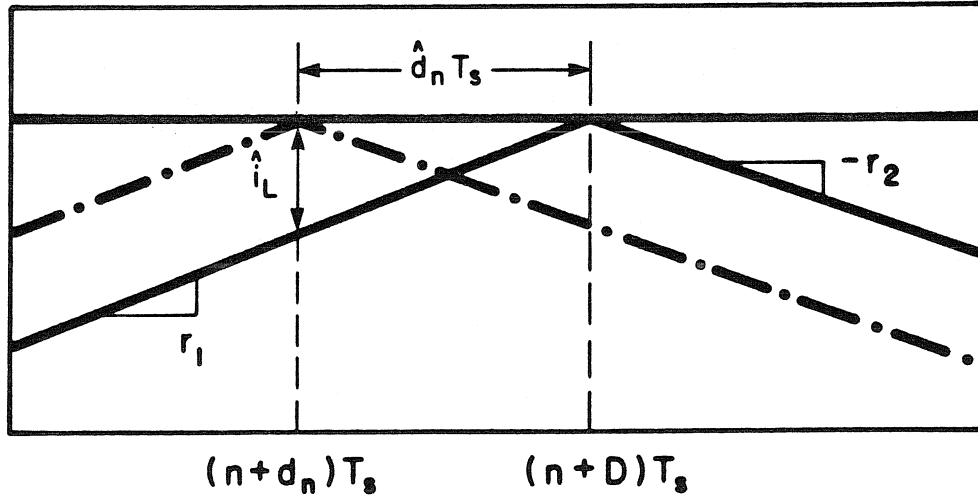
(b) expanded view of (a)

Figure 5.1. *Current-programming modulator waveforms.*

The effective feedback gain vector H_e is written from inspection of the control law, Eq. (5.11).

$$H_e = \begin{bmatrix} \dfrac{1}{r_1 T_s} \\ 0 \end{bmatrix} \tag{5.13}$$

Note that this result equals the state-space averaging analysis result. Similarly, the vector K is the same as in the state-space averaged case.

$$K = \begin{bmatrix} r_1 + r_2 \\ - \end{bmatrix} \tag{5.14}$$

Again only one component is significant for this calculation. Finally, because the dynamics represented by the M matrix in Eq. (5.7) are much slower than the sought-after high-frequency phenomena, this matrix is approximated by the unit matrix.

$$M = e^{A_1 D T_s} e^{A_2 D' T_s} \approx I \tag{5.15}$$

This step is equivalent to the substitution $A = 0$ in the state-space averaged analysis. The loop gain $T_z(z)$ can now be easily found.

$$T_z(z) = \left(1 + \frac{r_2}{r_1}\right) \frac{1}{z - 1} \tag{5.16}$$

The rates of change r_1 and r_2 may be replaced by the duty ratio by means of a relationship which can be derived from Fig. 5.1.

$$D\tau_1 = D'\tau_2 \qquad (5.17a)$$

$$\frac{\tau_2}{\tau_1} = \frac{D}{D'} \qquad (5.17b)$$

Substitution of this relation into Eq. (5.16) gives a simple result.

$$T_z(z) = \frac{1}{D'}\frac{1}{z-1} \qquad (5.18)$$

The closed-loop pole z_p satisfies $T_z(z_p) = -1$ and is easily evaluated.

$$z_p = -\frac{D}{D'} \qquad (5.19)$$

The locus of this pole as a function of duty ratio is shown in Fig. 5.2. It is seen that even this approximate discrete modeling analysis reveals a subharmonic instability when the duty ratio reaches one-half, exactly the behavior seen in actual current-programmed regulators.

The appearance of only one pole in a two-state system is a consequence of the choice $M = I$, just as the substitution $A = 0$ in the state-space averaged analysis of current-programming gave only a single pole. In reality there are two poles, but one is close to a zero, near $z = 1$, as shown in Fig. 5.3. The choice $M = I$ makes this pole cancel exactly with the zero, but the cancellation is not perfect for a non-unity M. In addition, a non-unity M may affect the critical duty ratio at which the converter becomes unstable.

It has been found that if the ramp formed by the inductor current is supplemented by an artificial ramp, as in the general controller of Fig. 2.3, the subharmonic instability can be removed [4]. In fact, a particular choice of artificial
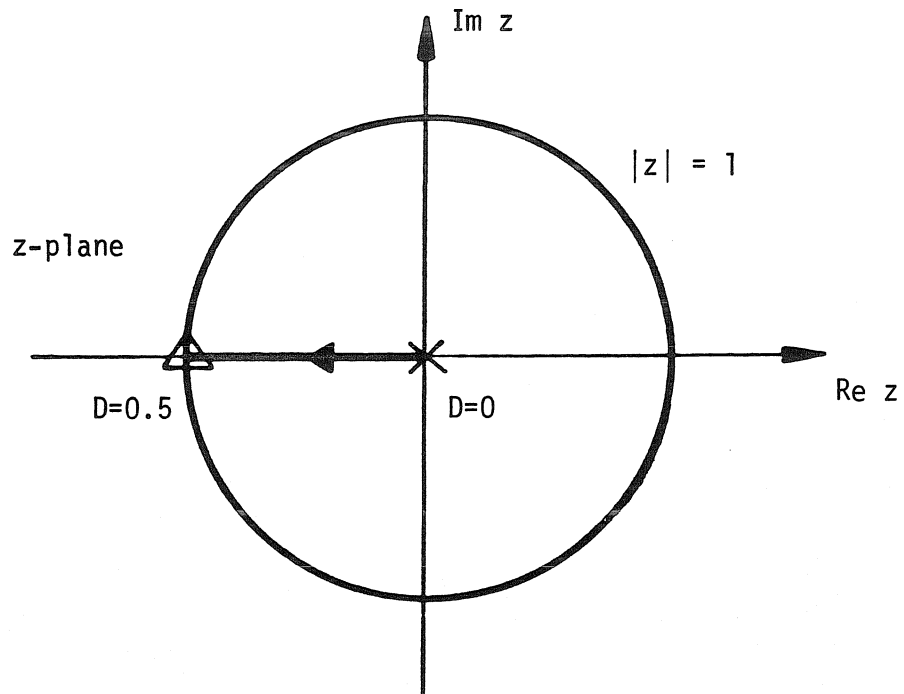
Figure 5.2. *Root locus plot of the current-programming pole as a function of duty ratio.*
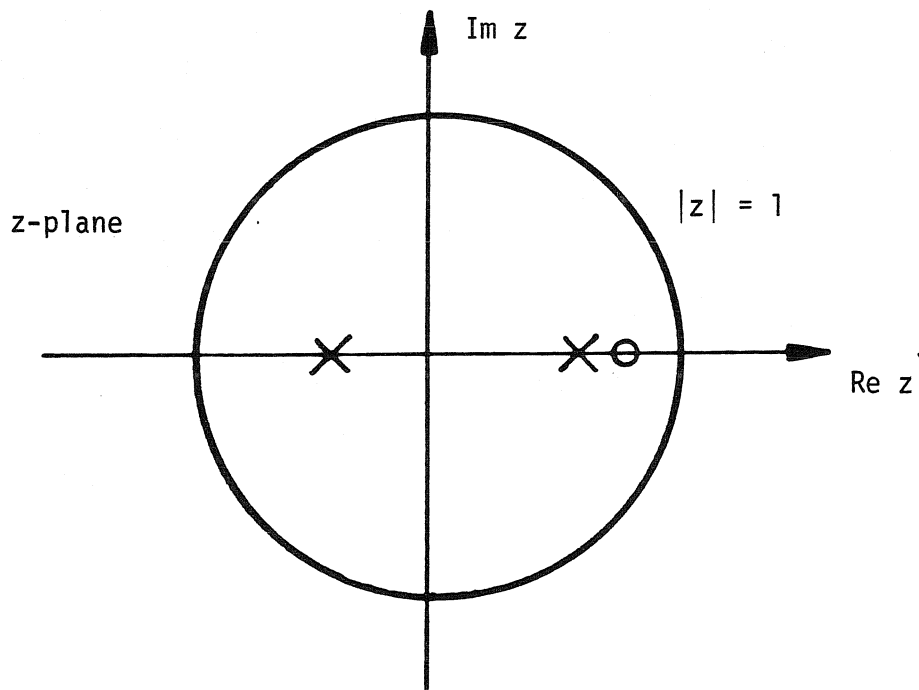
Figure 5.3. *Actual pole and zero locations in a current-programmed converter. The zero cancels one pole exactly when M=1.*

ramp slope has been shown to eliminate any current error in one switching cycle. This compensation technique can also be analyzed with use of the discrete modeling technique. Consider the current-programmed modulator of Fig. 5.4, to which an artificial ramp of slope r_R has been added. From this figure, a new control law is easy to determine.

$$\hat{i}_L[(n+D)T_s] = -(r_1+r_R)\hat{d}_n T_s \qquad (5.20a)$$

$$\hat{d}_n = -\frac{\hat{i}_L[(n+D)T_s]}{(r_1+r_R)T_s} \qquad (5.20b)$$

The loop gain for this case can be evaluated by use of this new control law in place of the old one.

$$T_z(z;r_R) = \frac{r_1+r_2}{r_1+r_R}\frac{1}{z-1} \qquad (5.21)$$

The new closed-loop pole location is also easily found.

$$z_p = \frac{r_R-r_2}{r_R+r_1} \qquad (5.22)$$

Examination of this equation shows that the choice $r_R=r_2$ places the pole exactly at the origin of the z-plane, corresponding to the elimination of current errors in one cycle, as illustrated in Appendix A. This result is exactly that found previously [4].

A few more words on current-programmed systems are appropriate at this point. By itself a current-programmed circuit does not constitute a voltage regulator; the output voltage must be fed back in addition to the inductor
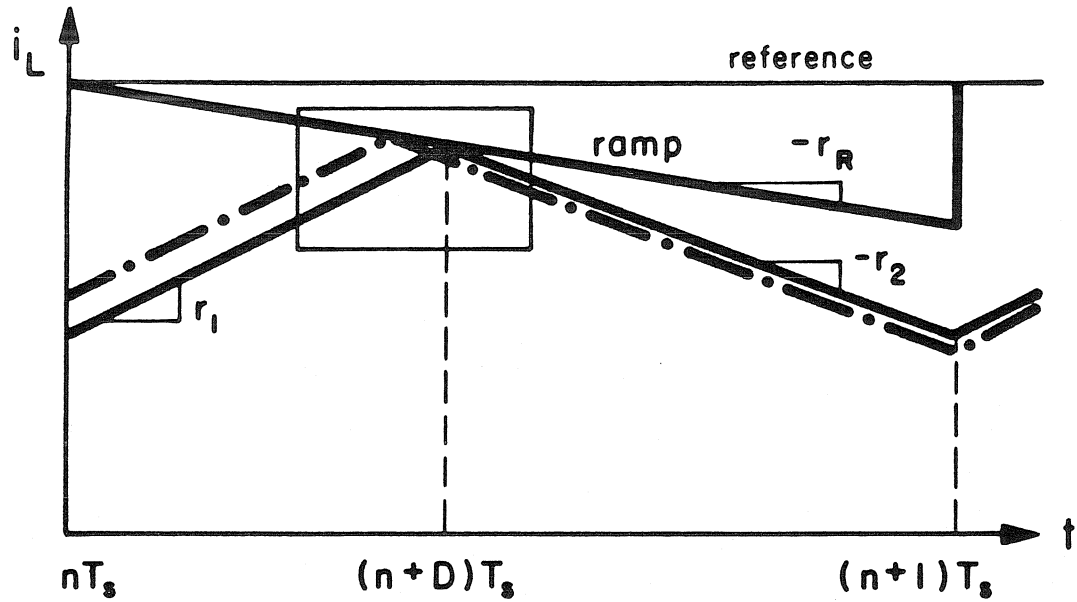
(a) *current-programming modulator waveforms, including artificial ramp*

	steady-state
	perturbed
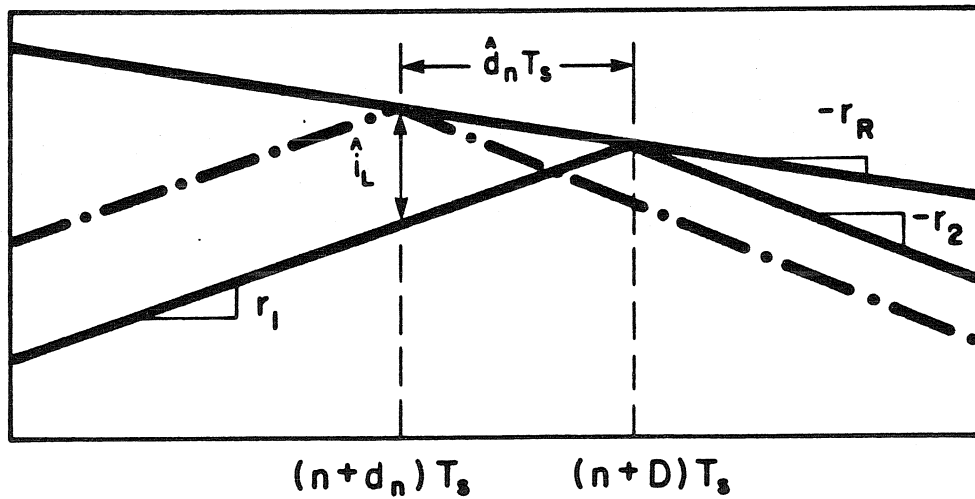
(b) *expanded view of (a)*

Figure 5.4. *Current-programming modulator waveforms, including artificial ramp.*

current to achieve output regulation. This system can be analyzed as a multi-loop feedback problem; however, since the current feedback loop is already determined, another idea is to treat the current-programmed circuit as a new plant about which voltage feedback is to be applied, as illustrated in Fig. 5.5. Here the gain h_1 is already chosen via the current-programming and any artificial ramp used; only h_2 is to be determined. The effects of variations in h_2 on the system dynamics can be explored with the use of a root locus diagram. The open-loop poles of this root locus, that is, the poles when h_2 is zero, are just the closed-loop poles of the current-programmed circuit, since this closed-loop system is the plant for the voltage feedback analysis. The zeros of the voltage feedback loop gain are determined by the details of the converter in question. A possible resulting root locus is shown in Fig. 5.6. In this example, the high frequency open-loop pole is seen to lie roughly halfway between the z-plane origin and the unstable point $z=-1$, and the loop gain zero is assumed to lie outside the unit circle. As the gain h_2 increases, the system poles migrate according to the usual root locus rules. Note in particular that both poles will cross the unit circle. The point at which one of them first touches the unit circle marks the onset of instability.

An important aspect of this example is that, in the discrete analysis, the high-frequency pole behaves just like any other pole. There is nothing magical about it. In particular, this analysis shows that it is misleading to think that it is possible to position the high-frequency pole via current-programming and then, independently, apply voltage feedback to obtain a regulator; this point of view neglects the effects of the voltage feedback on the high-frequency pole, which migrates like any other pole when feedback is applied. Thus, it is entirely possible that a current-programmed regulator designed to be stable in the
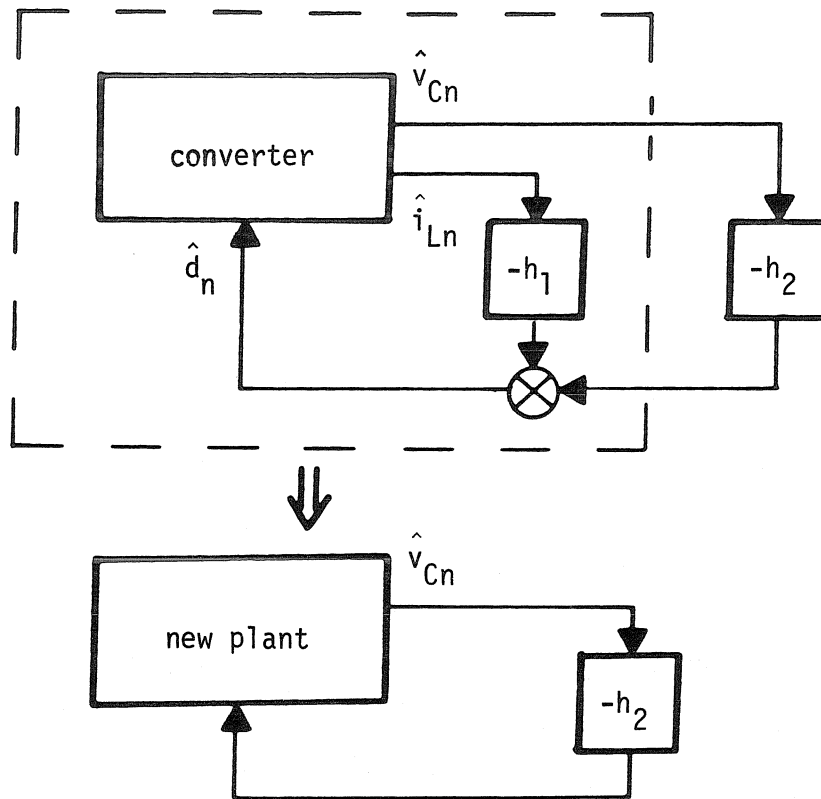
Figure 5.5. *Addition of output voltage feedback to a current-programmed regulator, absorbing the current feedback path into the plant.*
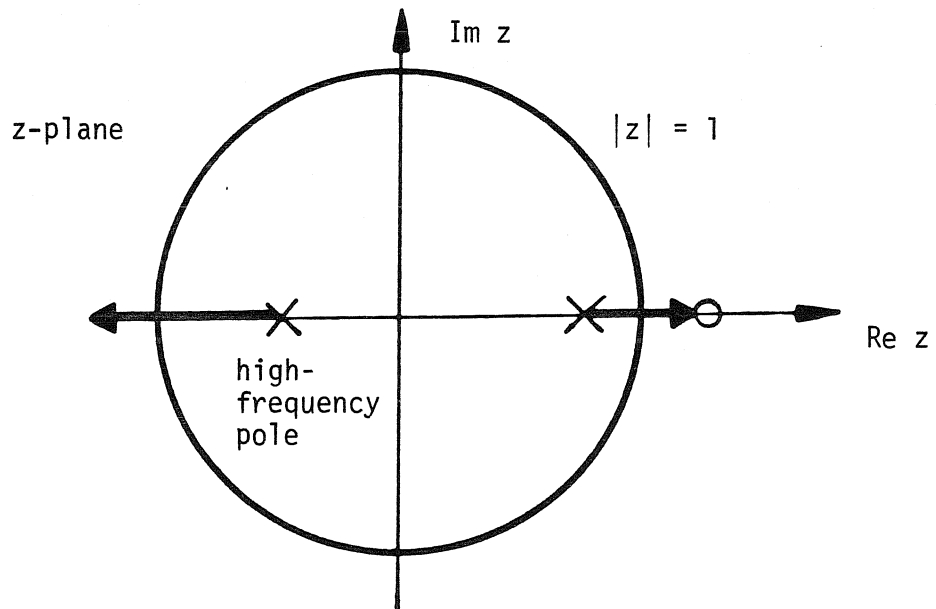
Figure 5.6. *Root locus plot for output voltage feedback in a current-programmed regulator.*

absence of voltage feedback will develop a subharmonic instability if excessive voltage feedback is applied.

Thus far, the emphasis has been placed on the differences between state-space averaging and discrete modeling predictions for current-programmed circuits. However, the qualitative differences in results given by the two techniques are not limited solely to this one application. Indeed, it is easy to see that any regulator whose state-space averaged loop gain looks like a single pole at high frequencies will be expected, according to state-space averaging, to have no high-frequency instabilities, but that the corresponding discrete model of the system will predict subharmonic oscillations if the gain of the loop is made too large. This difference is illustrated in Fig. 5.7.

These examples illustrate the accuracy of the discrete modeling technique in the analysis of switching converters. Problems with its use remain, however. One is the lack of insight into the method which generally exists in the minds of engineers. Another is that it is not clear how to make measurements to confirm a discrete modeling design. Laboratory measurement equipment is heavily oriented towards frequency-domain analysis, but the discrete modeling technique discusses only sequences of numbers. The transformation $z = e^{sT_s}$ can be used to map from the z to the s-plane, as will be discussed later, but conventional measurements may still not agree with discrete modeling predictions. These measurement questions will be explored in greater detail in Part II of this thesis, with the aid of a new modeling technique which will be developed in the next chapter.

5.5 Conclusions

In this chapter, the discrete modeling technique was shown to represent
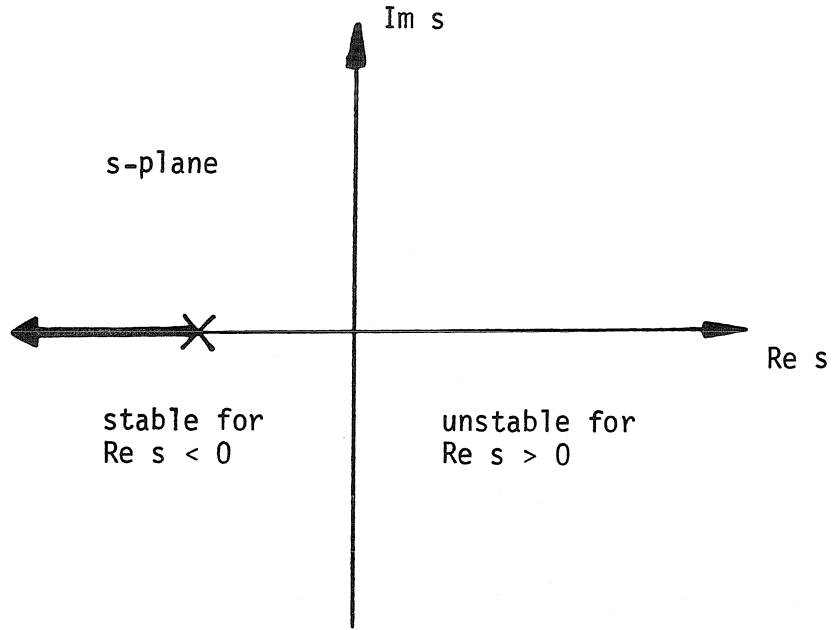
(a) state-space averaging: stable for any gain
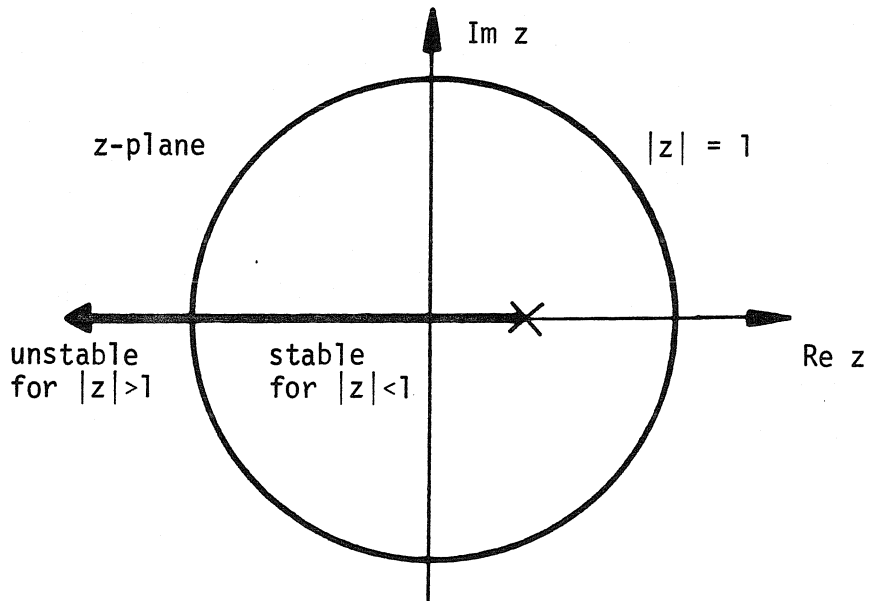
(b) discrete modeling: unstable if gain is too large

Figure 5.7. *Root locus plot for a loop gain with a single pole, as predicted by two modeling techniques.*

switching regulators by a set of linear, shift-invariant difference equations which can then be analyzed by use of the z-transform. Only the small-signal approximation is needed to develop this model, and it was therefore expected to be very accurate. This expectation was confirmed by the method's successful analysis of current-programmed regulators, and, owing to the confidence generated by this accomplishment, the method was then exploited to discuss several aspects of these systems. In particular, it was pointed out that the high-frequency pole of such a regulator is not fixed solely by the current feedback but is also affected by the output voltage feedback necessary to obtain output regulation. Thus, a current-programmed regulator which is perfectly stable with only current feedback applied can develop a subharmonic instability when the output voltage is also fed back.

The differences in the predictions of state-space averaging and discrete modeling were then shown to exist not just for current-programming but for many other switching regulator systems as well. Generally, in such cases a state-space averaging result will predict stability, while the discrete method predicts instability. However, the increased high-frequency accuracy of the discrete technique is only obtained at the expense of a convenient model form. The difference equations of the discrete approach are generally unfamiliar to engineers, and, furthermore, are not directly applicable to the interpretation of frequency-domain measurements, the kind usually made on switching regulators.

CHAPTER 6

DEVELOPMENT OF SAMPLED-DATA MODELING

AND ITS APPLICATION TO CURRENT-PROGRAMMING

6.1 Introduction

The previous two chapters have reviewed two different switching converter modeling methods. One of them, state-space averaging, results in a continuous, linear, time-invariant system which is very attractive to practicing engineers. However, it sacrifices accuracy at high frequencies in achieving this goal, as evidenced by its failure to predict subharmonic oscillations in current-programmed regulators. The second method, the discrete modeling technique, while possessing great accuracy, has a form which is unfamiliar to the engineer and is not oriented towards frequency-domain measurements.

In Section 6.2 of this chapter, a new modeling technique, the sampled-data method, which combines the continuous form of state-space averaging with the accuracy of the discrete method, is developed. The new model is obtained by the incorporation of only one of the two approximations used in the derivation of state-space averaging.

The sampled-data modeling technique is extended in Section 6.3 to include regulator modeling. A subtle but important aspect of this extension is the inclusion of a small time delay to maintain the causality of the system. The result is a sampled-data loop gain which can be used for stability analysis.

The new modeling technique is then applied in Section 6.4 to the analysis of current-programming. There its accuracy is verified by its successful prediction of the subharmonic oscillation occurring in these systems. Finally, conclusions are drawn in Section 6.5.

6.2 Converter modeling

Both the state-space averaging and the discrete models were developed from
the same equations, Eqs. (3.13) and (3.15), repeated here as Eq. (6.1).

$$\dot{\hat{x}}(t) = [\overline{d}(t)A_1 + \overline{d}'(t)A_2]\hat{x}(t) + [\overline{d}(t)b_1 + \overline{d}'(t)b_2]\hat{v}_g(t)$$

$$+ [(A_1 - A_2)\overline{x}[(n+D)T_s] + (b_1 - b_2)V_g]\hat{p}(t) \tag{6.1a}$$

$$\hat{p}(t) = \sum_{n=-\infty}^{\infty} \hat{d}_n T_s \delta[t-(n+D)T_s] = \hat{u}(t)T_s \sum_{n=-\infty}^{\infty} \delta[t-(n+D)T_s] \tag{6.1b}$$

The only approximation used in the derivation of this equation was to assume
that all perturbations about the steady state are small. The discrete modeling
technique made no further approximations in its development, but state-space
averaging, it will be recalled, required some additional modifications. It is not
too surprising then, that the predictions of the two models differ.

Two steps were required to convert Eq. (6.1) into the form of state-space
averaging. The first was to retain only the average values of $\overline{d}(t)A_1 + \overline{d}'(t)A_2$
and $\overline{d}(t)b_1 + \overline{d}'(t)b_2$; the components which varied at the switching frequency
or higher were neglected. The second step was to smooth out the pulsed nature
of the driving term $\hat{p}(t)$, converting it into a continuous function. It is natural
to ask whether one of these steps was more responsible than the other for the
degradation of the ability of state-space averaging to predict the subharmonic
oscillations of current-programmed regulators. This question will be answered
in this chapter by consideration of a model which, in a sense, lies between the
state-space averaging and the discrete modeling techniques.

The new model is obtained by use of only one of the two approximations

adopted in the development of state-space averaging. Specifically, the time-varying components of $\overline{d}(t)A_1 + \overline{d}'(t)A_2$ and $\overline{d}(t)b_1 + \overline{d}'(t)b_2$ are dropped, but $\hat{p}(t)$ is not modified. Recall that, in Chapter 4, this first step was shown to be related to the straight-line approximation, a good assumption, while the modification of $\hat{p}(t)$ was less well justified. A new state equation is thereby obtained.

$$\dot{\hat{x}}(t) = A\hat{x}(t) + b\hat{v}_g(t) + K\hat{p}(t) \qquad (6.2a)$$

$$A = DA_1 + D'A_2, \quad b = Db_1 + D'b_2 \qquad (6.2b)$$

$$K = (A_1 - A_2)\overline{x}[(n+D)T_s] + (b_1 - b_2)V_g \qquad (6.2c)$$

$$\hat{p}(t) = \sum_{n=-\infty}^{\infty} \hat{d}_n T_s \delta[t - (n+D)T_s] = \hat{u}(t)T_s \sum_{n=-\infty}^{\infty} \delta[t - (n+D)T_s] \qquad (6.2d)$$

A simple time translation is now performed so that the pulses occur at times nT_s, a standard form.

$$\dot{\hat{x}}(t) = A\hat{x}(t) + b\hat{v}_g(t) + K\hat{p}(t) \qquad (6.3a)$$

$$\hat{p}(t) = \sum_{n=-\infty}^{\infty} \hat{d}_n T_s \delta[t - nT_s] = \hat{u}(t)T_s \sum_{n=-\infty}^{\infty} \delta[t - nT_s] \qquad (6.3b)$$

The time translation is assumed to be understood; the notation for the functions involved is unchanged, as are the values of A, b, and K.

This model is called the sampled-data model because it has exactly the form of a sampled-data system. In such an entity, continuous signals flow through a continuous system, except for one or more points where signals are applied only

at equally spaced time intervals, with no information being received between the samples. The equation is linear, but, if $\hat{u}(t)$ is considered to be the input, it is not time-invariant, since a translation in $\hat{u}(t)$ by anything other than a multiple of T_s will not result in only a corresponding shift in the original output. A block diagram of the system is shown in Fig. 6.1. Here the definition of sampling a signal $\hat{u}(t)$ to obtain a sampled signal $\hat{u}^*(t)$ is slightly different than the usual practice.

$$\hat{u}^*(t) = \hat{u}(t)T_s \sum_{n=-\infty}^{\infty} \delta[t - nT_s] \tag{6.4}$$

The individual delta functions each have a weight $\hat{u}(nT_s)T_s$, not just $\hat{u}(nT_s)$.

Since the sampled-data model results in a continuous system, the appropriate analysis tool to employ is the Laplace transform, as it was for state-space averaging. In the present case, however, some new transform relations must be developed to deal with the pulse strings which occur in the driving term $\hat{p}(t)$. Appendix B discusses this issue in some detail. The symbol $V^*(s)$ will denote the Laplace transform of a sampled signal $v^*(t)$, whose original, unsampled waveform was $v(t)$, with Laplace transform $V(s)$.

6.3 Controller and regulator modeling

The block diagram of Fig. 6.1 suggests that, as for state-space averaging, a good controller model will construct the function $\hat{u}(t)$ as a linear combination of signals obtained by filtering and other processing of the states. However, in this case, care must be taken because of the presence of the delta functions produced by the sampler. These spikes have an instantaneous effect at the output of the integrator block of Fig. 6.1; hence, their effects can potentially
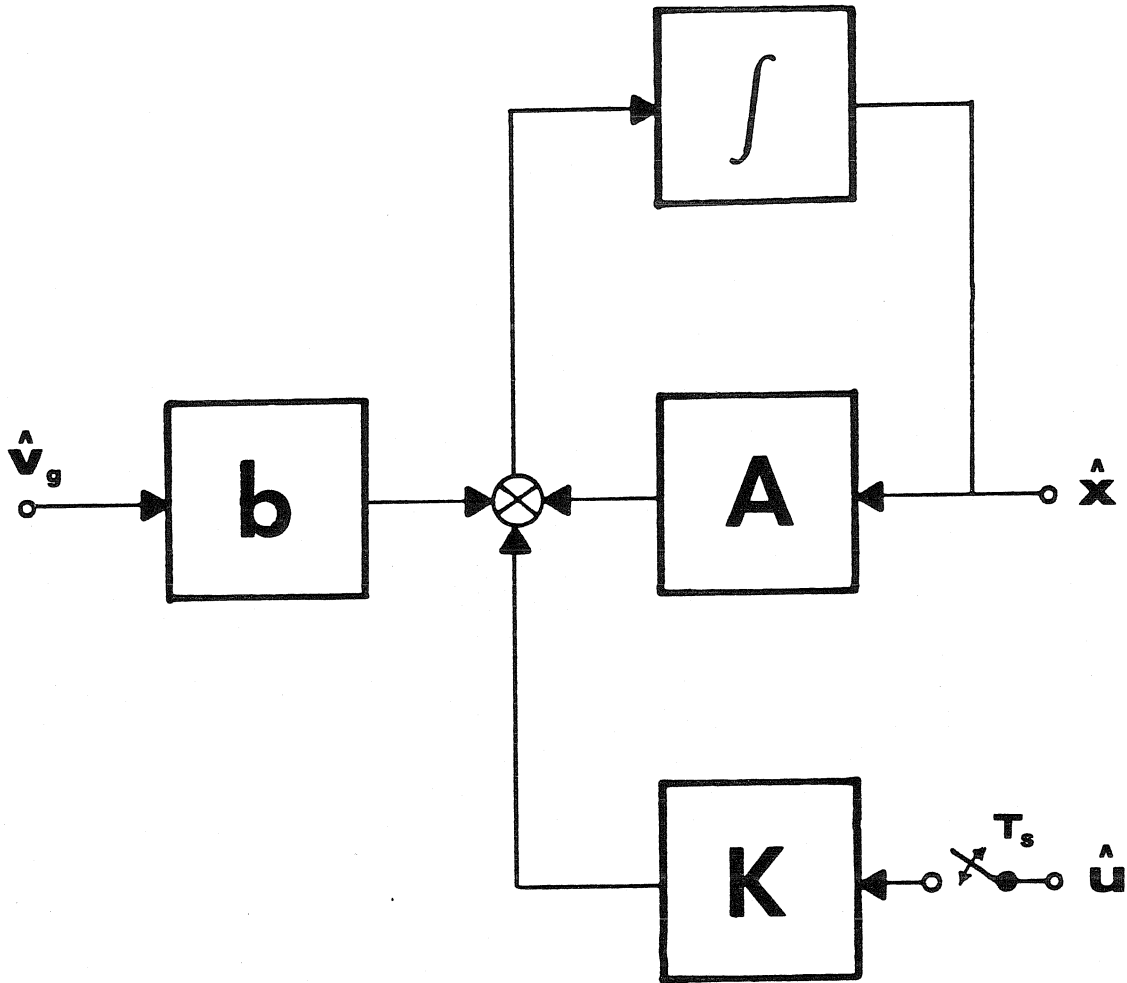
Figure 6.1. *Block diagram of the sampled-data model.*

influence their own creation, much as an incorrect handling of these pulses in Section 5.2 could have given an incorrect discrete model. In fact, if the problem in the sampled-data model is simply ignored, a non-causal system will result. To eliminate this defect, a small time delay ε is included in the modulator path; this delay, which is eventually allowed to go to zero, prevents the instantaneous transmission of the delta functions' influences and hence restores causality. With this addition the controller model can be stated.

$$\widehat{u}(t) = -H_e^T \widehat{x}(t-\varepsilon) \tag{6.5a}$$

$$\widehat{U}(s) = -H_e^T e^{-\varepsilon s} \widehat{X}(s) \tag{6.5b}$$

The Laplace transform of Eq. (6.3) provides the plant description.

$$\widehat{X}(s) = (sI-A)^{-1}b\widehat{V}_g(s) + (sI-A)^{-1}K\widehat{U}^*(s) + (sI-A)^{-1}\widehat{x}(0) \tag{6.6}$$

When combined, Eqs. (6.5) and (6.6) give an expression for the duty ratio modulation as a function of input voltage and initial state perturbation.

$$\widehat{U}^*(s) = -H_e^T[e^{-\varepsilon s}\widehat{X}(s)]^* \tag{6.7a}$$

$$= -H_e^T[e^{-\varepsilon s}(sI-A)^{-1}b\widehat{V}_g(s)]^* - H_e^T[e^{-\varepsilon s}(sI-A)^{-1}K\widehat{U}^*(s)]^*$$

$$-H_e^T[e^{-\varepsilon s}(sI-A)^{-1}]^*\widehat{x}(0) \tag{6.7b}$$

A theorem in Appendix B allows the sampled Laplace transform $\widehat{U}^*(s)$ to be removed from any additional sampling, and hence this equation can be solved for $\widehat{U}^*(s)$.

$$\widehat{U}^{\circ}(s) = \frac{-H_e^T[e^{-\varepsilon s}(sI-A)^{-1}b\widehat{V}_g(s)]^{\circ}-H_e^T[e^{-\varepsilon s}(sI-A)^{-1}]^{\circ}\widehat{x}(0)}{1 + H_e^T[e^{-\varepsilon s}(sI-A)^{-1}]^{\circ}K} \qquad (6.8)$$

From Eq. (6.8), a loop gain $T_s^{\circ}(s)$ can be defined.

$$T_s^{\circ}(s) = H_e^T[e^{-\varepsilon s}(sI-A)^{-1}]^{\circ}K \qquad (6.9)$$

The subscript s is necessary to distinguish this loop gain from the sampled ver-
sion of the state-space averaged loop gain $T(s)$. The solutions of the equation
$1+T_s^{\circ}(s)=0$ are the closed-loop poles s_p of the system. As mentioned previously,
when a set of calculations involving these quantities is completed, the artificial
delay ε is allowed to go to zero. This limit is to be understood in Eq. (6.9) and in
all subsequent expressions.

6.4 Sampled-data analysis of current-programming

The steps involved in the analysis of a current-programmed switching regula-
tor are completely parallel to those for a state-space averaged analysis. First,
low-frequency effects are neglected, a step which also makes the analysis appli-
cable to all converters with two state variables.

$$A = 0 \qquad (6.10)$$

Next, the effective feedback gain vector and the relevant part of the forcing vec-
tor are calculated.

$$H_\theta = \begin{bmatrix} \dfrac{1}{\tau_1 T_s} \\ 0 \end{bmatrix} \qquad (6.11a)$$

$$K = \begin{bmatrix} \tau_1 + \tau_2 \\ - \end{bmatrix} \qquad (6.11b)$$

Finally, the sampled-data loop gain is evaluated from Eq. (6.9).

$$T_s^*(s) = \frac{1}{T_s} \left(\frac{e^{-\varepsilon s}}{s} \right)^* \frac{\tau_1 + \tau_2}{\tau_1} \qquad (6.12)$$

From Appendix B the appropriate sampled Laplace transform can be found.

$$\left(\frac{e^{-\varepsilon s}}{s} \right)^* = \frac{T_s}{e^{sT_s} - 1} \qquad (6.13)$$

Thus, an explicit form of the loop gain can be constructed.

$$T_s^*(s) = \frac{\tau_1 + \tau_2}{\tau_1} \frac{1}{e^{sT_s} - 1} \qquad (6.14)$$

The positions of the closed-loop poles s_p can be determined as the roots of $T_s^*(s_p) = -1$.

$$e^{s_p T_s} = -\frac{\tau_2}{\tau_1} = -\frac{D}{D'} \qquad (6.15)$$

Here the last equality makes use of Eq. (5.17). There are infinitely many solutions to this equation.

$$s_p = \frac{1}{T_s} \ln\left(-\frac{D}{D'}\right) = \frac{\omega_s}{2\pi} \ln\left(\frac{D}{D'}\right) + j(n+\tfrac{1}{2})\omega_s \qquad (6.16)$$

$$n = 0, \pm 1, \pm 2, \ldots$$

A plot of these poles in the s-plane appears in Fig. 6.2.

It is easily verified that for $D < D'$, that is, for duty ratios less than 0.5, the real parts of these poles are all negative, indicating a stable system with all poles in the left-half s-plane. Conversely, for duty ratios greater than 0.5, $D > D'$, and the poles lie in the right-half s-plane, implying an unstable system. This prediction matches exactly the observed behavior of current-programmed regulators.

6.5 Conclusions

In this chapter, a new modeling technique, the sampled-data method, was developed. The derivation parallels that of state-space averaging, but only one of the two approximations employed in that development is invoked. Time-varying components of the state matrices and driving vectors are averaged out, since this approximation was earlier shown to be related to the accurate straight-line approximation. However, the pulsed driving function is left unmodified. The result is a sampled-data system, the origin of the new technique's name. The continuous nature of this model allows the Laplace transform to be used as a tool for its interpretation.

In the course of the model's extension to regulator analysis, it was pointed out that causality problems could occur if care was not taken in the development. The addition of a small time delay, eventually to be allowed to go to zero, overcame this potential trouble. With this modification, a sampled-data loop
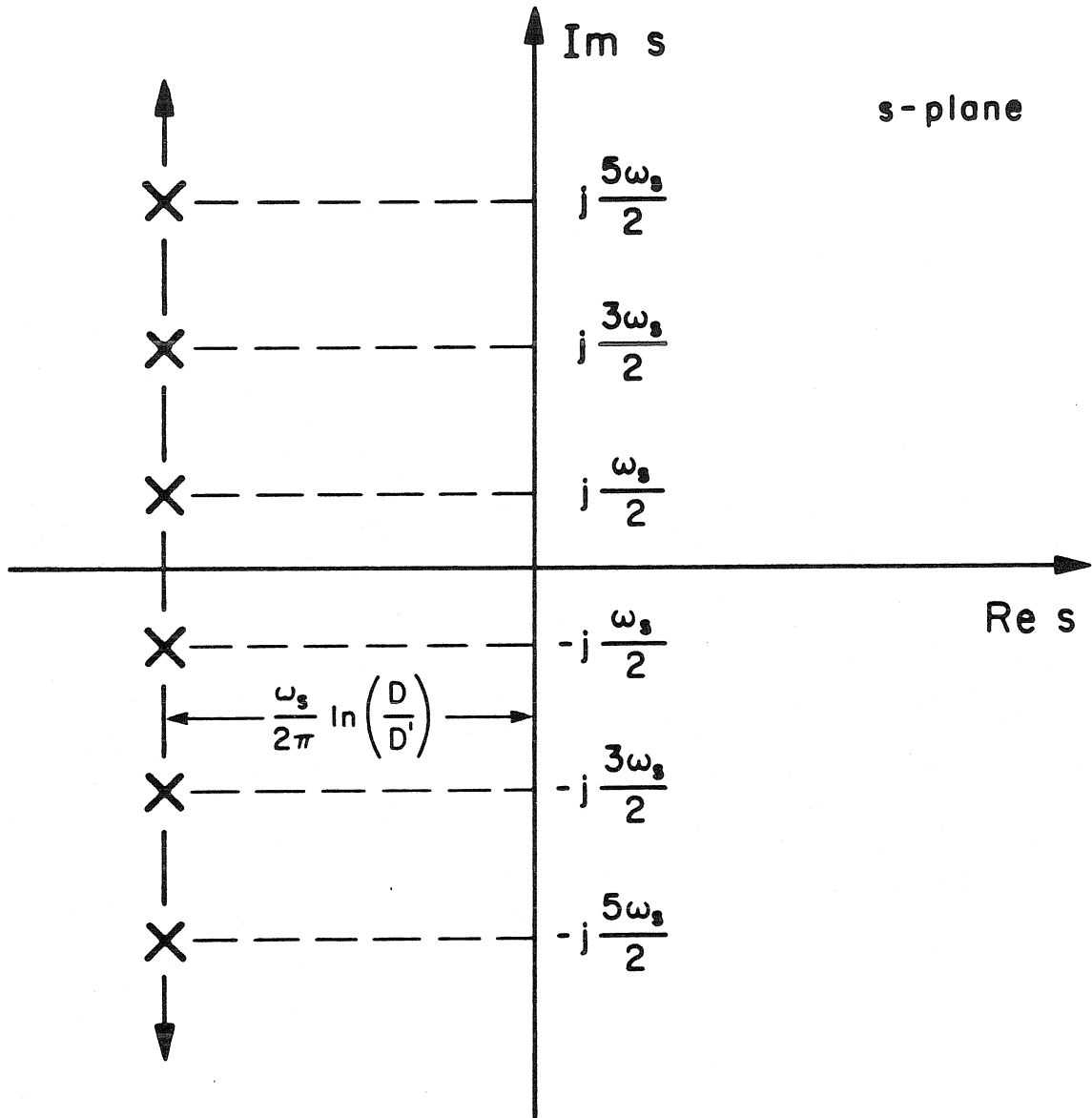
Figure 6.2. *Current-programming pole locations in the s-plane (stable case shown).*

gain was defined.

The first application of the sampled-data technique was the analysis of current-programming. The accuracy of the new method was verified by its correct prediction of the potential subharmonic instability. Thus, while possessing the continuous form of state-space averaging, the sampled-data technique also matches the discrete method in accuracy and therefore combines the best features of each in a single model.

CHAPTER 7

SAMPLED-DATA MODELING AND ITS RELATIONSHIPS
WITH DISCRETE MODELING AND STATE-SPACE AVERAGING

7.1 Introduction

The previous chapter introduced a new modeling technique, sampled-data modeling, which possesses a continuous form like that of state-space averaging, yet which displays accuracy, at least for current-programmed regulators, comparable to that of discrete modeling. The purpose of the present chapter is to explore the relationships between this new technique and the two previously known methods, displaying their similarities and differences and showing how to transform between them. In addition, some general properties of the sampled-data loop gain will be developed. In this chapter, current-programming is no longer given special treatment; the results achieved here are applicable to many kinds of switching regulator systems.

In Section 7.2 the connections between discrete modeling and the sampled-data method are explored. The comparison is conducted in both the time and transform domains. It is seen that the two models are, to a great degree, equivalent, simply different representations of the same system. Thus, for a given application, the choice between these two can be determined by convenience considerations.

The comparison between the state-space averaging and the sampled-data techniques occurs in Section 7.3. A comparison of the block diagrams of these two methods reveals one picture of the difference between the two, the presence or absence of a sampler. This relation allows the equivalent circuits developed for state-space averaging to be used, with only one modification, for the

sampled-data technique as well. This difference between the two methods is also represented in both the time and frequency domains. It is seen that the state-space averaged loop gain forms a limiting case of the sampled-data loop gain.

A particular, commonly occurring loop gain, for which state-space averaging predicts stability for any gain constant but the sampled-data method does not, is then analyzed. Following this specific case, a general relationship is developed which approximately transforms between the sampled-data and state-space averaged loop gains. The section ends with a review of the differences between the two models, relating these divergences to the differences in the original derivations of the two techniques.

In Section 7.4 the sampled-data loop gain is examined. When considered as a function of real frequency, as employed in many design procedures, this loop gain is seen to be periodic, to be real at certain frequencies, and to possess several symmetries, all of which make its plotted form quite striking. These general properties can also be used to define limits on the design process. Finally, conclusions are presented in Section 7.5.

7.2 Sampled-data modeling versus discrete modeling

As was mentioned in the Introduction, the comparison between the sampled-data and discrete methods can be carried out in both the time and transform domains. Consider first the time domain. To compare the sampled-data method with the discrete method, it is necessary to integrate the sampled-data equation over one switching period. The appropriate sampled-data equation, obtained from Eq. (6.2), is stated here as Eq. (7.1). The source perturbation $\hat{v}_g$ is taken to be zero, in accordance with the discrete model's assumptions.

$$\dot{\widehat{x}} = A\widehat{x} + K\widehat{d}_n T_s \delta[t - (n+D)T_s] \ , \quad (n+D)T_s < t < (n+1+D)T_s \qquad (7.1)$$

The integration is straightforward.

$$\widehat{x}[(n+1+D)T_s] = e^{AT_s}\widehat{x}[(n+D)T_s] + e^{AT_s}KT_s\widehat{d}_n \qquad (7.2)$$

Compare this result with the corresponding expression for discrete modeling, Eq. (5.6), repeated here as Eq. (7.3).

$$\widehat{x}[(n+1+D)T_s] = e^{A_1 DT_s}e^{A_2 D'T_s}\widehat{x}[(n+D)T_s] + e^{A_1 DT_s}e^{A_2 D'T_s}KT_s\widehat{d}_n \qquad (7.3)$$

The sole difference is the replacement of the expression $e^{A_1 DT_s}e^{A_2 D'T_s}$ by the matrix $e^{AT_s} = e^{DA_1 T_s + D'A_2 T_s}$. This replacement is justified by the straight-line approximation, since both expressions have the same first-order expansions.

$$e^{A_1 DT_s}e^{A_2 D'T_s} \approx (I + A_1 DT_s)(I + A_2 D'T_s) \qquad (7.4a)$$

$$\approx I + A_1 DT_s + A_2 D'T_s \qquad (7.4b)$$

$$= I + AT_s \qquad (7.4c)$$

$$\approx e^{AT_s} \qquad (7.4d)$$

Because the straight-line approximation is an excellent assumption for switching converters, the two methods are virtually equivalent in the time domain.

Similarly, in the transform domain, a close relationship exists between the sampled-data loop gain $T_s^*(s)$ and the discrete loop gain $T_z(z)$. As reviewed in

Appendix C, if these two loop gains truly represent the same system, the change of variables $z = e^{sT_s}$ should transform one into the other. The sampled-data loop gain $T_s^*(s)$ is given by Eq. (6.9), repeated here as Eq. (7.5).

$$T_s^*(s) = H_e^T[e^{-\varepsilon s}(sI - A)^{-1}]^* K \qquad (7.5)$$

Recall that the delay ε is required to preserve causality and is eventually allowed to go to zero. This equation can be manipulated into a different but equivalent form. If the numbers $v(nT_s)$ are the sampled values of a function $v(t)$, the sampled waveform's Laplace transform can be written as an infinite series involving these values. This expression is derived in Appendix B, and is repeated here as Eq. (7.6).

$$V^*(s) = T_s \sum_{n=0}^{\infty} v(nT_s)e^{-snT_s} \qquad (7.6)$$

The time function corresponding to the Laplace transform $(sI - A)^{-1}$ in Eq. (7.5) is easily obtained from consideration of an appropriate matrix differential equation.

$$\dot{m} = Am \; ; \; m(0) = I \qquad (7.7a)$$

$$M(s) = (sI - A)^{-1} \qquad (7.7b)$$

$$m(t) = \begin{cases} 0 & \text{if } t < 0 \\ e^{At} & \text{if } t \geq 0 \end{cases} \qquad (7.7c)$$

The values of the matrix function $m(t)$ at times nT_s are not precisely the numbers to be inserted in Eq. (7.6), however; the delay $e^{-\varepsilon s}$ present in Eq. (7.5)

adds a lag in the time sequence, causing the first term of the series in Eq. (7.6) to vanish.

$$[e^{-\varepsilon s}(sI-A)^{-1}]^{\bullet} = T_s \sum_{n=1}^{\infty} e^{A(nT_s-\varepsilon)} e^{-nsT_s} \qquad (7.8a)$$

$$= T_s e^{-\varepsilon A}(I - e^{AT_s} e^{-sT_s})^{-1} e^{AT_s} e^{-sT_s} \qquad (7.8b)$$

$$= T_s (e^{sT_s}I - e^{AT_s})^{-1} e^{AT_s} \qquad (7.8c)$$

In the last step the delay ε was allowed to go to zero, having served its purpose in eliminating the first term of the series. The loop gain $T_s^{\bullet}(s)$ can now be written in this new form.

$$T_s^{\bullet}(s) = H_e^T(e^{sT_s}I - e^{AT_s})^{-1} e^{AT_s} KT_s \qquad (7.9)$$

This expression can be directly compared with that for the discrete loop gain $T_z(z)$, Eq. (5.10), repeated here as Eq. (7.10).

$$T_z(z) = H_e^T(zI - M)^{-1} MKT_s \qquad (7.10a)$$

$$M = e^{A_1 DT_s} e^{A_2 D'T_s} \qquad (7.10b)$$

It is assumed that the two models are defined such that the effective feedback gain vectors H_e are the same. Then if, as in the time domain discussion, the straight-line approximation is valid, that is, $M \approx e^{AT_s}$, the two loop gains are related by the change of variables $z = e^{sT_s}$ and are two equivalent representations of the same system. Hence, their stability predictions will be nearly identical.

Thus, in both the time and transform domains, the only difference between the sampled-data model and the discrete model was found to be the straight-line approximation. This result should not be surprising. Both methods used a small-signal approximation, but while discrete modeling employed no further approximations, the sampled-data method invoked the straight-line approximation as well. Hence results like those found here should be expected.

Another feature is that, in actual calculations with the discrete modeling technique, the straight-line approximation is generally used to compute the matrix M. In such cases, the sampled-data and discrete representations of the loop gain become completely equivalent, and either representation can be used. In Part III of this thesis an example of this equivalence is encountered; there the discrete representation of the loop gain is used, since the focus is on the movement of system poles, of which the discrete model has only a finite number, while the sampled-data model has infinitely many. In other cases, however, it is much more convenient to use the sampled-data model. The analysis of measurements in Part II of this thesis provides one example; the continuous nature of the sampled-data model is required in this context. The close relationship between the sampled-data model and state-space averaging, to be discussed in the next section, also makes the use of the sampled-data model more convenient.

7.3 Sampled-data modeling versus state-space averaging

The relationships between sampled-data modeling and discrete modeling occurred strictly on an abstract, functional level, since the two representations had completely different forms. However, both the sampled-data and the state-space averaged models are continuous in nature, and it may be expected that

more physical relationships exist between these two techniques.

Indeed, a comparison of the Laplace transformed block diagrams of the two in Fig. 7.1 reveals just such a relationship. This figure is adapted from Figs. 4.1 and 6.1, but includes the feedback paths not previously shown. The only substantial difference between the two block diagrams is the presence of the sampler in the sampled-data diagram. All of the differences between the two models can therefore be ascribed to this element, and one model can be transformed into the other by the addition or removal of this sampler, together with the addition of the delay ε, if necessary, to maintain causality.

One application of this result suggests itself immediately. An extension of state-space averaging is the formulation of equivalent linear circuits from the state-space averaged result [1]. These circuits can then be embedded in larger circuits and used for system analysis. The relationship just discovered allows the same technique to be used with the sampled-data model. The equivalent circuit remains the same, but now the duty ratio generators, corresponding to the $\widehat{U}(s)$ signal in Fig. 7.1a, become pulsed in nature, thereby including the effects of the sampler in Fig. 7.1b. This modification is illustrated in Fig. 7.2 for the canonical circuit model derived from state-space averaging [1]. For clarity, only the small-signal portion of the model is shown.

A similar comparison can be made of the time-domain equations for the two models, adopted from Eqs. (4.8) and (6.3) and rewritten here as Eq. (7.11).

$$\dot{\widehat{x}} = A\widehat{x} + b\widehat{v}_g + K\widehat{u} \qquad \text{(state-space averaging)} \tag{7.11a}$$

$$\dot{\widehat{x}} = A\widehat{x} + b\widehat{v}_g + K\widehat{u}^* \qquad \text{(sampled-data modeling)} \tag{7.11b}$$
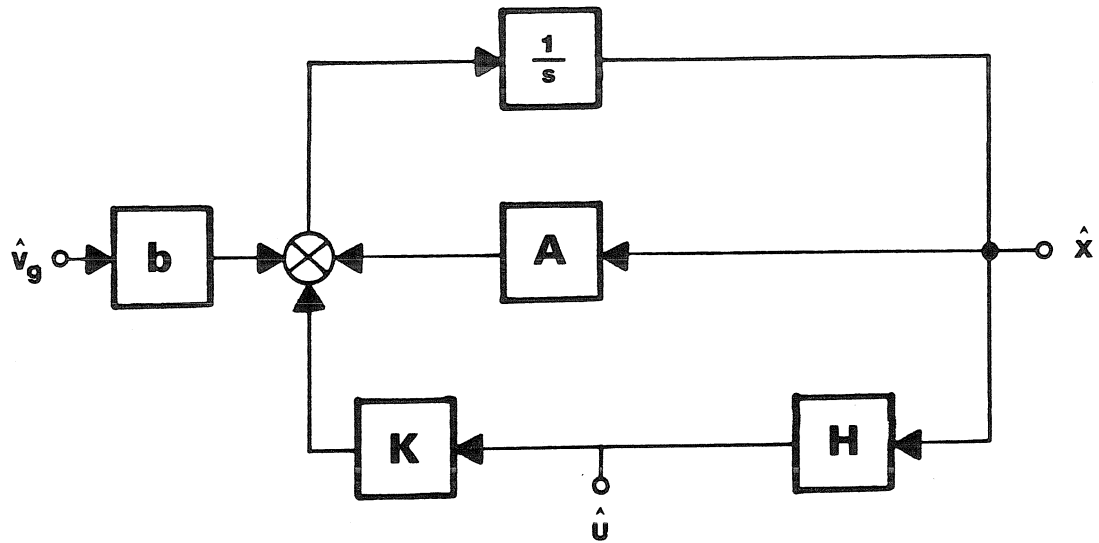
(a) state-space averaged block diagram
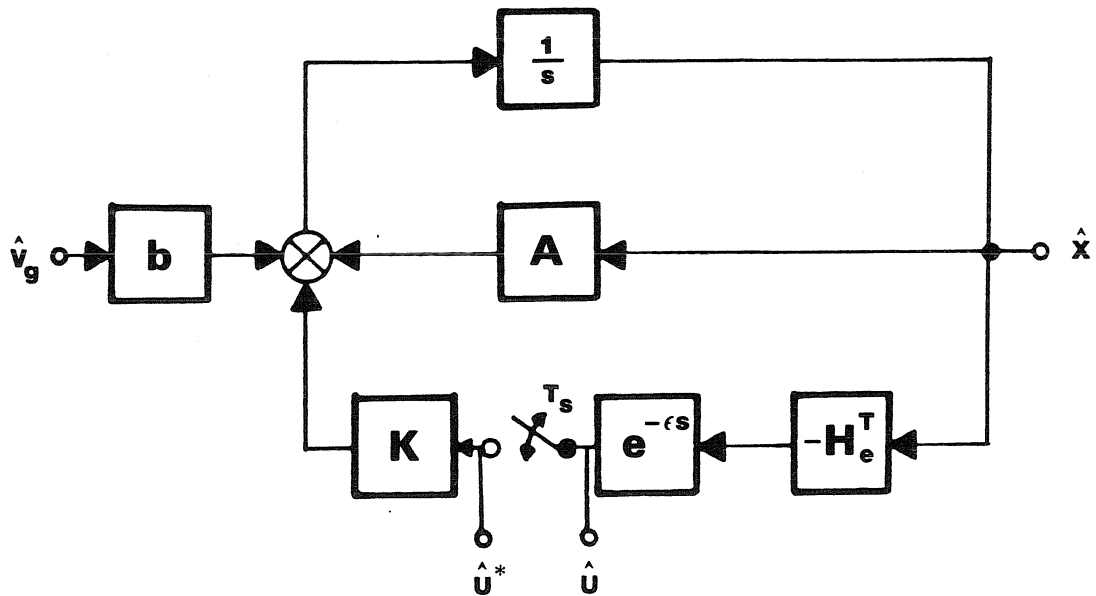
(b) sampled-data block diagram

Figure 7.1. *Comparison of the block diagrams of the state-space averaging and sampled-data models.*
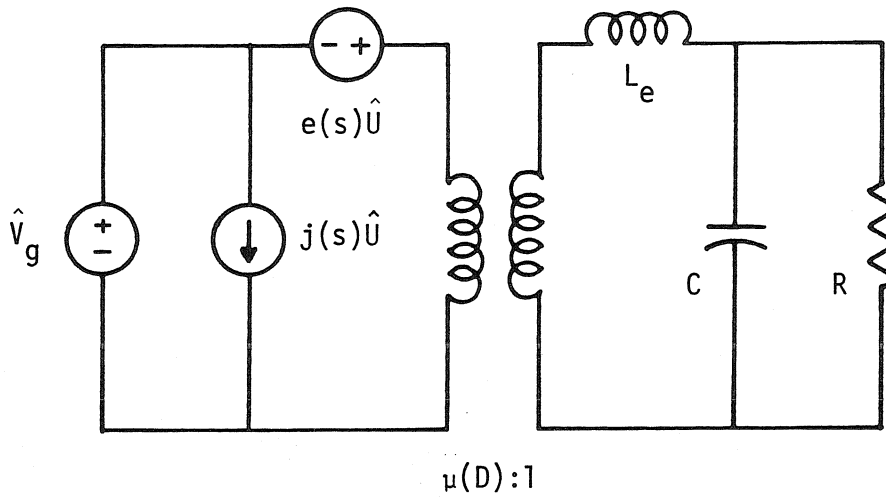
(a) canonical equivalent circuit: state-space averaging
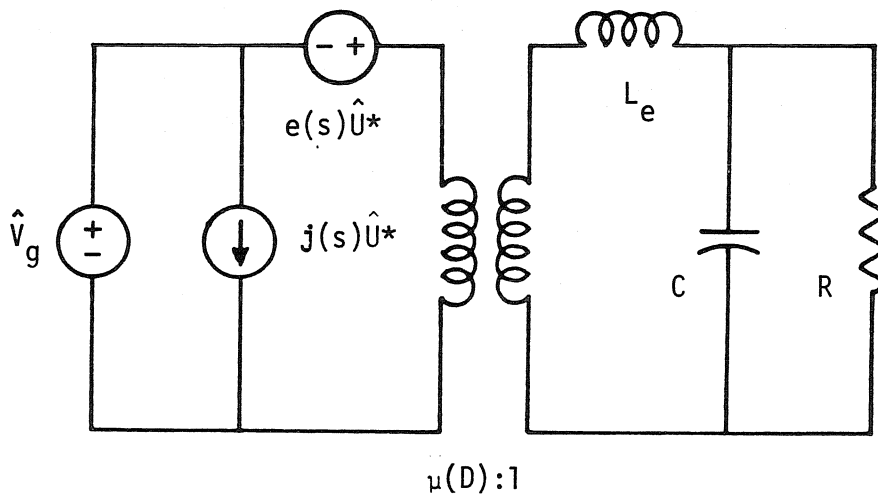
(b) canonical equivalent circuit: sampled-data modeling

Figure 7.2. *Modification of the canonical equivalent circuit for sampled-data modeling.*

$$\widehat{u}^{\circ} = \widehat{u}(t)T_s \sum_{n=-\infty}^{\infty} \delta[t - nT_s] \qquad (7.11c)$$

Again the difference between the two models is seen to lie in the sampled-data equation's pulsed driving waveform, which does not appear in the state-space averaged result.

Finally, a comparison of the two methods in the frequency domain can be undertaken. The loop gains for the two techniques are given in Eq. (7.12), adapted from Eqs. (4.11) and (6.9).

$$T_\varepsilon(s) = H_e^T e^{-\varepsilon s}(sI - A)^{-1}K \qquad \text{(state-space averaging)} \qquad (7.12a)$$

$$T_s^{\bullet}(s) = H_e^T[e^{-\varepsilon s}(sI - A)^{-1}]^{\bullet}K \quad \text{(sampled-data modeling)} \qquad (7.12b)$$

Here a small delay ε has been included in the state-space averaging result to stress its similarity with the sampled-data analysis. This addition does not affect the state-space averaged loop gain as it does the sampled-data one; there are no delta functions driving the state-space averaged equation, so infinitely fast signal propagation through the integrator is not a problem, and causality is already firmly established. Thus, when ε is made to go to zero, it will leave no effect on the state-space averaged loop gain.

With this slight modification, the sampled-data loop gain is just the sampled version of the state-space averaged loop gain.

$$T_s^{\bullet}(s) = [T_\varepsilon(s)]^{\bullet} \qquad (7.13)$$

In Appendix B a relationship, repeated here as Eq. (7.14), between the Laplace transform of a sampled function and that of its unsampled version is developed.

$$[T(s)]^\circ = \sum_{n=-\infty}^{\infty} T(s+jn\omega_s) \qquad (7.14)$$

This relationship is illustrated in Fig. 7.3 for a low-pass function $T(s)$, like those usually encountered in switching regulator analysis. As can be seen from the figure, at frequencies well below one-half the switching frequency the two func-tions agree almost exactly. Discrepancies only arise at relatively high frequen-cies, where overlap between successive reflections of the loop gain becomes significant. Thus, state-space averaging can be viewed as a limiting case of the more powerful sampled-data technique; the state-space averaged results are valid in situations where the system bandwidth is well below one-half the switch-ing frequency.

This result demonstrates that it is not always necessary to use the sampled-data model in the design of a regulator system. In many cases, the system bandwidth is limited to a value much less than the switching frequency by characteristics of the converter or controller. One example of such a charac-teristic is the existence of a right-half-plane zero in the loop gain. The differences between the state-space averaged and sampled-data models are superfluous here: the loop gain must be far below unity gain well before one-half the switching frequency, but, as was just shown, the sampled-data and state-space averaged loop gains diverge only at high frequencies.

The usefulness of the sampled-data analysis occurs when state-space averag-ing predicts stability even for system bandwidths very close to one-half the switching frequency. A common instance of this situation is that of a state-space averaged loop gain which looks like a single pole at high frequencies, and which therefore predicts stability for any value of gain. Consider such a single-
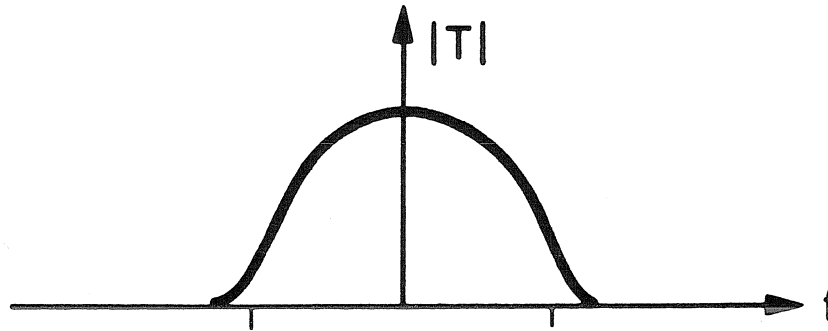
(a) unsampled loop gain
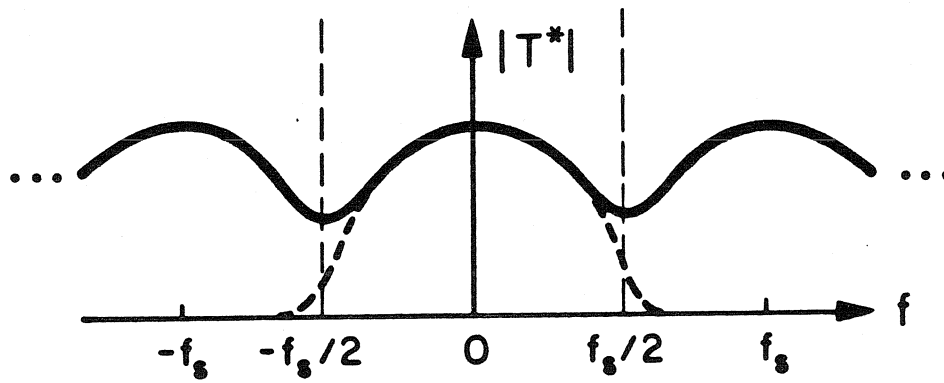
(b) sampled loop gain

Figure 7.3. *Relationship between unsampled and sampled loop gains.*

pole loop gain.

$$T(s) \ = \ \frac{2\pi f_c}{s} \qquad (7.15)$$

The corresponding sampled-data loop gain is easily calculated.

$$T_s^*(s) \ = \ \frac{2\pi f_c/f_s}{e^{sT_s} - I} \qquad (7.16)$$

In Eq. (7.16) the delay ε has already been made to vanish. The crossover frequency of the state-space averaged loop gain, the frequency at which $|T(s)| = 1$, is f_c, and the switching frequency is f_s. These two functions are plotted in Fig. 7.4 in the form of Bode plots, from which stability information can be easily obtained. Contrary to the state-space averaged prediction, the sampled-data loop gain indicates that instability can indeed occur. In fact, the case shown is on the verge of instability. The phase of the sampled loop gain falls to -180° just as the magnitude reaches one, at one-half the switching frequency. A condition for the maximum value of f_c for stability can be easily derived from Eq. (7.16).

$$f_c \ < \ \frac{f_s}{\pi} \quad \text{for stability} \qquad (7.17)$$

Of course, for an adequate stability margin, the value of f_c chosen must be considerably below the maximum allowable.

The relationship between the sampled-data and state-space averaged loop gains given in Eq. (7.14) is of mainly qualitative interest, providing a visualization of the connection between the two. Another, more quantitative relationship can also be developed, based on the equivalent representation of the sampled-
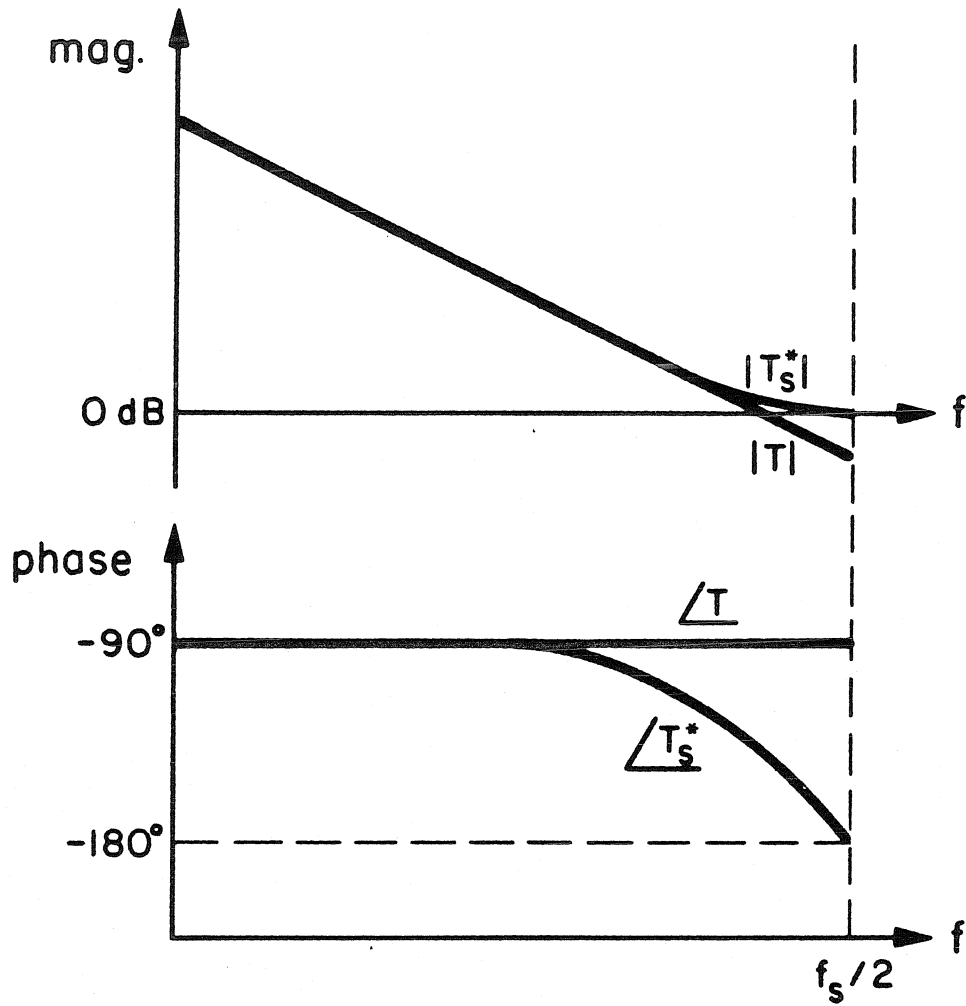
$$T(s) = \frac{2\pi f_p}{s} \quad , \quad T_s^\bullet(s) = \frac{2\pi f_p / f_s}{e^{sT_s} - 1}$$

Figure 7.4. *Comparison of the state-space averaging loop gain* $T(s)$ *and the sampled-data gain* $T_s^\bullet(s)$ *for a single-pole system.*

data loop gain $T_s^\bullet(s)$ given in Eq. (7.9), repeated here as Eq. (7.18).

$$T_s^\bullet(s) = H_e^T(e^{sT_s}I - e^{AT_s})^{-1}e^{AT_s}KT_s \qquad (7.18)$$

The straight-line approximation permits the replacement of the exponential matrix e^{AT_s} by the first two terms of its Taylor series expansion. Suppose the exponential form e^{sT_s} is similarly approximated by the first two terms of its Taylor series. This step is equivalent to the assumption that the frequencies of interest are much less than the switching frequency.

$$e^{sT_s} \approx 1 + sT_s \ , \ \ sT_s << 1 \qquad (7.19)$$

With these approximations the sampled-data loop gain $T_s^\bullet(s)$ can be rewritten in an approximate form.

$$T_s^\bullet(s)\Big|_{e^{sT_s} \to 1+sT_s} \approx H_e^T(sI-A)^{-1}(I + AT_s)K \qquad (7.20)$$

The matrix $I + AT_s$ acts as a correction to the vector K. Owing to the straight-line approximation, this correction is often small and may be assumed negligible with only a small loss of accuracy.

$$T_s^\bullet(s)\Big|_{e^{sT_s} \to 1+sT_s} \approx H_e^T(sI-A)^{-1}K = T(s) \qquad (7.21)$$

Thus, with this transformation, $e^{sT_s} \to 1+sT_s$, the sampled-data loop gain is transformed, to a good approximation, into the state-space averaged loop gain. As a test of this relation, consider the previous example, which treated the specific case of a state-space averaged loop gain with a single pole. An

application of the transformation to the sampled-data loop gain of Eq. (7.16)
should result in the recovery of the state-space averaged loop gain.

$$T_s^{\bullet}(s) = \frac{2\pi f_c / f_s}{e^{sT_s} - 1} \rightarrow \frac{2\pi f_c / f_s}{sT_s} = \frac{2\pi f_c}{s} \qquad (7.22)$$

The last expression matches the state-space averaged form, Eq. (7.15), and the
transformation is verified for this case.

Thus, the sampled-data and state-space averaged loop gains are approxi-
mately related by the transformation $e^{sT_s} \rightarrow 1 + sT_s$. Recall that the sampled-data
and discrete modeling loop gains were similarly related by a transformation
$e^{sT_s} \rightarrow z$. There is a difference between these two cases, however. The relation-
ship between discrete modeling and sampled-data modeling is valid for all fre-
quencies, reflecting the fact that the accuracies of the two techniques are com-
parable. However, the result of a transformation of a sampled-data loop gain via
the substitution $e^{sT_s} \rightarrow 1 + sT_s$ agrees with the original only at frequencies which
are low compared to the switching frequency. Otherwise, the transformation is
no more than a change of variables, with s at the end no longer being the true
complex frequency. This restriction reflects the fact that the two methods only
agree at low frequencies, with state-space averaging losing accuracy at higher
frequencies.

The relationships between the sampled-data and state-space averaged models
having been developed, it is well to conclude this section with a review of the ori-
gin of the difference between the two, specifically, the sampled-data model's
increased high-frequency accuracy. Both techniques utilize the straight-line
approximation, which allows the time-varying portions of the converter state
matrix and forcing vector to be neglected, with only their average values being

kept. However, the sampled-data technique stops at this point, retaining the pulsed nature of the duty ratio modulation function, while state-space averaging continues by replacing this pulse string by a smooth function. Thus, state-space averaging assumes that feedback can be applied continuously, at any frequency, while the sampled-data technique correctly asserts that control can be exercised at only one moment in each switching cycle. This property increases a regulator's tendency to oscillate at high frequencies, since the controller may not be able to act quickly enough to restrain state variations. The recognition of this tendency in the sampled-data model, and its neglect in state-space averaging, are the origins of the differences between the two methods.

7.4 Properties of the sampled-data loop gain

The previous two sections have emphasized the relationships between the new sampled-data modeling technique and the discrete and state-space averaged methods. In this present section attention will be focussed solely on the sampled-data method and in particular on the sampled-data loop gain. In many of its applications, for example, when displayed on Bode or Nyquist plots, the loop gain is considered to be a function not of the complex variable s, as it has been so far in this thesis, but rather of the frequency f. The discussion here will also restrict the loop gain's dependence to this range.

$$s = j\,2\pi f \tag{7.23}$$

When considered as a function of frequency, the sampled-data loop gain possesses certain general properties which cause its plotted characteristic to be quite striking. These features are readily discernible from a particular representation of this function. This form, derived in Section 7.2, is repeated

here as Eq. (7.24).

$$T_s^*(j2\pi f) = H_s^T(e^{j2\pi f/f_s}I - e^{AT_s})^{-1}e^{AT_s}KT_s \qquad (7.24)$$

One property of the sampled-data loop gain is derived by the replacement of the frequency f in Eq. (7.24) by $f + f_s$. Since $e^{j2\pi} = 1$, the sampled-data loop gain is unchanged by this substitution, and is therefore periodic, with the switching frequency f_s as the period. Recognition of a second characteristic results from evaluation of Eq. (7.24) for the cases $f = 0$ and $f = f_s/2$. Since $e^{j\pi} = -1$, and the other components are real vectors and matrices, in these two instances the loop gain T_s^* becomes purely real. The combination of this characteristic with the periodicity of the function implies that the sampled-data loop gain is real at each multiple of one-half the switching frequency.

Finally, consider the substitution $f = f_s - f$ in Eq. (7.24).

$$T_s^*[j2\pi(f_s - f)] = H_s^T(e^{-j2\pi f/f_s}I - e^{AT_s})^{-1}e^{AT_s}KT_s \qquad (7.25)$$

This expression also results from the evaluation of the complex conjugate of the loop gain at the frequency f.

$$\overline{T_s^*[j2\pi f]} = H_s^T(e^{-j2\pi f/f_s}I - e^{AT_s})^{-1}e^{AT_s}KT_s \qquad (7.26)$$

This step used the fact that the conjugate of a matrix inverse is the inverse of its conjugate. The resulting equality reveals two symmetries of the sampled-data loop gain.

$$T_s^*[j2\pi(f_s - f)] = \overline{T_s^*[j2\pi f]} \qquad (7.27)$$

Consideration of the magnitudes of the two expressions in Eq. (7.27) shows that the magnitude of the sampled-data loop gain possesses even symmetry about one-half the switching frequency. The imaginary component of this equation, on the other hand, implies that the imaginary part of the sampled-data loop gain must be odd about one-half the switching frequency. Hence, the phase is odd about its value at one-half the switching frequency. This particular value of the phase must be a multiple of 180°, since, as was shown earlier, the loop gain is real at this frequency.

The combination of these three findings with the low-pass nature of switching converters results in a picture of the sampled-data loop gain something like that in Fig. 7.5. This general figure is quite useful for the determination of certain design implications of the sampled-data loop gain. For example, it is evident from this figure that the highest possible loop gain crossover frequency is one-half the switching frequency: if the crossover frequency were any higher, the loop gain would never fall below unity magnitude, and instability would be unavoidable. This property is due to the fact that control is only exercised once in each switching cycle; the most rapidly varying signal which can be propagated through this discrete controller has a period of twice the switching period.

7.5 Conclusions

This chapter has compared the new sampled-data modeling technique with the discrete modeling and state-space averaging methods and has determined some general properties of the sampled-data loop gain. The discrete model and the sampled-data model were shown to be essentially two different representations of the same system. As such, they can be used interchangeably, according to convenience and the requirements of specific cases.
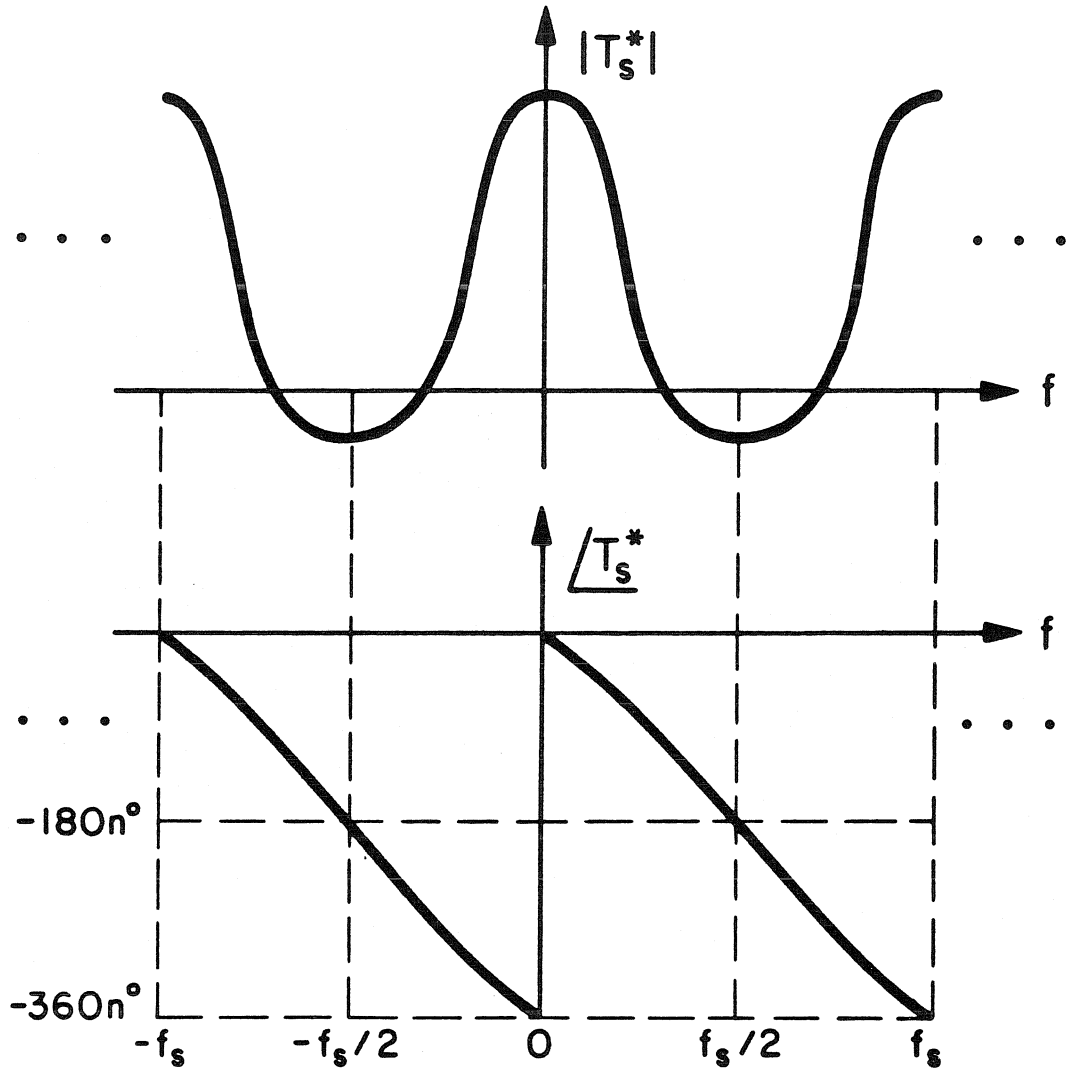
Figure 7.5. *General features of the sampled-data loop gain.*

On the other hand, differences between state-space averaging and the sampled-data method are known to exist; the discussion in this chapter described and illuminated these differences. On one level, the two techniques were shown to differ by the presence or absence of a sampler, which exists in the sampled-data representation but is missing from the state-space averaged model. Since this element is the only difference between the two, all the divergences in the predictions of the two models can be ascribed to it, and the equivalent circuits developed for state-space averaging can be easily modified to serve the sampled-data technique.

In the frequency domain it was seen that the loop gain of state-space averaging forms a low-frequency limiting case of the sampled-data loop gain, demonstrating that the two methods agree at low frequencies, where state-space averaging is known to be accurate. A particular case was examined in detail to show how the sampled-data model can be used to design in cases where state-space averaging predicts stability regardless of feedback gain. In a more general setting a transformation was developed which allows a sampled-data loop gain to be approximately converted to the corresponding state-space averaged version.

With this discussion serving as a framework, the developments of state-space averaging and sampled-data modeling were reviewed. It was seen that the smoothing of the pulsed driving function in state-space averaging allows that model to respond instantaneously to any perturbation, no matter how high its frequency, thus accounting for the relatively stable high-frequency behavior predicted by its analyses. In contrast, the pulsed nature of the sampled-data duty ratio modulation function correctly introduces delays which tend to cause instability at high frequencies if the feedback gain is too large.

Finally, the character of the sampled-data loop gain, as a function of real fre-quency, was examined. It was shown that this loop gain is periodic, with the switching frequency as the period, and is purely real at each multiple of one-half the switching frequency. In addition, it was seen that the magnitude of this function possesses even symmetry about one-half the switching frequency, while the phase is odd about its value at that same frequency. From the combination of these properties and the fact that switching converters are low-pass in nature, a general picture of the sampled-data loop gain was drawn. This form was seen to be useful in the design process, being employed, as an example, to show that the maximum possible bandwidth of a switching regulator is one-half the switching frequency.

CHAPTER 8

CONCLUSIONS

In Part I of this thesis, the development and high-frequency predictions of two switching regulator analysis methods, state-space averaging and discrete modeling, were compared. As a result of this comparison, a new modeling technique, the sampled-data method, was formulated.

Fundamental concepts of switching regulators and their analyses were presented in Chapters 2 and 3. These basic ideas included a description of the elementary converters and their operations and a design constraint, resulting from the necessity of low output voltage ripple, inherent to these circuits. This constraint led to the formulation of the straight-line approximation, which would later prove to be of great importance in the analysis of these systems. The concept of feedback was introduced to transform converters into regulators, and a particular kind of regulation scheme known as current-programming was discussed. This system possesses a well-known high-frequency instability which would later serve as a test of the predictions of modeling techniques. An equation describing the small-signal behavior of any converter was developed. While too complicated to be directly useful, this equation would form the basis of subsequent model derivations. Finally, the steady-state operation of switching converters was discussed briefly.

State-space averaging, a widely used modeling scheme, was treated in Chapter 4. Its governing idea is the modeling of a switching regulator by a linear, time-invariant matrix differential equation. Additionally, it can be used to formulate equivalent circuit models. Examination of its derivation revealed that, besides the small-signal assumption required for linearity, two approxima-

tions are involved. The first is related to the straight-line approximation, which had been justified previously. The second modification involves the smoothing of a pulsed driving signal into a continuous function. In a test of its high-frequency ability, state-space averaging failed to predict the known subharmonic instability in current-programmed regulators.

In Chapter 5, the discrete modeling technique was discussed. Rather than using a continuous model, it represents a regulator by a linear, shift-invariant matrix difference equation. It was seen that only the small-signal approximation is used in its derivation. The discrete modeling method accurately predicts the current-programming instability, and was seen to provide similar information for many designs which state-space averaging predicts are stable. However, the method's unusual form makes its application difficult for someone unaccustomed to discrete systems. Also, it is not suited to the frequency-domain measurements usually made on switching regulators.

Re-examination of the development of state-space averaging suggested that while the straight-line approximation is a good one, the smoothing of the pulsed driving function is unjustified. With use of only the straight-line approximation, a new model was developed in Chapter 6. The new method is called the sampled-data technique, because its form is that of a sampled-data system. The increased accuracy of the new model compared with state-space averaging was demonstrated by its ability to correctly predict the current-programming instability.

In Chapter 7, various relationships were developed between the new sampled-data model and the discrete and state-space averaged methods, and properties of the sampled-data loop gain were uncovered. The sampled-data and discrete models were seen to be two representations of the same system, via the

transformation $z = e^{sT_s}$, as long as the straight-line approximation holds. However, the continuous nature of the sampled-data model makes it more useful than the discrete model for the analysis of measurements and comparison with state-space averaging, which is also a continuous model. Such comparison showed that the sampled-data technique differs from state-space averaging only in the presence of a sampler in the feedback loop. This recognition led to the interpretation of state-space averaging as a low-frequency limiting case of the sampled-data method, approximately related to it by the transformation $e^{sT_s} \to 1 + sT_s$. The increased high-frequency accuracy of the sampled-data technique was directly traced to the smoothing of the pulsed driving function in the derivation of state-space averaging.

An examination of the sampled-data loop gain was then undertaken. It was seen that this loop gain, when considered to be a function of real frequency, is periodic, with the switching frequency as period, and that its imaginary part vanishes at each multiple of one-half the switching frequency. In addition, the magnitude of this loop gain displays even symmetry about one-half the switching frequency, while its phase is odd about its value at that frequency. From these properties, and the low-pass nature of switching converters, the general form of the sampled-data loop gain was determined, and was shown to be useful in the design process.

The findings discussed above are all consistent with the conclusion that the sampled-data analysis technique combines the accuracy of the discrete method with the continuous form of state-space averaging. Thus, this new technique is ideal for the investigation of many topics of interest involving switching regulators. Its continuous form mirrors the continuous nature of actual switching regulators, and its predictions can be relied upon even for frequencies approach-

ing one-half the switching frequency.

PART II

LOOP GAIN MEASUREMENTS

OF SWITCHING REGULATORS

CHAPTER 9

INTRODUCTION

The analysis techniques discussed in Part I of this thesis do not by themselves allow designs to be completed. Measurements are also an indispensable part of any design process, for only through tests of an actual circuit can the successful implementation of a design be confirmed. One powerful tool which links analysis and measurement is the quantity known as the loop gain. Loop gains were introduced in Part I of this thesis, in the course of an analysis of the accuracies of various modeling techniques. At that time, these loop gains were treated only as mathematical constructs, defined by their relationships with the modeling techniques' predicted closed-loop system poles. Loop gains are not, however, solely theoretical; they can also be measured in actual physical systems, yielding stability information about the system and allowing a comparison to be made with the theoretical prediction.

Of course, before these benefits can be realized, it is necessary to know what is to be measured. For linear, time-invariant systems, this problem has long been solved, as is suggested by the very name *loopgain* [12,13]. State-space averaging results in such a linear time-invariant model for switching regulators, so it is to be expected that the choice of the appropriate measurement to obtain the state-space averaged loop gain is straightforward. This supposition is correct, and the resulting measurement technique has proven useful in many applications. However, as shown in Part I of this thesis, at frequencies approaching one-half the switching frequency state-space averaging is no longer accurate, and therefore its measurement predictions cannot be trusted at high frequencies. The discrete modeling technique, on the other hand, possesses great accuracy but, being a discrete process, does not have a suitable form for

the analysis of measurements in the frequency domain.

Neither of these drawbacks is possessed by the sampled-data modeling technique, developed in Part I of this thesis. This new method combines the accuracy of the discrete technique with the continuous form of state-space averaging. Thus, it is perfectly suited to the analysis of switching regulator measurements. This part of this thesis will therefore focus on the application of the sampled-data method to the question of the determination of a suitable measurement for comparison with the sampled-data loop gain and to the interpretation of other measurements which are commonly made.

In Chapter 10 the fundamentals of conventional loop gain measurements in switching regulators are reviewed, including the state-space averaged analyses of these measurements. Then, in Chapter 11, the sampled-data technique is used to analyze both the conventional measurements and a new, somewhat exotic measurement. It is found that one of the conventional measurements is not useful as a predictor of stability in systems with large bandwidths. The new measurement is seen to give the true sampled-data loop gain, and the other conventional measurement, while not giving one of the theoretical loop gains encountered in Part I, does yield stability information.

In Chapter 12 experimental measurements made on a wide-bandwidth regulator are presented. These data illustrate the various types of measurements discussed in Chapter 11 and confirm the sampled-data analyses of them. Conclusions are offered in Chapter 13.

CHAPTER 10

FUNDAMENTALS AND STATE-SPACE AVERAGED ANALYSIS
OF LOOP GAIN MEASUREMENTS IN SWITCHING REGULATORS

10.1 Introduction

In this chapter, a fundamental loop gain measurement technique for switching regulators is reviewed, and the state-space averaged analysis of this measurement is presented. In Section 10.2 a common method for the measurement of loop gains in feedback circuits is described. Some special characteristics of switching regulators are then noted, along with the modifications required to adapt the basic measurement method to these systems.

A state-space averaged analysis of this measurement technique is undertaken in Section 10.3. The result is found to match the state-space averaged loop gain defined in Part I of this thesis. Furthermore, with just one potential difference, the same result is obtained if the feedback loop is not even closed, provided the proper converter bias can be maintained. The possible difference is a change in the overall scale of the loop gain magnitude, caused by the interaction of switching ripple on the fed-back waveform with the artificial ramp of the modulator. Finally, it is recalled from Part I that state-space averaging loses accuracy at frequencies near one-half the switching frequency and that therefore the results of the state-space averaged measurement analysis must be viewed with care in the high-frequency region. Conclusions are presented in Section 10.4.

10.2 Basics of loop gain measurements

The quantity known as the loop gain is of fundamental importance in both the analysis and measurement phases of the design of feedback circuits.

Analytically the loop gain is important because the complex frequencies at which the loop gain attains the value -1 are the closed-loop poles of the system. Consequently, Nyquist and Bode techniques can be applied to obtain stability information. In addition to this property, however, the loop gain of a circuit can also be measured, providing an excellent tool for design verification.

Techniques for loop gain measurement in linear, time-invariant circuits have been extensively described [12,13]. One of the most common methods, and the one which will be adopted here, requires the existence of a point in the feedback loop where a low impedance source drives a high impedance load, as in Fig. 10.1. If a new sinusoidal source v_z is inserted in the loop between the original source and load, and the signals v_x and v_y, as shown in the figure, are measured, the ratio v_y/v_x is the loop gain at the frequency of v_z.

This technique is, with several qualifications, applicable to switching regulators. One complication is that a switching regulator often contains multiple feedback loops. Thus, there may exist many topologically distinct places at which to inject signals, each yielding a different measurement, and the location corresponding to a given theoretical loop gain may not be obvious. Fortunately, however, switching regulator feedback systems are special in that, because the duty ratio is the only control input, all the feedback loops must meet at one point, the duty ratio modulator input. The theoretical analyses of Part I of this thesis implicitly utilized this characteristic by deriving the loop gain from an expression for the duty ratio modulation. In addition, this position, illustrated in Fig. 10.2, usually satisfies the impedance requirements described above and is therefore a natural place to choose for signal injection. Indeed, this choice will be seen to lead to measurements which can be compared directly with the loop gains derived in Part I.

$$T = \frac{v_y}{v_x}$$
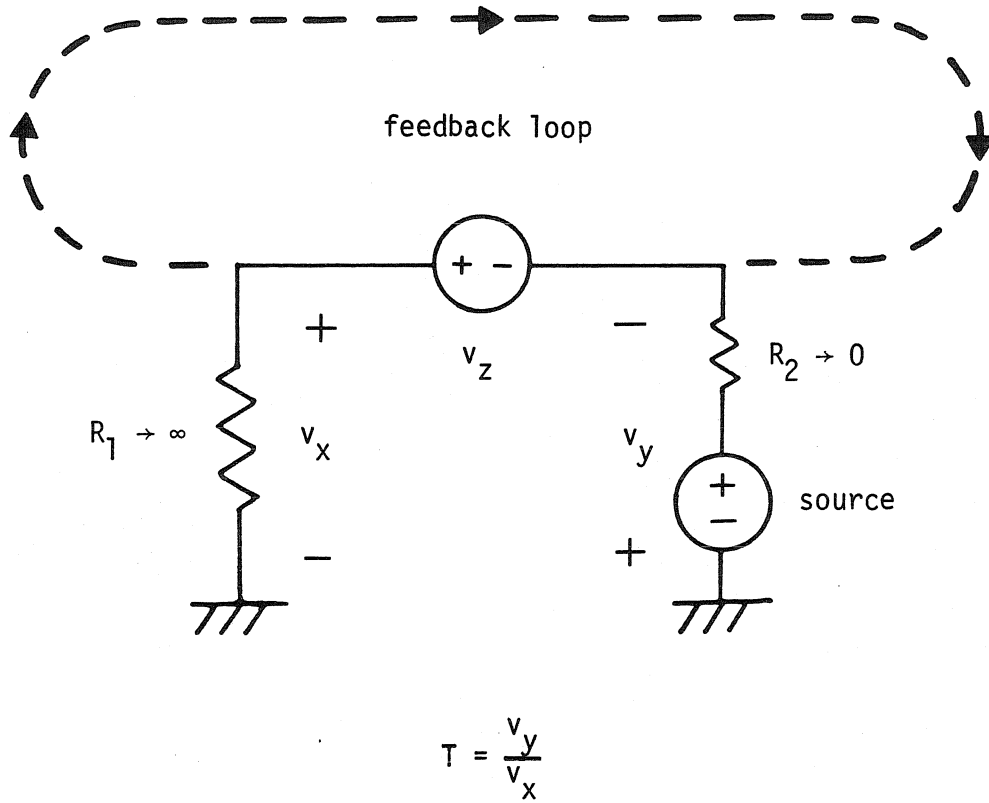
Figure 10.1. *Common technique for measuring the loop gain T.*
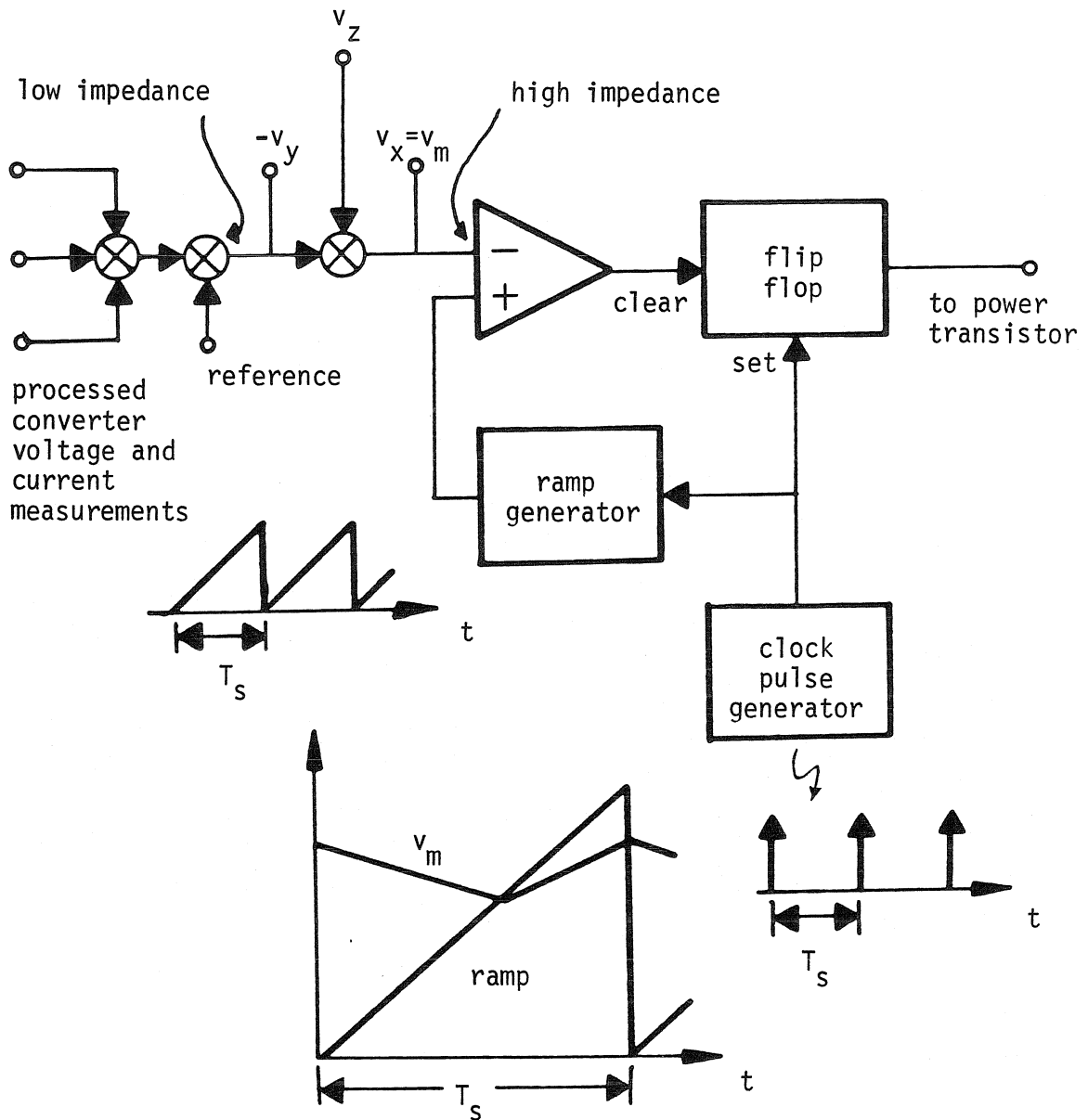
Figure 10.2. *Controller topology, illustrating signal injection for loop gain measurement.*

A second modification is due to the noise created by the switching process, which must be removed from the measured signals before accurate results can be obtained. Fortunately, a network analyzer system possesses tracking, narrow-band filters which automatically perform this function. Such an instrument was used for the measurements described in this thesis. Additionally, the network analyzer system used was operated under computer control, with use of software developed for this purpose [14]. This software control allowed measurements to be made rapidly and accurately, with automatic protection against excessive noise or signal overload.

Finally, and most importantly, it must be remembered that a switching regulator is not, in reality, a linear, time-invariant system. Even its small-signal behavior, while linear, is not time-invariant. The effects of this characteristic on measurement results provide the focus of the analysis in this part of this thesis.

10.3 State-space averaging loop gain predictions

Before an investigation of these time-varying effects is undertaken, however, the predictions of a linear, time-invariant model, the state-space averaged model, will be reviewed. The popularity of state-space averaging has made it an obvious candidate for use in the formulation of loop gain measurement analysis. The block diagram which summarizes the state-space averaged model of a switching regulator is repeated in Fig. 10.3a (see Eq. (4.8) and Fig. 7.1a). This block diagram can be put into a more standard form by the application of the Laplace transformation and the combination of the integrator and state matrix, as in Fig. 10.3b.

Source modulation $\hat{v}_g$ is eliminated in a loop gain measurement, so, with signal injection $\hat{v}_z$ occurring at the input of the modulator, the resulting block
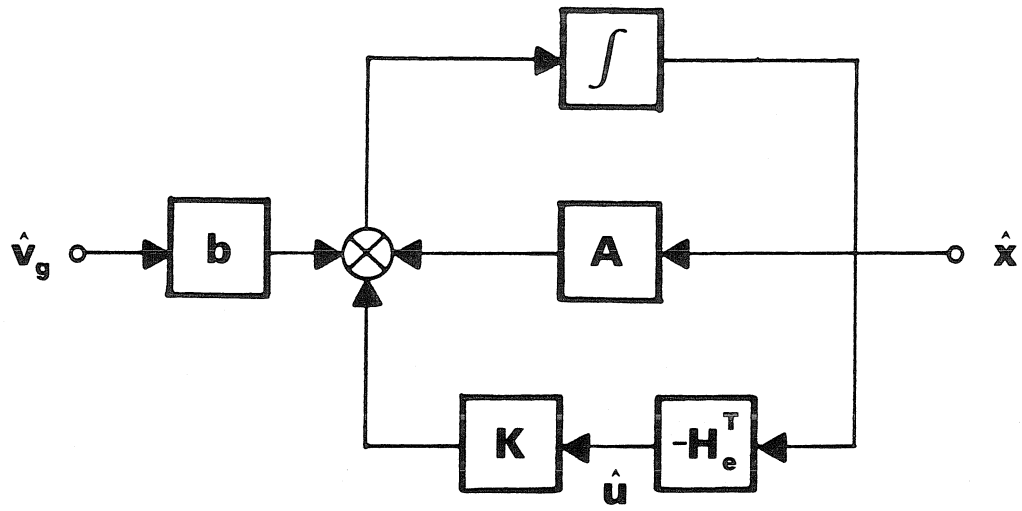
(a) time-domain model
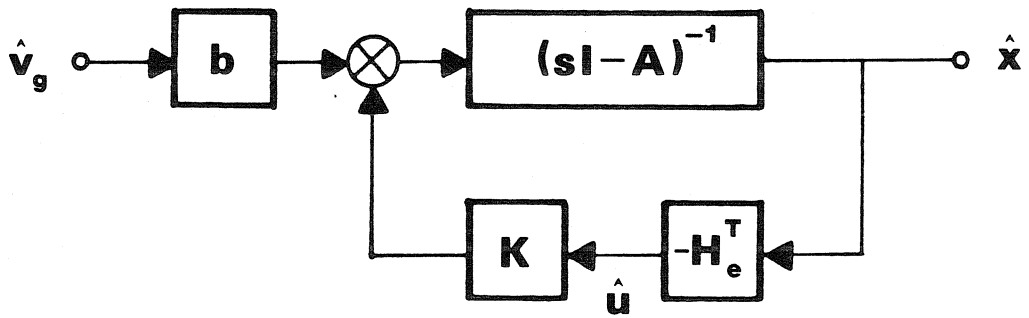
(b) frequency-domain model

Figure 10.3. *State-space averaged model of a switching regulator.*

diagram of the measurement setup appears as in Fig. 10.4. Here the effective
gain vector H_e has been split into two factors in order to accurately reflect the
measurement technique.

$$H_e = G_m H \tag{10.1}$$

One factor, the vector H, represents the feedback gains which are explicity used
in the circuit. The second, the scalar gain G_m, models the gain produced by the
modulator. The injection point lies between these two elements, and the loop
gain signal component $\hat{v}_x$ is just the modulator input signal $\hat{v}_m$. The duty ratio
modulation function $\hat{u}$ is also shown, following the modulator block. Note that
in Fig. 10.4 the loop path is vectorial in nature everywhere but at the point of
signal injection. This characteristic reflects the fact, stated earlier, that in
switching regulators all the feedback paths meet at the modulator input, which
is therefore an appropriate choice for the injection point.

Analysis of this block diagram for the loop gain is straightforward.

$$\hat{v}_y(s)/\hat{v}_x(s) = H^T(sI - A)^{-1}G_m K \tag{10.2a}$$

$$= H_e^T(sI - A)^{-1}K \tag{10.2b}$$

Note that this result is, as desired, exactly the state-space averaged theoretical
loop gain $T(s)$ found in Part I in Chapter 4. Thus, state-space averaging predicts
that the procedure just described can be used to compare the theoretical loop
gain with the measured loop gain of the circuit under test.

An interesting extension of this analysis is to note that the prediction of
Eq. (10.2) is also obtained if the feedback loop is broken entirely, as in Fig. 10.5,
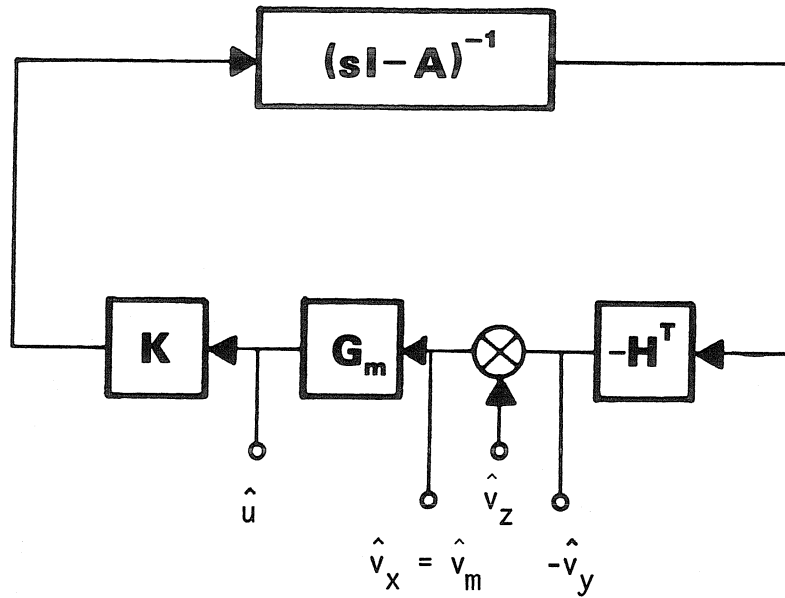
Figure 10.4. *State-space averaged block diagram of loop gain measurement with the feedback loop closed.*
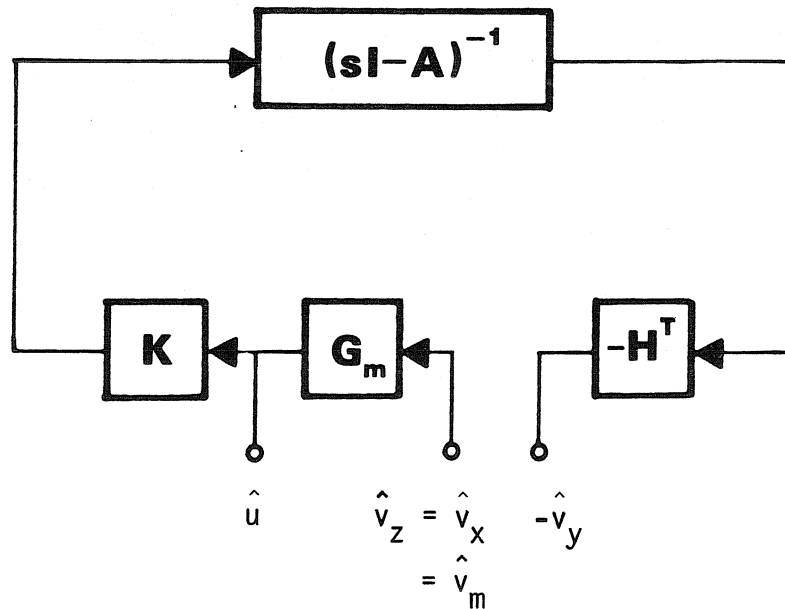
Figure 10.5. *State-space averaged block diagram of loop gain measurement with the feedback loop open.*

with the steady-state conditions maintained by external control of the duty ratio. Not all regulators can be operated in this open-loop fashion, but the meaurement of many systems is accomplished in this manner.

Although the forms of the open-loop and closed-loop state-space averaged predictions are the same, one factor in the loop gain expression, Eq. (10.2), may be different in the two cases, even if the measurements are performed on the same system. This element is the modulator gain G_m, which may be affected in the closed-loop case by interactions between the artificial ramp of the modulator and any switching ripple on the fed-back waveform. This switching ripple may act as an additional ramp, altering the effective modulator gain, as illustrated in Fig. 10.6. In this diagram, Fig. 10.6a displays a case in which, as in the open-loop case, the switching ripple on the fed-back waveform is negligible compared to the artificial ramp. In Fig. 10.6b, which might represent the closed-loop case, the switching ripple on the fed-back waveform interacts with the artificial ramp to reduce the effective modulator gain. The effect of this possible difference is a change in scale of the loop gain's magnitude characteristic. The phase characteristic is unaffected.

Thus, the state-space averaged analysis of loop gain measurements is seen to be rather straightforward. However, it was demonstrated in Part I of this thesis that, because state-space averaging neglects the time-varying nature of switching regulators, its predictions may not be accurate as the frequencies of interest approach one-half the switching frequency. Hence, the measurement analyses performed in this chapter cannot be trusted in the high-frequency region. Inevitably, as performance requirements on regulators become more severe, the bandwidths necessary to achieve specified transient performance will begin to enter this high-frequency range. To assure adequate stability margins for these
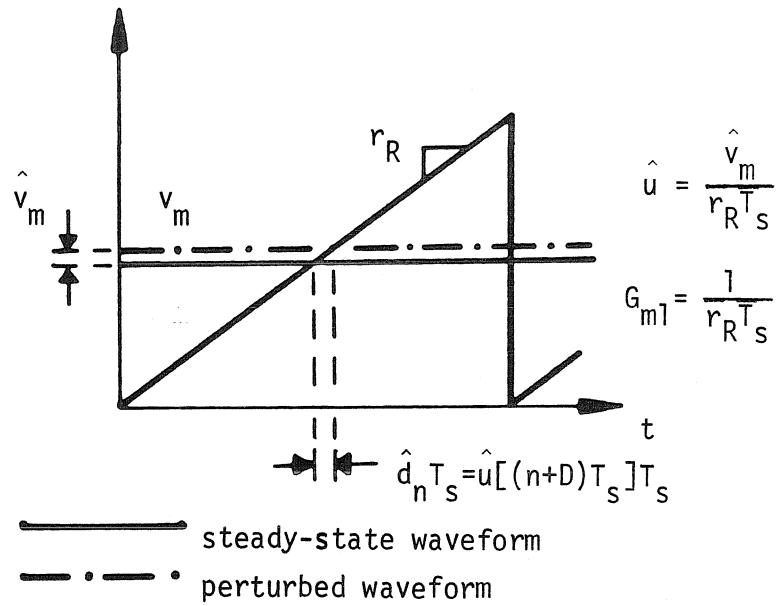
(a) negligible switching ripple
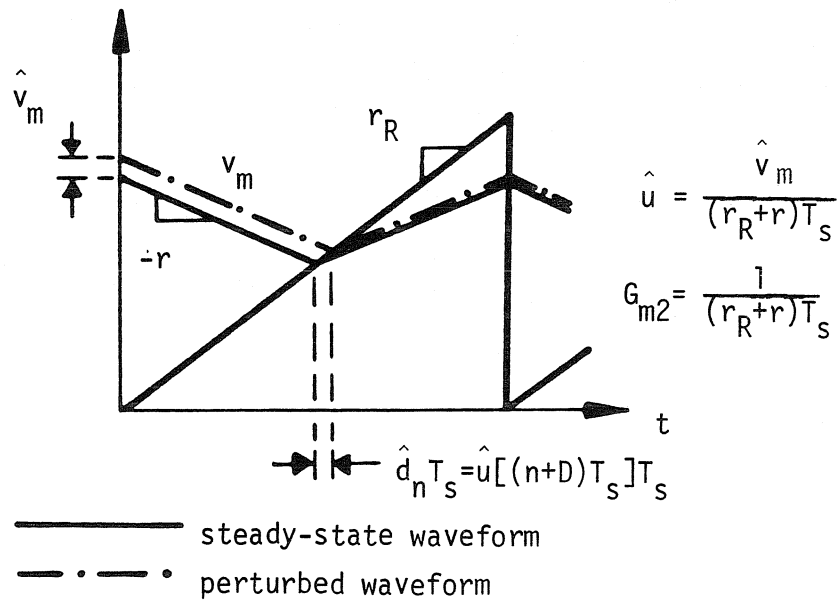
(b) significant switching ripple of slope -r

Figure 10.6. *Effect on modulator gain G_m of switching ripple on modulator signal v_m.*

systems, analyses must be accurate and measurements well understood even at these high frequencies. This need provides the motivation for the next chapter, in which the newly developed sampled-data modeling technique, which possesses excellent accuracy even at high frequencies, is used to analyze the measurements discussed in this chapter.

10.4 Conclusions

This chapter presented the basic elements of loop gain measurements in switching regulators and the analysis of these measurements by state-space averaging. A standard injection technique for measuring loop gains in linear, time-invariant circuits was described. This method was then shown to be adaptable to switching regulators by the choice of the modulator input, the location where all of the potential feedback loops must meet, as the injection point and by the use of narrow-band, tracking voltmeters to filter out the switching noise. It was noted that the time-varying nature of switching regulators can affect the measurement results.

An analysis of this measurement setup by state-space averaging, a time-invariant model, predicted that the measurement result would be identical to the state-space averaged theoretical loop gain defined in Part I of this thesis. In addition, nearly the same result was predicted if the feedback loop was open during the measurement, with the only possible difference being a magnitude scale change caused by a change in the modulator gain between the open-loop and closed-loop cases. Specifically, the closed-loop modulator gain can be affected by switching ripple on the fed-back signal applied to the modulator, ripple which is not present at the modulator in the open-loop case. This switching ripple can interact with the artificial ramp of the modulator and thereby change

the modulator's effective gain from its value in the open-loop case.

Finally, it was recalled that state-space averaging had been previously shown to be inaccurate at frequencies near one-half the switching frequency. Therefore, the predictions developed in this chapter cannot be used with confidence in that frequency range. This deficiency serves as the motivation for the next chapter, in which the more accurate sampled-data method will be applied to the formulation of measurement predictions which are valid even at high frequencies.

CHAPTER 11

SAMPLED-DATA ANALYSIS OF LOOP GAIN MEASUREMENTS

11.1 Introduction

The previous chapter used a conventional technique, state-space averaging, to analyze two conventional loop gain measurements, one with the feedback loop closed, and the other with the loop open. The analyses predicted that both measurements would match the state-space averaged loop gain, with a possible difference in magnitude scale, owing to different modulator gains in the two cases.

These predictions are valid at low frequencies, but state-space averaging loses accuracy at frequencies approaching one-half the switching frequency. In this chapter the new sampled-data technique, which possesses good accuracy even at high frequencies, is used to analyze these same two loop gain measurements, as well as a new, somewhat exotic measurement. It is found that, while all three measurement results agree in form at low frequencies, they may differ at high frequencies and, more importantly, vary in their degrees of usefulness in regulator design.

In Section 11.2 the basic measurement setup is modeled by a sampled-data block diagram. The open-loop measurement is considered in Section 11.3 and is found to give the state-space averaged loop gain as a result. It is therefore determined not to be useful as a predictor of stability in wide-bandwidth systems. In Section 11.4 a new loop gain measurement is described, in which the component signals of the loop gain are sampled before they are measured. Analysis of this measurement shows that the result should match the theoretical sampled-data loop gain. The conventional closed-loop measurement is

analyzed in Section 11.5. The result turns out to be a combination of the state-space averaged and sampled-data loop gains but nevertheless is an accurate predictor of stability. The state-space averaged prediction is seen to match this result for all but wide-bandwidth systems. Conclusions are offered in Section 11.6.

11.2 Sampled-data block diagram for use in measurement analysis

The formulation of loop gain predictions with the use of the sampled-data technique proceeds similarly to that in the state-space averaging case. The starting point consists of the two Eqs. (6.6) and (6.7), rewritten here as Eq. (11.1).

$$\hat{X}(s) = (sI - A)^{-1}b\hat{V}_g(s) + (sI - A)^{-1}K\hat{U}^{\bullet}(s) \tag{11.1a}$$

$$\hat{U}^{\bullet}(s) = -H_e^T[e^{-\varepsilon s}\hat{X}(s)]^{\bullet} \tag{11.1b}$$

In this equation a zero initial state is assumed. Recall that the delay ε is added to maintain causality, and that ε is eventually allowed to go to zero. This equation is easily put into block diagram form, shown in Fig. 11.1. As in the state-space averaged block diagrams, Figs. 10.4 and 10.5, the effective feedback gain vector H_e is split into two factors, the modulator gain G_m and the feedback gain vector H, in order to accurately mirror the measurement setups to be discussed.

In this Laplace-transformed block diagram the sampler is included to show where continuous Laplace transforms are changed to their sampled counterparts. Note that the sampler does not exist physically in the regulator circuit; it is a construct of the modeling process. Nevertheless, the sampler provides the
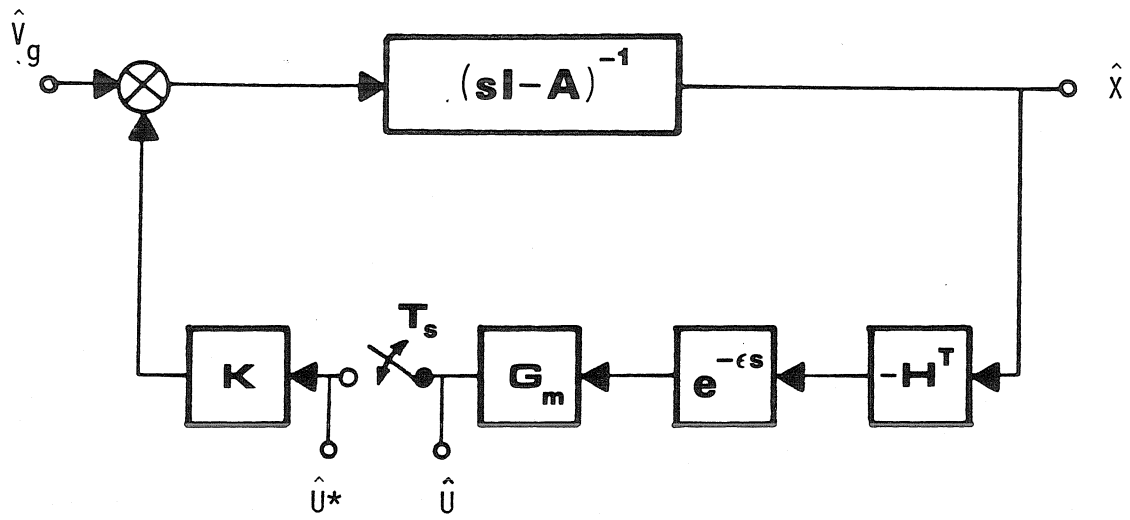
Figure 11.1. *Block diagram of the sampled-data model.*
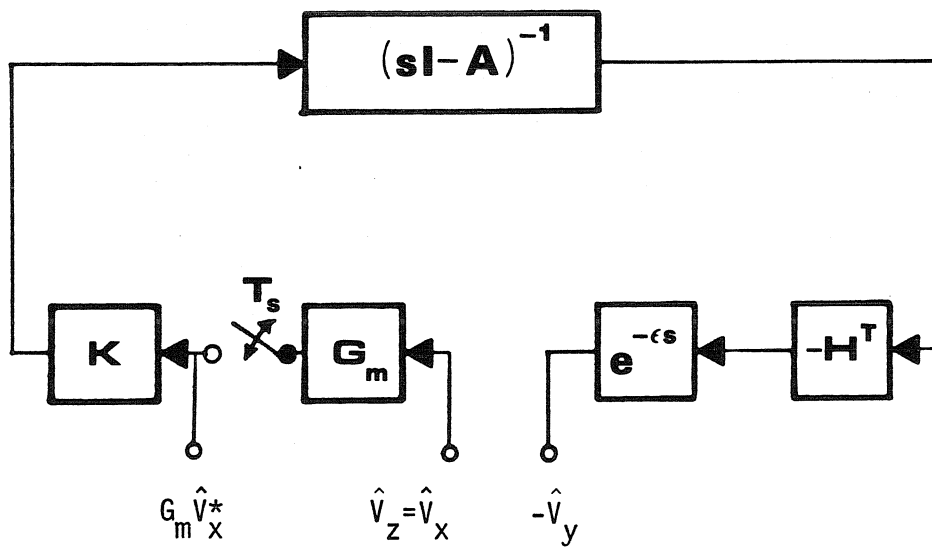
Figure 11.2. *Sampled-data block diagram for loop gain measurement with the feedback loop open.*

key to the formulation of accurate predictions of loop gain measurements in switching regulators, for it represents the time-varying nature of the regulator in a way which allows this behavior to be taken into account simply and accu- rately.

With the block diagram of Fig. 11.1, various measurement schemes can be analyzed. Three setups which will be considered here are the open-loop and closed-loop measurements discussed in Section 10.3, and a closed-loop, sampled measurement not previously discussed. For these as for all measurements of loop gains, the source $\hat{v}_g(t)$ is assumed to be zero.

11.3 Sampled-data analysis of loop gain measurement with feedback loop open

Signal injection of a sinusoid $\hat{v}_z$ of frequency ω_0 with the feedback loop open is represented in block diagram form in Fig. 11.2. Note that the injected signal $\hat{v}_z$ is equal to the signal $\hat{v}_x$ in this arrangement. The signals $\hat{v}_x$ and $\hat{v}_y$ are fed to the network analyzer, which extracts the component at frequency ω_0 from each signal and divides these two components to determine the loop gain. To predict the result of this measurement, therefore, it is necesary to relate the ω_0 components of the signals $\hat{v}_x$ and $\hat{v}_y$.

An expression for $\hat{V}_y(s)$ in terms of the sampled Laplace transform $\hat{V}_z^*(s)$ can be written down immediately.

$$\hat{V}_y(s) = e^{-\epsilon s} H_e^T (sI - A)^{-1} K \hat{V}_z^*(s)$$

(11.2a)

$$H_e = C_m H$$

(11.2b)

The spectrum of the signal $\hat{V}_z^*(s)$ consists of an infinite number of sinusoidal components, expressed in terms of the spectrum $\hat{V}_z(s)$ by a relation developed

in Appendix B and repeated here as Eq. (11.3).

$$\hat{V}_x^{\bullet}(s) = \sum_{n=-\infty}^{\infty} \hat{V}_x(s + jn\,\omega_s) \qquad (11.3)$$

However, only one of these components contributes to the component of $\hat{v}_y$ measured by the analyzer.

$$[\hat{v}_y]_{\omega_0} = H_s^T(j\omega_0 I - A)^{-1}K[\hat{v}_x^{\bullet}]_{\omega_0} \qquad (11.4)$$

In this equation the brackets denote a single frequency component of the enclosed signal, and the subscript gives the frequency in question. This notation has approximately the same content as the standard phasor notation used in sinusoidal steady state analysis. Note also that the delay ε has been allowed to go to zero in this equation; the delay's effects are only significant in sampled Laplace transforms.

For an arbitrary signal $\hat{v}_x$ Eq. (11.4) would not be useful. Aliasing effects of the sampling process would make it impossible to recover the component of $\hat{v}_x$ at frequency ω_0 from that of $\hat{v}_x^{\bullet}$ at that frequency. This overlap is illustrated in Fig. 11.3a. However, for the special case where $\hat{v}_x$ is a single pure sinusoid, no overlap occurs, as shown in Fig. 11.3b. In this case the component of $\hat{v}_x^{\bullet}$ at frequency ω_0 is the component of $\hat{v}_x$ at that frequency, which is just $\hat{v}_x$ itself. With this substitution Eq. (11.4) provides exactly the information needed for a measurement prediction.

$$\frac{[\hat{v}_y]_{\omega_0}}{[\hat{v}_x]_{\omega_0}} = H_s^T(j\omega_0 I - A)^{-1}K \qquad (11.5)$$
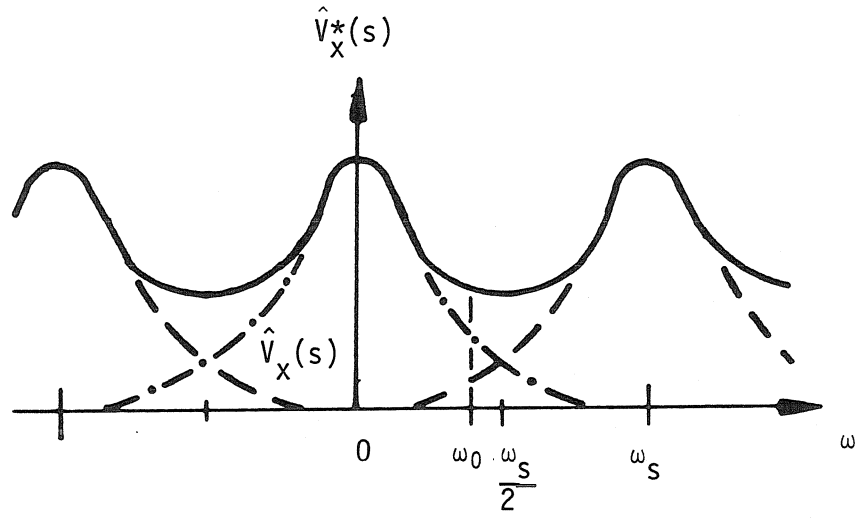
(a) arbitrary $\hat{v}_x(t)$
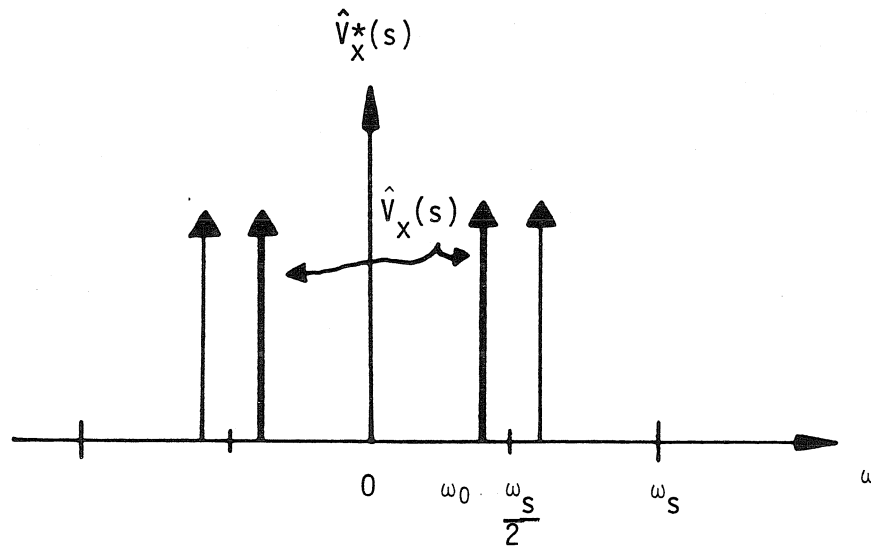
(b) $\hat{v}_x(t)$ a pure sinusoid

Figure 11.3. *Relationship between $\hat{V}_x(s)$ and $\hat{V}_x^\bullet(s)$.*

As a digression, a point of potential confusion in this analysis is now examined. It was stated that for $\hat{v}_x$ a pure sinusoid no frequency overlap occurred, and a figure showing the spectrum of the corresponding sampled signal $\hat{v}_x^{\bullet}$ as a series of delta functions confirmed that assertion. However, is this array of spikes the actual spectrum of $\hat{v}_x^{\bullet}$?

Laplace transform analysis seems to say no. The Laplace transform of the complex exponential $e^{j\omega_0 t}$ is easily calculated.

$$L(e^{j\omega_0 t}) = \frac{1}{s - j\omega_0} \tag{11.6}$$

This expression does not in the least resemble a delta function, and in fact has infinite frequency extent. It might therefore be expected that aliasing effects would occur even for the case where $\hat{v}_x$ is a sinusoid.

A different picture is obtained, however, if the Fourier transform is used instead of the Laplace transform. The Fourier transform of a pure sinusoid is, in fact, a delta function, as employed in Fig. 11.3b. Which view is correct? The resolution of this puzzle lies in the definitions of the two transforms. In its efforts to improve convergence, the Laplace transform must assume that any function to be transformed is identically zero for times less than zero. Hence the spectrum spreads out. On the other hand, the Fourier transform, at the expense of good convergence properties, transforms the complete function. The infinite temporal extent of a sinusoid in this case sharpens the spectrum into a single delta function.

Network analyzers, of course, do not set functions to zero for times less than a certain value. As the measurement interval lengthens, the readings of the analyzer approach the Fourier transform values. Hence, the original analysis

and predicted result of this measurement are indeed correct.

With the digression completed, attention is now returned to the predicted loop gain measurement result, Eq. (11.5). It is seen that the expression matches the state-space averaged theoretical loop gain, Eq. (4.11), and in fact is the same as the prediction for the state-space averaged analysis in the previous chapter. However, the significance of this result is quite different in the present context from that in Chapter 10. In the state-space averaged picture this result meant that the open-loop measurement was useful for stability analysis, if the previously discussed possible shift in modulator gain C_m was taken into account. In the sampled-data view of things, however, just the opposite is true, because it was shown in Part I that the state-space averaged loop gain cannot be used with confidence at high frequencies. Hence, the sampled-data analysis concludes that, for wide-bandwidth regulators, the open-loop measurement does not provide an adequate stability prediction. In the next section, a more exotic measurement is described which does yield stability information and which in fact results in the sampled-data loop gain.

11.4 Sampled-data analysis of loop gain measurement with feedback loop closed and signals sampled

The sampled-data analysis in Part I of this thesis showed that the theoretical loop gain which yielded accurate predictions at frequencies approaching one-half the switching frequency was given by the expression in Eq. (6.9), repeated here as Eq. (11.7).

$$T_s^{\bullet}(s) = H_e^T[e^{-\varepsilon s}(sI - A)^{-1}]^{\bullet}K \quad , \quad \varepsilon \to 0 \tag{11.7}$$

For comparison with theory, a measurement which resulted in this quantity

would be convenient. It turns out that such a measurement is possible, although it is not as simple to make as the measurement described previously.

Consider the sampled-data block diagram in Fig. 11.4. Note the two additional samplers in this network. Unlike the original sampler in the feedback loop, which is a construct of the modeling process and not accessible, the two new samplers are physical elements and must be added to the circuit to make the measurement. The pulse strings $\widehat{v}_x^{\,\bullet}$ and $\widehat{v}_y^{\,\bullet}$ are fed to the network analyzer, which, as usual, filters these two signals and measures the quotient of their components at frequency ω_0. The result is easy to predict, since the relation between the sampled Laplace transforms $\widehat{V}_x^{\,\bullet}(s)$ and $\widehat{V}_y^{\,\bullet}(s)$ is straightforward.

$$\widehat{V}_y(s) = H_\varepsilon^T e^{-\varepsilon s}(sI - A)^{-1}K\,\widehat{V}_x^{\,\bullet}(s) \tag{11.8a}$$

$$\widehat{V}_y^{\,\bullet}(s) = H_\varepsilon^T [e^{-\varepsilon s}(sI - A)^{-1}]^{\bullet} K\,\widehat{V}_x^{\,\bullet}(s) \tag{11.8b}$$

The already sampled signal $\widehat{V}_x^{\,\bullet}(s)$ is not affected by further sampling, and therefore factors out of the sampled product. This result is precisely what is desired for a measurement of $T_s^{\bullet}(s)$.

$$\frac{[\widehat{v}_y^{\,\bullet}]_{\omega_0}}{[\widehat{v}_x^{\,\bullet}]_{\omega_0}} = H_\varepsilon^T [e^{-j\varepsilon\omega_0}(j\omega_0 I - A)^{-1}]^{\bullet} K \tag{11.9a}$$

$$= T_s^{\bullet}(j\omega_0) \tag{11.9b}$$

Of course, in the calculation of the loop gain, the delay ε is eventually allowed to go to zero.
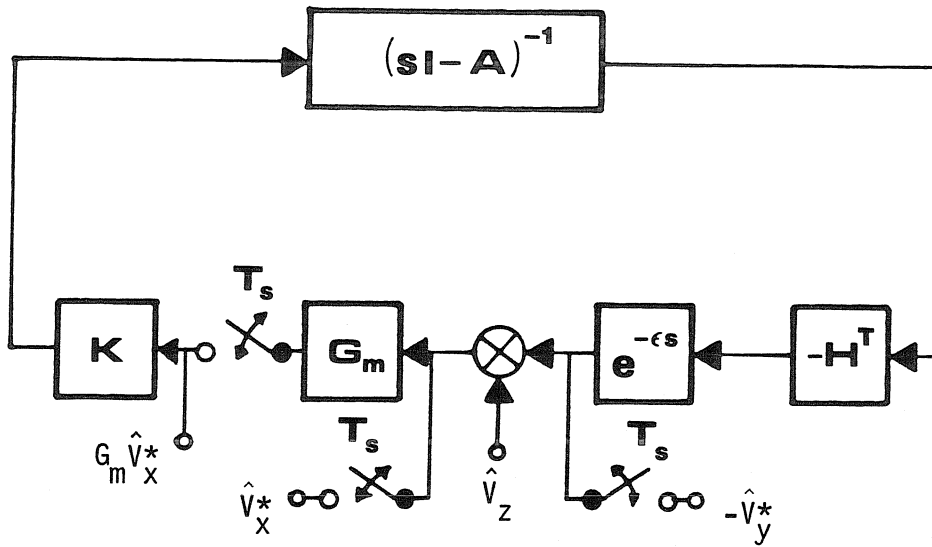
Figure 11.4. *Sampled-data. block diagram for loop gain measurement with the feedback loop closed and signals sampled.*
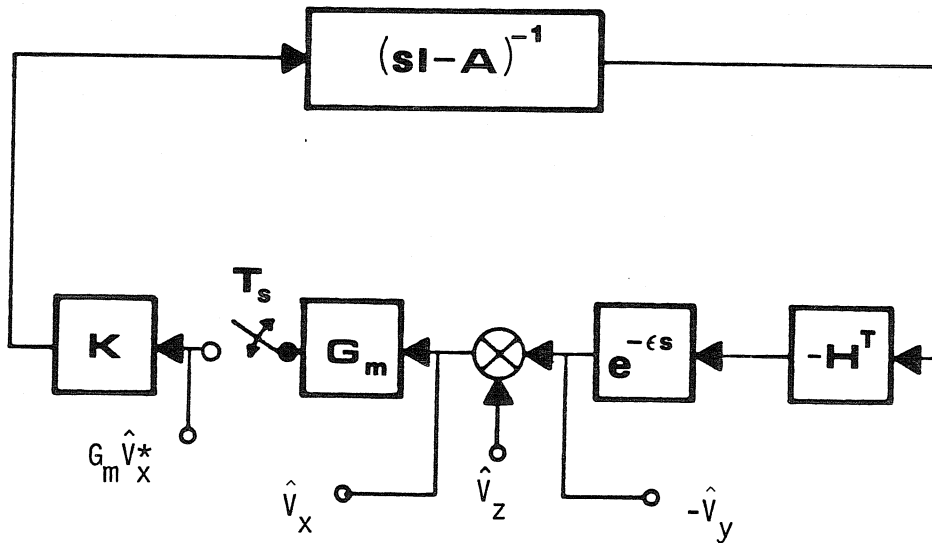
Figure 11.5. *Sampled-data block diagram for loop gain measurement with the feedback loop closed.*

Thus, if two additional samplers are introduced into the measurement pro-
cess, it is possible to measure $T_s^{\circ}(s)$ directly. However, these samplers add con-
siderable complexity to the experimental setup; therefore, this measurement
technique, while theoretically interesting, may not have a great deal of practical
value. A simpler, yet still useful, measurement is discussed in the next section.

11.5 Sampled-data analysis of loop gain measurement with feedback loop closed

Finally, the conventional closed-loop measurement is considered. Recall that
state-space averaging predicted essentially the same result for this case as for
the open-loop case. The sampled-data block diagram for this measurement is
shown in Fig. 11.5. The injected signal $\hat{v}_z$ consists of a pure sinusoid of fre-
quency ω_0, but, owing to the sampler, the other signals are both summations of
many sinusoids. The waveforms $\hat{v}_x$ and $\hat{v}_y$ are used as inputs to the network
analyzer, and a relation between the ω_0 components of these two signals is
sought.

The following relations are apparent from the block diagram.

$$\hat{V}_y(s) = H_e^T e^{-es}(sI - A)^{-1}K\,\hat{V}_z^{\circ}(s) \tag{11.10a}$$

$$\hat{V}_x(s) = \hat{V}_z(s) - \hat{V}_y(s) \tag{11.10b}$$

Unlike the open-loop measurement case discussed in Section 11.3, in the
present instance $\hat{v}_x(t)$ is not a pure sinusoid. Therefore, the equality between
$[\hat{v}_x]_{\omega_0}$ and $[\hat{v}_x^{\circ}]_{\omega_0}$ which was exploited in that earlier analysis does not hold here.
However, the injected signal $\hat{v}_z(t)$ is a pure sinusoid in this case, so equality
between $[\hat{v}_z]_{\omega_0}$ and $[\hat{v}_z^{\circ}]_{\omega_0}$ does exist.

$$[\widehat{v}_{z}^{\bullet}]_{\omega_0} = [\widehat{v}_z]_{\omega_0} \tag{11.11}$$

Thus, the aim should be to express the waveforms $\widehat{v}_x$ and $\widehat{v}_y$ in terms of $\widehat{v}_z$ and $\widehat{v}_z^{\bullet}$, a form from which the measurement prediction can be extracted.

If the two parts of Eq. (11.10) are sampled and then combined, the result is an equation for $\widehat{V}_x^{\bullet}(s)$ in terms of $\widehat{V}_z^{\bullet}(s)$.

$$\widehat{V}_y^{\bullet}(s) = H_{\delta}^T [e^{-\varepsilon s}(sI - A)^{-1}]^{\bullet} K \, \widehat{V}_x^{\bullet}(s) = T_s^{\bullet}(s) \widehat{V}_x^{\bullet}(s) \tag{11.12a}$$

$$\widehat{V}_x^{\bullet}(s) = \widehat{V}_z^{\bullet}(s) - \widehat{V}_y^{\bullet}(s) \tag{11.12b}$$

$$\widehat{V}_x^{\bullet}(s) = \frac{\widehat{V}_z^{\bullet}(s)}{1 + T_s^{\bullet}(s)} \tag{11.12c}$$

The substitution of this result in Eq. (11.10a) gives $\widehat{V}_y(s)$ in terms of $\widehat{V}_z^{\bullet}(s)$, one of the two desired equations.

$$\widehat{V}_y(s) = \frac{T(s)}{1 + T_s^{\bullet}(s)} \widehat{V}_z^{\bullet}(s) \tag{11.13}$$

The delay ε does not affect the numerator, which reduces to the state-space averaged loop gain when ε goes to zero. Then, the insertion of this last equation into Eq. (11.10b) gives $\widehat{V}_x(s)$ in terms of $\widehat{V}_z(s)$ and $\widehat{V}_z^{\bullet}(s)$, the other desired relation.

$$\widehat{V}_x(s) = \widehat{V}_z(s) - \frac{T(s)}{1 + T_s^{\bullet}(s)} \widehat{V}_z^{\bullet}(s) \tag{11.14}$$

Application of Eq. (11.11) to Eqs. (11.13) and (11.14) yields the ω_0 frequency

components of $\widehat{v}_x$ and $\widehat{v}_y$.

$$[\widehat{v}_x]_{\omega_0} = \frac{T(j\omega_0)}{1 + T_s^*(j\omega_0)} [\widehat{v}_z]_{\omega_0} \qquad (11.15a)$$

$$[\widehat{v}_y]_{\omega_0} = \frac{1 + T_s^*(j\omega_0) - T(j\omega_0)}{1 + T_s^*(j\omega_0)} [\widehat{v}_z]_{\omega_0} \qquad (11.15b)$$

The measurement prediction is the ratio of these two components.

$$\frac{[\widehat{v}_y]_{\omega_0}}{[\widehat{v}_x]_{\omega_0}} = \frac{T(j\omega_0)}{1 + T_s^*(j\omega_0) - T(j\omega_0)} \qquad (11.16a)$$

$$= T_c(j\omega_0) \qquad (11.16b)$$

This new quantity $T_c(s)$ is neither the state-space averaged nor the sampled-data loop gain discussed previously but rather a combination of the two. Hence, a question immediately arises concerning the utility of this closed-loop measurement: is it useful for stability analysis? Intuition suggests that it is, since the function $T_c(s)$ is, after all, the result of a closed-loop measurement. The question can be answered analytically by a comparison of the predictions of this new quantity with those of the now well-established sampled-data loop gain $T_s^*(s)$.

The actual closed-loop system poles s_p are determined from the sampled-data loop gain $T_s^*(s)$ by the usual relation.

$$1 + T_s^*(s_p) = 0 \qquad (11.17)$$

Consider the analogous equation for $T_c(s)$.

$$0 = 1 + T_c(s) \qquad\qquad\qquad (11.18\text{a})$$

$$= \frac{1 + T_s^{\bullet}(s)}{1 + T_s^{\bullet}(s) - T(s)} \qquad\qquad\qquad (11.18\text{b})$$

Thus, if $1+T_s^{\bullet}(s_p)=0$ and $T(s_p)$ is non-zero, then $1+T_c(s_p)=0$ also. Conversely, if $1+T_c(s_p)=0$ and both $T(s_p)$ and $T_s^{\bullet}(s_p)$ are finite, then $1+T_s^{\bullet}(s_p)=0$. Since the conditions on these assertions are very weak, it is seen that the closed-loop poles predicted by the new function $T_c(s)$ are almost always the same as those predicted by the sampled-data loop gain $T_s^{\bullet}(s)$. Thus, $T_c(s)$ can be considered to be a valid loop gain of the feedback system, and can be subjected to the standard analysis techniques, such as the Bode and Nyquist plots. The conclusion is that the closed-loop measurement is indeed, as intuition suggested, useful in stability analysis.

Finally, the qualitative relation between the loop gain $T(s)$ predicted by state-space averaging and the actual closed-loop gain $T_c(s)$ can be examined. Inspection of the expression for $T_c(s)$ in Eq. (11.16) shows that it consists of the state-space averaged result $T(s)$ divided by a quantity composed of one plus a correction term. The correction term consists of the difference between the sampled-data loop gain $T_s^{\bullet}(s)$ and the state-space averaged loop gain $T(s)$.

For frequencies far below one-half the switching frequency, it has been shown in Part I of this thesis that the sampled-data loop gain $T_s^{\bullet}(s)$ and the state-space averaged loop gain $T(s)$ are equal. Therefore, in this region the result of a closed-loop measurement cannot be distinguished from the state-space averaging prediction; the correction terms in the denominator of $T_c(s)$ cancel. Furthermore, if the system in question has a small bandwidth, both the sampled-data

and state-space averaged loop gains will be much smaller than unity in the frequency range where they do not agree. As a result, for these systems the closed-loop measurement will match the state-space averaged prediction even at high frequencies, since, at frequencies high enough for the two correction terms in the denominator of $T_c(s)$ to not cancel each other, they will be too small to be significant.

Thus, far below one-half the switching frequency, or even at high frequencies in low-bandwidth regulators, the closed-loop measurement $T_c(j\omega)$ matches the state-space averaged prediction $T(j\omega)$, confirming the usefulness of state-space averaging in these systems. It is only in high-bandwidth systems, for frequencies near one-half the switching frequency, that errors in the state-space averaged prediction will arise, since only then will the difference $T_s^*(j\omega) - T(j\omega)$ become significant compared to unity. Nevertheless, because the stability of a system depends on the behavior of its loop gain near the crossover frequency, and since, for a high-performance regulator, the crossover frequency occurs in the high-frequency regime, the variations of the actual closed-loop characteristic from the state-space averaged prediction are important. The ability to quantify them therefore provides a substantial advantage in the design of wide-bandwidth regulator systems.

11.6 Conclusions

This chapter developed sampled-data analysis predictions for various loop gain measurements of switching regulators. It was found that, if a loop gain is measured with the feedback loop open, the state-space averaged loop gain is obtained, exactly as predicted by state-space averaging. However, while accurate for regulators whose bandwidths are much less than one-half the switching

frequency, this result implies that the open-loop measurement is not useful for stability analysis when the bandwidth is a large fraction of one-half the switching frequency. It was then shown that the sampled-data loop gain, which provides an accurate stability criterion even at high frequencies, can be obtained by a closed-loop measurement of the sampled versions of appropriate signals. Finally, in the conventional method in which the feedback loop is closed but the measured signals are not sampled, a third quantity, a combination of the state-space averaged and sampled-data loop gains, was obtained.

Investigation of this new quantity demonstrated that it is, in fact, a valid loop gain, suitable for stability analysis. This new loop gain was then shown to match the state-space averaged loop gain in all cases except those involving regulators with large bandwidths, where the state-space averaged prediction develops significant errors at high frequencies. In these cases, the importance of the new closed-loop quantity for the analysis of wide-bandwidth systems was deduced from the fact that loop gain crossover for such systems occurs in precisely the same high-frequency range as that in which state-space averaging's predictions are inaccurate.

CHAPTER 12

EXPERIMENTAL ILLUSTRATION OF LOOP GAIN MEASUREMENTS

12.1 Introduction

The previous chapter has analyzed and interpreted several different tech-
niques for the measurement of quantities analogous to loop gains in switching
regulator systems. In this chapter, each of these measurements will be illus-
trated for a specific experimental circuit, and each measurement's agreement
with the appropriate prediction will be verified.

In Section 12.2 the experimental circuit to be used in this chapter is intro-
duced and discussed. The feedback arrangement is chosen so as to result in a
wide-bandwidth system, so that high-frequency effects are visible. The various
measurements are presented in Sections 12.3-12.5. As is the case throughout
this thesis, the emphasis is on the high-frequency characteristics of these meas-
urements; low-frequency behavior is generally ignored. It is seen that the meas-
urements match the predictions developed in Chapter 10 quite closely. In par-
ticular, the open-loop measurement is demonstrated to be an unreliable stabil-
ity criterion. Additionally, the measurements shown in these sections illustrate
how switching ripple on the fed-back waveform can modify the effective feedback
gains. Conclusions are contained in Section 12.6.

12.2 Experimental circuit

The measurements analyzed in the preceding chapter will be illustrated here
with use of the boost regulator shown in Fig. 12.1. The switching frequency is
48.5 kHz, and 12 W of power are delivered to the load. Notice that the sole fed-
back quantity in this system is the inductor current. The motivation for the
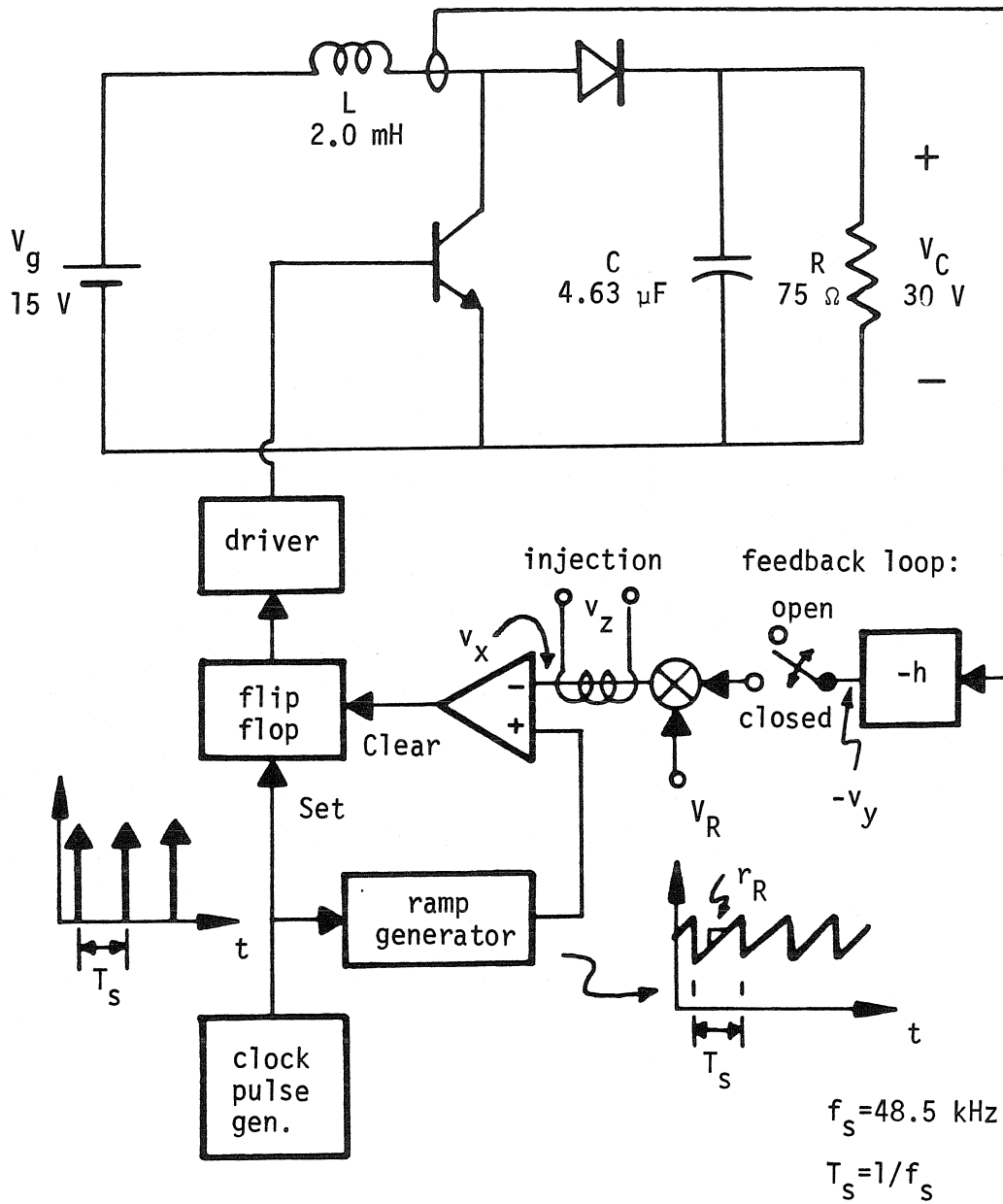
Figure 12.1. *Experimental boost regulator.*

choice of this somewhat unusual regulator is the desire to experiment with a high-bandwidth system. The usual quantity to be fed back is, of course, the output voltage. However, the state-space averaged transfer function from duty ratio to output voltage, which is a factor of the state-space averaged loop gain in such an arrangement, consists of two poles and a right-half-plane zero. The 90° phase lag from the right-half-plane zero means that any regulator constructed with only voltage feedback would be required to have an extremely low bandwidth to remain stable, just the opposite of what is wanted.

The transfer function from duty ratio to inductor current, on the other hand, has a left-half-plane zero to go along with the two poles, and all three of these features lie near 1 kHz. Thus, in the frequency range of 10-20 kHz, the state-space averaged transfer function is similar to that of a single integrator. This feedback arrangement, then, is precisely the kind of situation where the power of the sampled-data technique becomes evident, since, as was shown in Chapter 7 of Part I, state-space averaging predicts stability for any gain factor in this case. For a practical, wide-bandwidth voltage regulator, both inductor current and output voltage, and possibly the integral of the output voltage as well, would be fed back, but for the present investigation that arrangement would be too complicated.

With the inductor current chosen as the only fed-back quantity, the feedback gain of the system was set to a level which resulted in a wide-bandwidth but also comfortably stable system. Natural sampling was employed, the fed-back signal being compared directly to the artificial ramp. Therefore, it may be expected that switching ripple on the fed-back waveform will interact with the artificial ramp, altering the modulator gain in closed-loop cases. For loop gain measurements, the injection point used was the inverting input of the modulator com-

parator, an arrangement corresponding to the setup analyzed in the previous chapters.

In the following sections, each of the three measurements analyzed in the previous chapter will be illustrated. As is the case throughout this thesis, only the high-frequency ranges of the characteristics will be of concern. In this case, this philosophy means that derivations will be simplified at the expense of the loss of low-frequency details of the quantities under investigation. Thus, the loop gain predictions developed will not match the actual measurements at low frequencies but should be accurate in the vicinity of one-half the switching frequency.

12.3 Loop gain measurement with feedback loop open

With the feedback loop open, the analysis of the previous chapter predicts that the measured characteristic will be that of the state-space averaged loop gain $T(s)$. The expression for this function, first given in Chapter 4 as Eq. (4.11), is repeated as Eq. (12.1).

$$T(s) = H_e^T(sI - A)^{-1}K \qquad (12.1)$$

Here H_e is the effective feedback gain vector, A the averaged converter state matrix, and K the vector of coefficients of the duty ratio modulation input.

In the present case, an approximate form of this function can be obtained by a simple analysis very similar to that applied to the current-programmed regulator analyzed in Chapter 4 of Part I. Indeed, the experimental circuit of this chapter is, in fact, a current-programmed regulator with an artificial ramp. The approximation consists of the neglect of the low-frequency converter dynamics

by the replacement of the averaged state matrix A by zero. Since the region of interest is near one-half the switching frequency, this approximation should be acceptable. Then, as in the analysis of Chapter 4, the effective feedback gain vector H_e is obtained from analysis of the modulator waveforms and the circuit block diagram, and the relevant part of the forcing vector K is determined.

$$H_e = \begin{bmatrix} \dfrac{h}{\tau_R T_s} \\ 0 \end{bmatrix} \qquad (12.2a)$$

$$K = \begin{bmatrix} \tau_1 + \tau_2 \\ - \end{bmatrix} = \begin{bmatrix} V_C/L \\ - \end{bmatrix} \qquad (12.2b)$$

In the expression for the vector H_e, the symbol τ_R represents the rate of change of the artificial ramp in volts/second, and h is the feedback gain in volts/amp. The factor $1/(\tau_R T_s)$ can be recognized as the modulator gain G_m discussed in the previous chapter. Note that, because the feedback loop is open, there is no switching ripple to interact with the artificial ramp. In the expressions for the vector K, τ_1 and τ_2 are the magnitudes of the rates of change of the rising and falling current waveforms, respectively, in amps/second. In the boost converter the sum $\tau_1 + \tau_2$ is equal to the output voltage V_C divided by the inductance L.

With the completion of the calculation, the approximate loop gain is obtained.

$$T(s) = \frac{\dfrac{V_C}{\tau_R T_s} \dfrac{h}{L}}{s} = \frac{2\pi f_c}{s} \qquad (12.3a)$$

$$f_c = \frac{1}{2\pi} \frac{V_C h}{\tau_R T_s L} \qquad (12.3b)$$

The effect of the approximation used can be seen in the singularity of this expression at zero frequency. The exact state-space averaged loop gain, while resembling the approximation, Eq. (12.3), at high frequencies, levels off at low frequencies and in fact approaches a constant at dc. The differences between the two are exhibited in Fig. 12.2. Thus, as expected, the use of the approximate state-space averaged loop gain results in a loss of accuracy at low frequencies. However, this expression has the advantage of being simple and thus allows attention to be focussed on concepts rather than details. It will be seen that, even with this apparently gross approximation, excellent agreement can be obtained with experiment.

Experimentally, with the reference V_R set to maintain the proper steady-state operating point with the feedback loop open, the loop gain characteristic plotted in Fig. 12.3 was obtained. The characteristic at low frequencies is not shown, since agreement with the approximate theory in that region is not expected, and the upper frequency limit is one-half the switching frequency, since, in Part I, this frequency was shown to be the maximum possible system bandwidth. Logarithmic scales are used, as with conventional Bode plot analysis. Along with the experimental characteristic, also shown on this figure is the theoretical loop gain of Eq. (12.3), with the crossover frequency f_c chosen to fit the measured characteristic at high frequencies. As can be seen, the forms of the two characteristics in the vicinity of one-half the switching frequency are quite similar, the only difference being approximately 10° of additional phase lag, attributable to very high frequency dynamics somewhere in the loop. The crossover frequency f_c is close to 15 kHz.

Thus, with the feedback loop open, the high-frequency portion of the loop gain characteristic closely resembles the predicted single-pole expression of
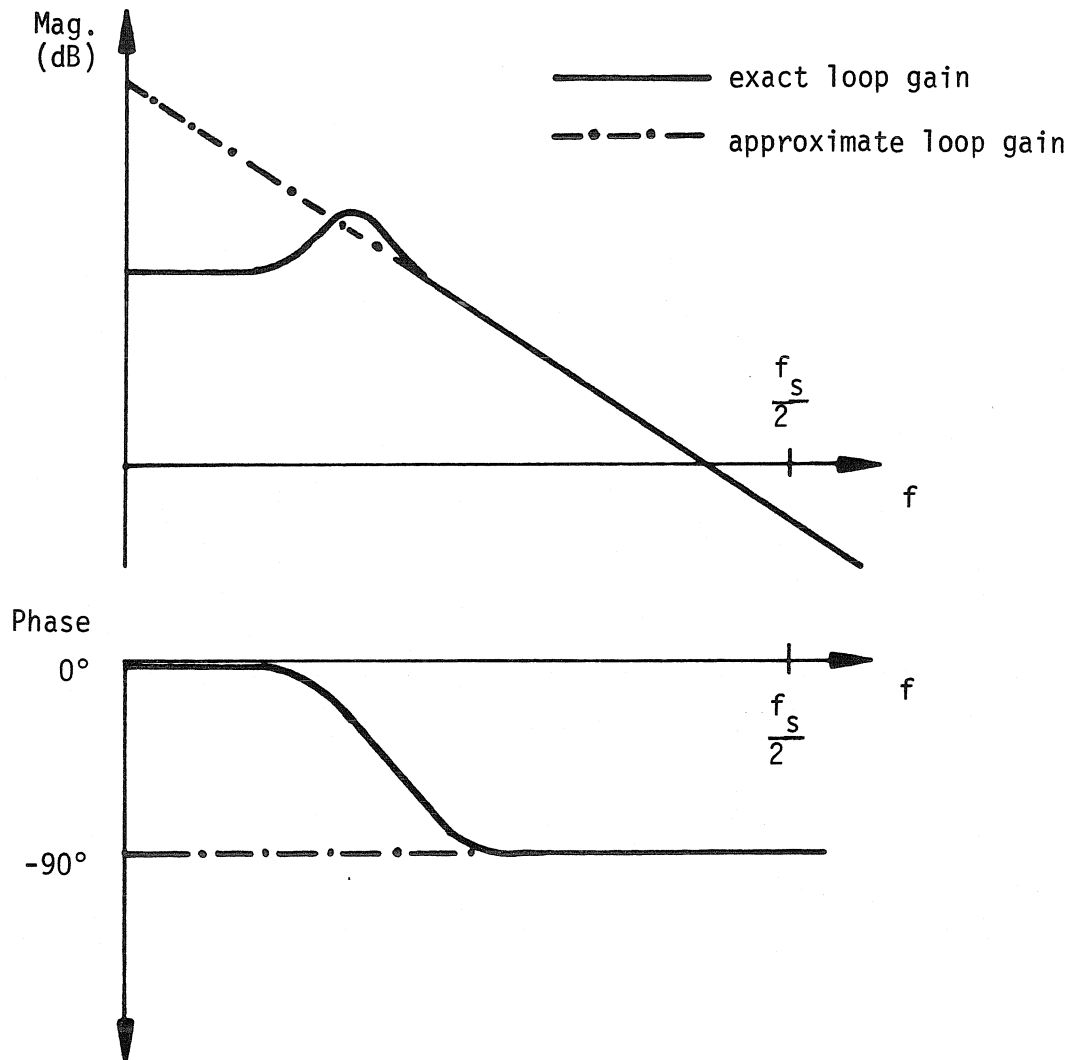
Figure 12.2. *Comparison of exact and approximate state-space averaged loop gains.*
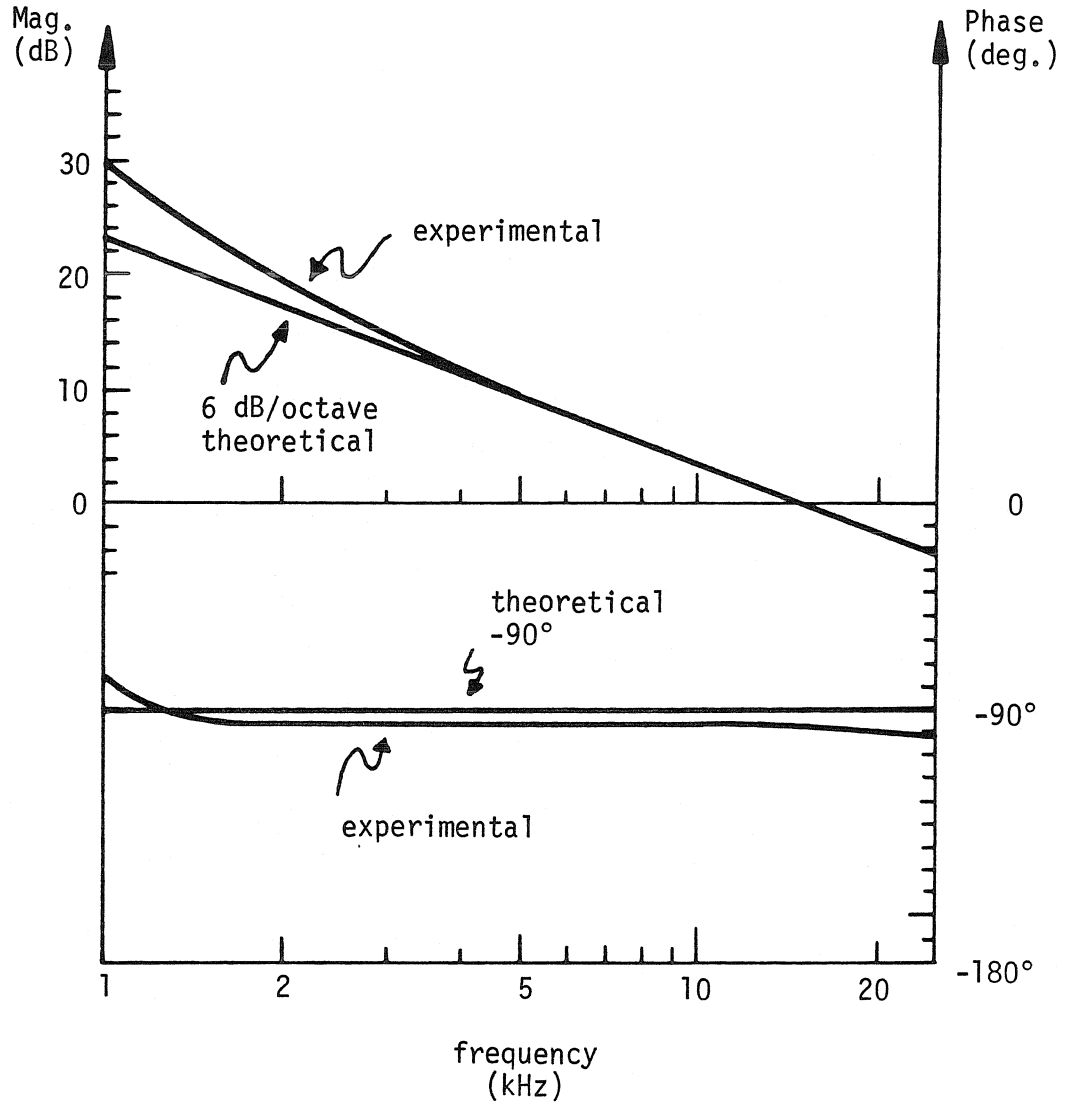
Figure 12.3. *Loop gain measurement with the feedback loop open.*

Eq. (12.3), provided the frequency f_c is chosen appropriately.

$$f_c = 15 \text{ kHz} \tag{12.4}$$

The next two sections of this chapter will investigate measurements made with the feedback loop closed. Quite different characteristics will be obtained, as predicted in the previous chapter. These predictions will incorporate the simple loop gain approximation $T(s)$ derived in this section, although the value of the crossover frequency f_c will have to be changed to match the experiments. This difference in the crossover frequency in the closed-loop cases is due to the presence of switching ripple at the modulator input, which, as has been discussed, can alter the modulator gain.

12.4 Loop gain measurement with feedback loop closed and signals sampled

From the analysis of Chapter 11, the result of a measurement of sampled signals with the feedback loop closed should be the sampled-data loop gain. An approximate form of this function can be obtained from the approximate state-space averaged loop gain, Eq. (12.3), by two modifications. The first is a change in the frequency f_c, because, with the loop closed, the switching ripple on the fed-back waveform will interact with the artificial ramp, changing the modulator gain from $1/(\tau_R T_s)$ to some new value $1/(\tau_e T_s)$. Here τ_e is an effective ramp slope. Second, the state-space averaged loop gain must be replaced by its sampled-data equivalent. The result is shown in Eq. (12.5).

$$T_s^*(s) = \frac{2\pi f_c' T_s}{e^{sT_s} - 1} \tag{12.5}$$

Here f_c' is the new crossover frequency for the state-space averaged loop gain. This new value takes into account the change in modulator gain when the feedback loop is closed. This frequency f_c' will be referred to as the equivalent crossover frequency, because, although the state-space averaged loop gain reaches unity magnitude at this frequency, the sampled-data loop gain may cross over at a different frequency. Note that, as was shown to be true in general in Section 7.4 of Part I of this thesis, this sampled-data loop gain, when considered as a function of real frequency, is periodic, with the switching frequency as period, and possesses a magnitude and an imaginary part which are even and odd, respectively, about one-half the switching frequency. However, the loop gain characteristic is only real at odd multiples of one-half the switching frequency; at even multiples there is a singularity in the function which invalidates the demonstration used to show that only real values occur at these frequencies.

The periodicity and symmetries of the sampled-data loop gain lead to the initially surprising conclusion that the low-frequency discrepancies between the approximate and actual state-space averaged loop gains will appear, in their sampled-data versions, at high frequencies as well. If the frequency range is restricted to a maximum of one-half the switching frequency, this effect will not appear, but near the switching frequency, the magnitude and phase behaviors occurring at low frequencies are repeated. This phenomenon will be seen in the measurement to be examined in this section.

To make the measurement, two samplers were constructed from analog switches and a monostable multivibrator. The one-shot was triggered by the system clock to provide, during each switching cycle, a synchronized narrow pulse to the control inputs of the analog switches. The output capacitance of

the switches was kept low so that the outputs from these devices were spikes, resembling delta functions. These pulse trains were then fed into the network analyzer.

Although this setup was somewhat noisy, measurements could be made. The resulting data are shown in Fig. 12.4. Unlike the other frequency plots in this chapter, a linear frequency scale, extending out to the switching frequency, is used to confirm the existence of the sampled-data loop gain symmetries. The solid curve is the approximate theoretical loop gain of Eq. (12.5), with the equivalent crossover frequency f_c' chosen to fit the experimental data point at one-half the switching frequency.

$$f_c' = 7.8 \text{ kHz} \tag{12.6}$$

Note that this value is only one-half that of the open-loop value f_c. The reason, as mentioned previously, is that the slope of the switching ripple on the fed-back waveform is nearly as large as the artificial ramp, but reversed in sign, so the effective ramp slope is increased by two. Whenever the fed-back ripple is significant compared to the artificial ramp, its effect must be taken into account in the loop gain analysis.

It is seen that, with this choice of the equivalent crossover frequency, agreement between the theoretical and experimental plots is quite good everywhere except at very low and very high frequencies, where discrepancies between the phase characteristics occur. At low frequencies the difference is readily ascribable to the approximation used in the choice of the theoretical loop gain, since loss of low-frequency accuracy was precisely the price expected for the simplicity of this expression. Moreover, as was explained earlier in this section, this
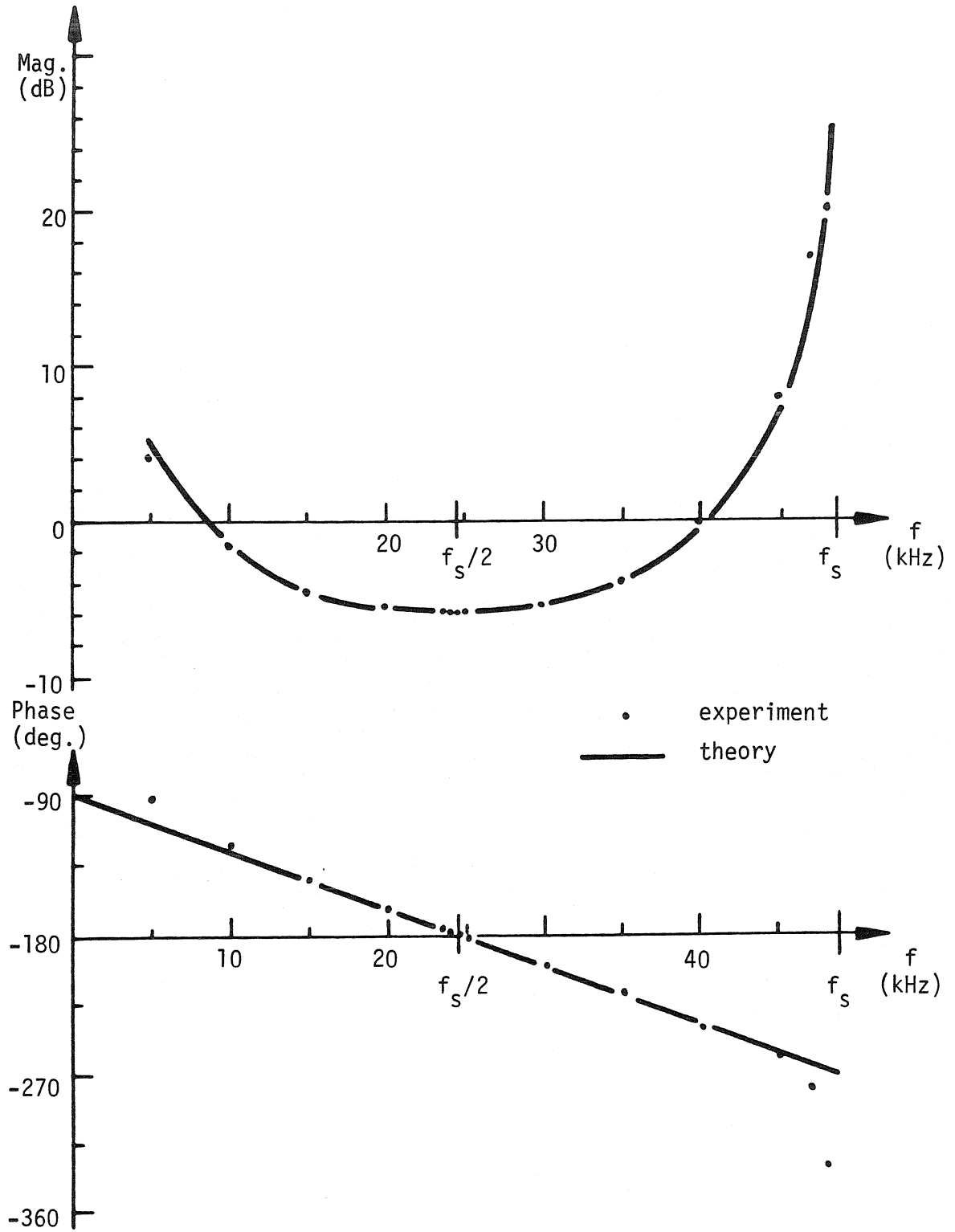
Figure 12.4. *Loop gain measurement with the feedback loop closed and signals sampled.*

approximation is also the root of the discrepancy near the switching frequency. The phase characteristic is odd about its value at one-half the switching frequency, so whatever happens at low frequencies happens again at high frequencies, only with opposite sign.

Indeed, a little thought shows that the experimental phase behavior near the switching frequency is quite reasonable. Note that the experimental phase data tend toward a value of -360° at the switching frequency, as required by the sampled-data loop gain's general properties, which were demonstrated earlier. The approximate theoretical phase plot, on the other hand, does not approach -360°; this peculiarity was explained previously to be a consequence of the fact that the theoretical expression possessed a singularity at the switching frequency which invalidated the demonstration of the reality property. Because the sampled-data loop gain is periodic, and because the state-space averaged and sampled-data loop gains match at low frequencies, the cause of the high-frequency singularity in the sampled-data loop gain is precisely the approximation which led to the dc singularity in the state-space averaged loop gain. The exact state-space averaged loop gain has no singularity at zero frequency, and consequently the exact sampled-data loop gain will also have no singularities at either dc or the switching frequency. Hence, the phase plot of this exact expression will approach -360°, just as the actual measurements do.

This qualitative argument is probably more revealing than a direct comparison of the measurement data with the exact theoretical loop gain. Over nearly the entire frequency range the simple theoretical approximation is seen to work extremely well. Furthermore, where differences do arise, they are easily explainable as a result of the approximation used, the measured characteristic's behavior agreeing with the inferred properties of the exact theoretical expres-

sion.

If attention is now returned to consideration of the loop gain characteristic as a whole, examination of the figure shows that the plotted loop gains, both theoretical and experimental, are purely real at one-half the switching frequency and display the expected symmetries about this frequency. The frequency range of this measurement is not wide enough to confirm the periodicity of the characteristic, and, in any case, the non-ideal samplers used would degrade the measurements at higher frequencies. However, the good agreement obtained with the prediction over the frequency range examined provides ample evidence of the theory's validity.

Finally, the dynamic information contained in this plot can be extracted. It is seen that the system is quite stable; the phase margin is nearly 60°. This result agrees with the analysis of Section 7.3 of Part I, where it was shown that, for this type of theoretical characteristic, the equivalent crossover frequency f_c' must be less than f_s/π, or 15.4 kHz in this case, for stability. Since the actual value of f_c' is only 7.8 kHz, one-half the critical value, the excellent phase margin is to be expected.

12.5 Loop gain measurement with feedback loop closed

The analysis in Chapter 11 indicated that, for this conventional closed-loop measurement, the measured loop gain would be something of a hybrid between the state-space averaged and sampled-data results.

$$T_c(s) \; = \; \frac{T(s)}{1 + T_s^{\bullet}(s) - T(s)} \qquad (12.7)$$

The actual measured characteristic is shown in Fig. 12.5. Also plotted on this
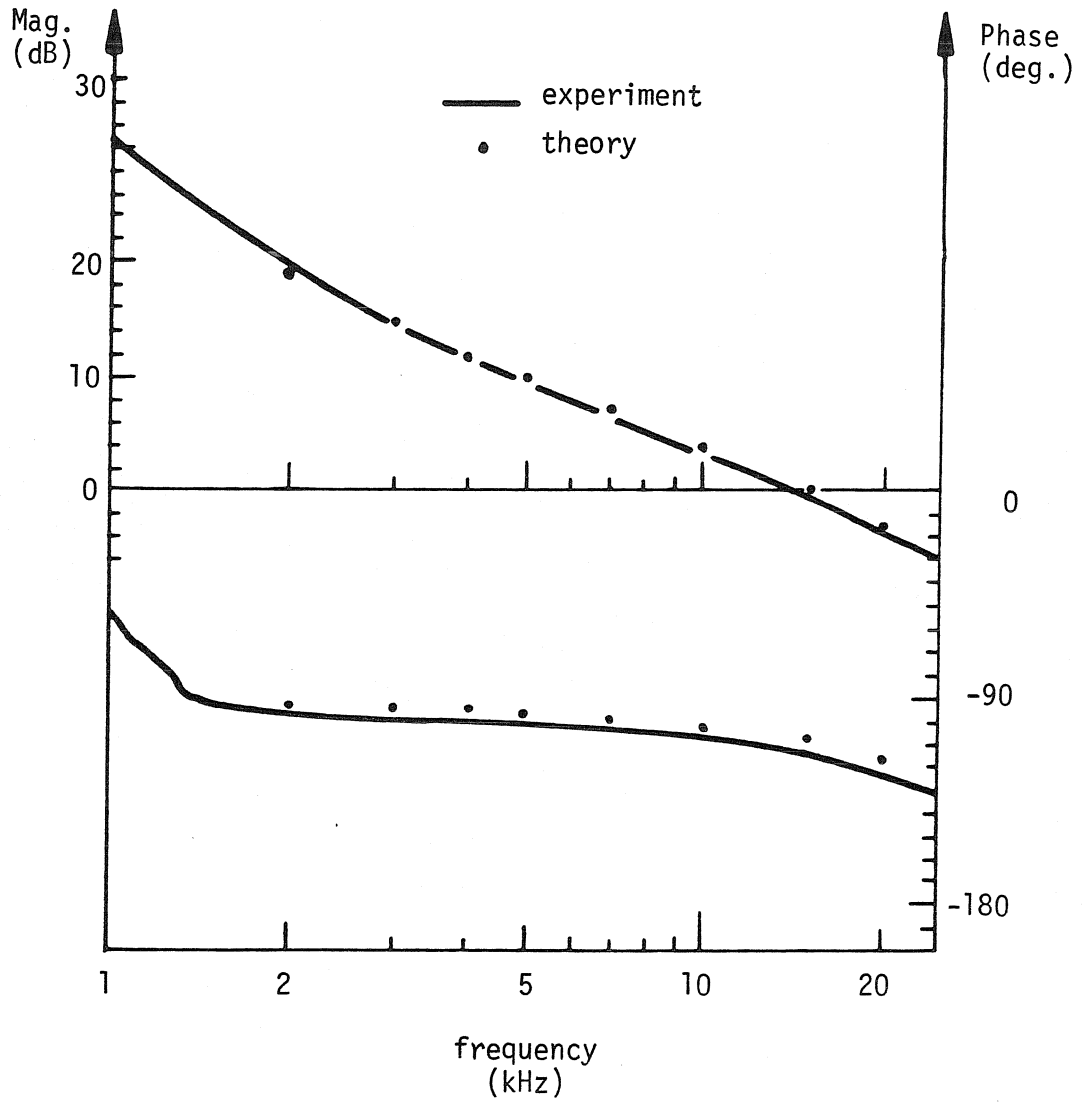
Figure 12.5. *Loop gain measurement with the feedback loop closed.*

figure are points of the theoretical prediction, calculated from Eq. (12.7). The state-space averaged loop gain $T(s)$ used in this calculation was the same simple single-pole function employed earlier, with its crossover frequency f_c' determined by the curve-fitting of the closed-loop, sampled-data measurement in the previous section.

$$T(s) \; = \; \frac{2\pi f_c'}{s} \tag{12.8a}$$

$$f_c' \; = \; 7.8 \text{ kHz} \tag{12.8b}$$

The agreement between theory and experiment is seen to be quite good, with the only discrepancy being an extra 10° of phase lag, attributable, as in the open-loop case, to some unmodeled high-frequency dynamics.

It is instructive to compare this measurement with the open-loop result of Fig. 12.3. The magnitude plots are nearly identical at high frequencies, but this feature is actually the result of two opposing influences. The first arises from the presence of switching ripple on the fed-back waveform in the closed-loop example, which reduces the gain of the closed-loop measurement in comparison with that of the open-loop case, as discussed earlier. The second, counteracting tendency is due to the correction term, $T_s^*(s) - T_s(s)$, in the denominator of Eq. (12.7); this term tends to raise the magnitude of the closed-loop gain relative to that of the open-loop characteristic. In the present case these two effects nearly cancel at high frequencies.

There are no such counteracting influences on the phase measurement. Like the sampled-data measurement, this measurement implies a stable system, but it also shows an additional 30° of phase lag over the open-loop case. Since it has

already been shown that the closed-loop measurement is an accurate predictor of stability while the open-loop measurement is not, this greater phase lag in the closed-loop case emphasizes that, for such a high-bandwidth system, a loop gain based on open-loop measurements is not a reliable guide to regulator performance because it is too optimistic in its predictions.

12.6 Conclusions

This chapter has presented experimental confirmation of the measurement analyses conducted in the previous chapter. A boost converter with current feedback was used to provide a test system with a state-space averaged loop gain resembling a simple integrator at high frequencies. Theoretical predictions incorporating this approximation could then be made, with the understanding that the resulting theory would not be accurate at low frequencies. A large feedback gain was used to obtain a wide-bandwidth system in which high-frequency effects would be noticeable. It was found that, with the feedback loop open, the state-space averaged prediction was obtained, as expected. The measured crossover frequency was approximately 15 kHz.

The feedback loop was then closed, and samplers were added to the signal paths fed to the network analyzer. Although this setup was noisy, measurements were successfully made, and the results matched the sampled-data loop gain very closely, provided the equivalent state-space averaged crossover frequency was reduced to 7.8 kHz from the open-loop value of 15 kHz. The reason for this reduction was determined to be the interaction of the switching ripple on the fed-back waveform with the artificial ramp, which in this case effectively halved the modulator gain, thereby reducing the total loop gain. The upper frequency limit of this measurement was chosen to be the switching frequency, in

order to illustrate the symmetries of the sampled-data loop gain. A discrepancy between the theoretical and experimental phase characteristics near the switching frequency was shown to be a result of the low-frequency inaccuracy of the approximate state-space averaged theoretical loop gain that was used. This approximate function possessed a singularity at dc which did not exist in the actual system, and which was propagated to the sampled-data theoretical loop gain in such a way as to cause the high-frequency discrepancy.

Finally, measurements were made with the feedback loop closed and with no sampling of the signals. The results agreed quite well with the theoretical prediction of Chapter 11, provided the state-space averaged equivalent crossover frequency found in the closed-loop, sampled measurement was employed. It was noticed that counteracting effects made the magnitude characteristic in this case appear quite similar to the open-loop characteristic. However, there was a large amount of excess phase lag in the closed-loop case relative to the open-loop measurement, demonstrating that the open-loop prediction is not a reliable indicator of stability.

CHAPTER 13

CONCLUSIONS

This part of this thesis has analyzed and illustrated various loop gain measurements of switching regulators. In Chapter 10 the usual injection technique employed to measure loop gains was reviewed, and the modifications necessary to apply the method to switching regulators were pointed out. It was also noted that switching regulators are not time-invariant systems, and that this characteristic can affect the measurements.

The state-space averaging method, which models switching regulators in a linear, time-invariant fashion, was then applied to the task of the prediction of loop gain measurements. The result was found to be the state-space averaged loop gain encountered in the theoretical discussion of Part I. An interesting feature of this analysis is that the form of the loop gain is the same even if the measurement is made with the feedback loop open, although a gain constants may change owing to interactions between the artificial ramp of the modulator and any switching ripple on the fed-back waveform. It was noted that, at high frequencies, the predictions of state-space averaging might prove inaccurate.

For this reason, in Chapter 11 the newly developed sampled-data method was used to analyze several measurement situations. With the feedback loop open, the prediction was determined to be the state-space averaged loop gain. Such a measurement was therefore seen to be a poor indicator of stability in wide-bandwidth systems, since in Part I it was shown that the state-space averaged loop gain is not accurate in these systems. Next, a case was considered in which the feedback loop is closed and the signals sent to the measuring instrument are sampled. In this situation, the measured gain was predicted to be the

sampled-data loop gain, which had been shown to be an excellent guide to stability. Finally, the closed-loop measurement with no sampling was treated. Here, it was found that, owing to the presence of the sampler in the model, the measurement corresponds to a function involving both the state-space averaged and sampled-data loop gains. It was also shown that the closed-loop poles predicted by this function are the same as those predicted by the sampled-data loop gain, implying that this closed-loop gain is an accurate stability indicator. This new closed-loop gain was shown to differ from the state-space averaged result only for wide-bandwidth systems, and even then only at frequencies approaching one-half the switching frequency. This frequency range is, however, precisely the region of loop gain crossover for these systems, and hence is of great importance.

In Chapter 12 a boost regulator with current feedback was used to test these three predictions. The feedback gain used was large so that the resulting system bandwidth would also be large, thus allowing the high-frequency differences between the various measurements to be observed. The use of current feedback made the state-space averaged loop gain appear at high frequencies to consist of a single pole, permitting the high-frequency prediction to be made with the use of this simple approximation. The open-loop measurement also resembled a single pole at high frequencies, as expected. The closed-loop, sampled measurement resulted in a characteristic which closely matched the theoretical sampled-data loop gain, although the equivalent crossover frequency of the state-space averaged loop gain used in the sampled-data calculation was required to be different from that of the open-loop case, owing to interactions between the artificial ramp and the switching ripple on the fed-back waveform. Finally, with the use of this same equivalent crossover frequency, the closed-

loop, continuous-signal measurement was shown to match the prediction for that case very closely. Although the magnitude characteristic of this measurement was similar to that of the open-loop case, some 30° of extra lag between the open and closed-loop phase characteristics emphasized the danger involved in any reliance upon open-loop measurements or state-space averaging in the design of wide-bandwidth switching regulators.

The good agreement between prediction and measurement in all cases demonstrates the accuracy of the sampled-data modeling technique. This new method is not only suitable for the analysis of regulator systems, as emphasized in Part I of this thesis, but is also useful for the interpretation of measurements made on these circuits. Thus, it has shown itself to be a powerful tool for the design of switching regulators.

PART III

ADAPTIVE CONTROL

OF SWITCHING REGULATORS

CHAPTER 14

INTRODUCTION

The first two parts of this thesis have developed a new technique, the sampled-data modeling method, for the accurate high-frequency analysis of switching converters and have used this model to interpret high-frequency measurements of loop gains of regulator systems. As performance requirements become more and more severe, regulator bandwidths will undoubtedly be forced into the neighborhood of one-half the switching frequency, the region where these new techniques become valuable. This third and final part of this thesis deals with a problem which may arise in such high-performance systems. This unexpected drawback is an acute sensitivity of a regulator's dynamic characteristics to changes in its operating condition, which includes the dc voltage and current levels in the converter, and external elements attached to the regulator.

Analysis, design, and measurement are all required to solve this problem. First, analysis is needed to determine when the sensitivity is bad enough to require attention. Then a design to alleviate the problem must be developed, and, finally, measurements are required to confirm the efficacy of the new design. In this case, the analysis involves manipulation of the expression for the regulator's loop gain, and the design changes feedback gains from constants to variables, specifically, functions which are proportional or inversely proportional to appropriate circuit quantities. The solution is therefore an application of adaptive control to switching regulators. The measurement technique used to verify the adaptive control's effectiveness is the observation of time-domain transient responses.

In Chapter 15 the development of the sensitivity analysis is undertaken. The discrete modeling technique proves to be most convenient for this purpose, in contrast to the previous part in which sampled-data modeling was used. Another change is that a modulator different from that employed before is introduced in order to eliminate a previously encountered complication, the interaction of the modulator's artificial ramp and the switching ripple of the fed-back waveform. The boost topology is used as an example throughout this part of this thesis. A simplified expression for the discrete loop gain of the boost regulator is given, and the manipulation of this loop gain to obtain sensitivity information is described.

Methods of adaptive control useful in the reduction of acute sensitivity are described in Chapter 16. For the boost regulator two schemes, differing in complexity and power, are suggested. It is found that both methods introduce extra feedback paths which alter the regulator's nominal dynamic properties. Modification of the original feedback network is required to compensate for these changes. Adaptive control strategies suitable for the other basic converter topologies are also discussed.

The actual implementation of an adaptively controlled boost regulator is described in Chapter 17. The performances of the two different adaptive schemes and a conventional, non-adaptive regulator are compared. It is seen that, while the conventional system's dynamic behavior degrades significantly under even small changes in operating point, the adaptive strategies preserve the regulator's dynamic characteristics over wide ranges of operating conditions. Finally, conclusions are presented in Chapter 18.

CHAPTER 15

SENSITIVITY OF SWITCHING REGULATORS

15.1 Introduction

The purpose of this chapter is to develop the machinery necessary for the explanation of the sensitivity of switching regulators to changes in their operating conditions and to derive explicit expressions for this sensitivity. In Section 15.2 the discrete modeling technique is chosen as being the most convenient analysis method for this investigation. In addition, uniformly sampling modulators, which will be used throughout this third part of this thesis, are introduced, and the discrete modeling of regulators incorporating this type of modulator is described.

The development of simplified loop gain expressions is undertaken in Section 15.3, using the boost regulator as an example. Invocation of the low switching ripple requirement drastically reduces the complexity of the loop gain expression, while maintaining reasonable accuracy. In Section 15.4, the qualitative and quantitative analysis of sensitivity is developed from this simplified loop gain. Again the boost converter serves as an example for which the detailed analysis is illustrated. Finally, conclusions are presented in Section 15.5.

15.2 Discrete modeling of regulators with uniformly sampling modulators

The previous two parts of this thesis have emphasized the sampled-data modeling technique as being a natural and accurate method for the analysis of switching regulators. However, in the comparison between the sampled-data and discrete modeling techniques in Chapter 7, it was pointed out that the loop gains of these two models were equivalent representations of a regulator's

behavior, so that other factors could determine which method to use in a given situation. For example, in Part II of this thesis the analysis of loop gain measurements in the frequency domain was the goal, and the continuous nature of the sampled-data method made it a natural choice for that application.

In this present investigation, on the other hand, a topic of interest will be the movement of system poles under various influences. An infinite number of such poles s_p exist in a sampled-data analysis, but only a finite number of closed-loop poles z_p result from the discrete analysis, the two sets being related by the equation $z_p = e^{s_p T_s}$, which was derived earlier. Therefore, the discrete method will be used for the analysis in this part of this thesis, in order to avoid the complexity of a description of the movement of infinitely many system poles.

In addition, a second change will be made in the foundations of Part III of this thesis compared to those of previous parts. Thus far, all of the modulators discussed have been of the naturally sampling type, in which the fed-back waveform is compared directly to the artificial ramp, with the duty ratio being determined by the point of intersection of these two signals. It has been noted several times that the switching ripple on the fed-back waveform can modify the effective gain of such a modulator.

In order to eliminate this potential interaction, which would complicate the analysis in future chapters, uniformly sampling modulators are utilized in this present investigation. Such a modulator, illustrated in Fig. 15.1, operates by sampling the fed-back signal $\hat{v}_1$ at one point in each switching cycle and using this value to determine the duty ratio via the usual comparison with an artificial ramp. Thus, the waveform $\hat{v}_2$ compared with the artificial ramp has no switching ripple, and the modulator gain G_m is a constant, depending only on the slope r_R of the ramp and the switching period T_s.
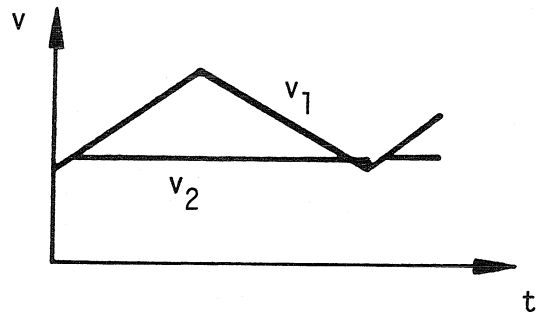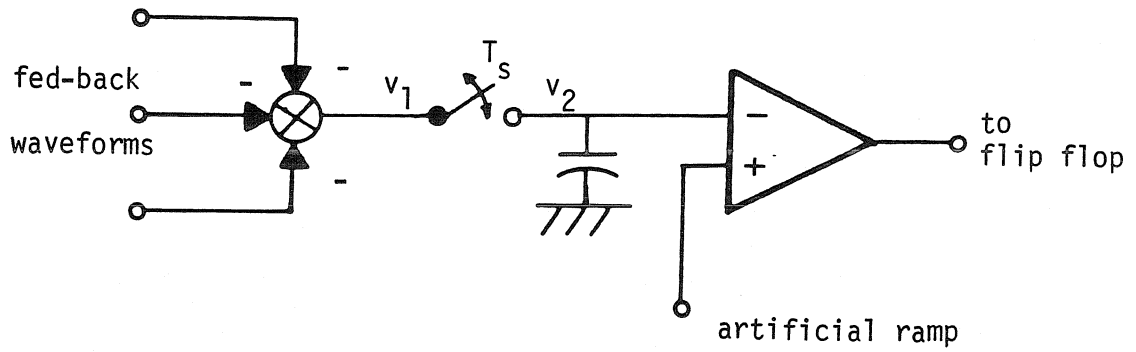
Figure 15.1. *Uniformly sampling modulator.*

$$\hat{d}_n = \frac{\hat{v}_1(nT_s)}{r_R T_s}$$

(15.1)

As implied by the figure and the equation, the uniformly sampling modulators used in this treatment will take their samples at the beginning of each switching period.

The discrete analysis of switching regulators employing this sort of modulator is most favorably conducted in a slightly different manner from that used in Chapter 5 of Part I. The change is due to the fact that the discrete model predicts the value of the state at only one instant in each switching cycle. It was pointed out in Chapter 5 that the discrete modeling procedure could be simplified if the state values yielded by the model were precisely those processed by the controller to determine the duty ratio. For a naturally sampling system, the type considered in Chapter 5, these state values were those at the switching times $(n+D)T_s$, $n = \ldots -1, 0, 1, \ldots$, when the converter transistor switch is turned off, and the model was developed accordingly.

For regulators employing the uniformly sampling modulators considered here, however, the control law is determined by the values of the state vector at the beginning of each switching cycle, not at the transition during the cycle.

$$\hat{d}_n = -H_e^T \hat{x}[nT_s]$$

(15.2)

Therefore, it is profitable to recast the converter model to give the values of the state at times nT_s rather than at times $(n+D)T_s$. As in Chapter 5 the fundamental small-signal equation, Eq. (3.15), is integrated over a switching cycle, but the starting point of the present integration is chosen to be time nT_s, instead of $(n+D)T_s$ as in Chapter 5. Because the development is so similar to that of the

previous case, only the result is stated here.

$$\hat{x}[(n+1)T_s] = e^{A_2 D'T_s} e^{A_1 DT_s} \hat{x}[nT_s] + e^{A_2 D'T_s} KT_s \hat{d}_n \qquad (15.3a)$$

$$K = (A_1 - A_2)\overline{x}[(n+D)T_s] + (b_1 - b_2)V_g \qquad (15.3b)$$

A comparison of this equation with the previous result, Eq. (5.6), shows that the only differences between the two expressions are the reversal of the exponential matrices in the first term on the right and the disappearance of the matrix $e^{A_1 DT_s}$ as a coefficient of the vector K in the uniformly sampling version.

In further imitation of the procedure followed in Chapter 5, the z-transforms of the control law, Eq. (15.2), and the converter model, Eq. (15.3), are taken. The result of the combination of these expressions is a formula for the duty ratio modulation, from which a loop gain $T_z(z)$ can be defined.

$$T_z(z) = H_e^T(zI - e^{A_2 D'T_s} e^{A_1 DT_s})^{-1} e^{A_2 D'T_s} KT_s \qquad (15.4)$$

This loop gain is actually quite similar to that developed in Chapter 5 for modulators employing natural sampling. When the straight-line approximation is used to evaluate the exponential matrices, the matrix expression within the inverse operation matches exactly the corresponding term found in Chapter 5. The remaining factors outside the inverse, while different in the two cases, often vary only in second-order terms.

15.3 Approximate loop gains for switching regulators with uniformly sampling modulators

Application of the straight-line approximation to the expression for the regu-

lator loop gain, Eq. (15.4), results in explicit loop gain expressions for various
systems. As an example, one which will be used throughout this part of this
thesis, consider the boost regulator of Fig. 15.2, in which the integral v_i of the
output voltage error is fed back in addition to the inductor current i_L and out-
put voltage v_C, so that the dc value of the output voltage is held constant. The
resultant system has three states. With the help of the straight-line approxima-
tion, the loop gain of this system can be calculated.

$$T_z(z) = \frac{T_s}{V_M} \frac{g_1 P_1(z) + g_2 P_2(z) + g_3 P_3(z)}{(z - z_1)(z - z_2)(z - z_3)} \tag{15.5a}$$

$$P_1(z) = \frac{\overline{v_C^s}}{L}(z-1)\left[z\left(1+\frac{D'T_s}{\tau C}\right) - \left(1 - \frac{T_s}{RC} - \frac{D'T_s}{\tau C}\frac{DT_s}{RC} + \frac{(D'T_s)^2}{LC}\right)\right] \tag{15.5b}$$

$$P_2(z) = \frac{\overline{i_L^s}}{C}(z-1)\left[-z\left(1-\frac{D'T_s}{RC}-\frac{D'T_s}{L/\tau}\right)+\left(1-\frac{D'T_s}{RC}+\frac{(D'T_s)^2}{LC}\right)\right] \tag{15.5c}$$

$$P_3(z) = T_s\frac{\overline{i_L^s}}{C}\left[-D'z^2+\left(D'-D+\frac{D'T_s}{L/\tau}\right)z+D\left(1+\frac{(D'T_s)^2}{LC}\right)\right] \tag{15.5d}$$

$$z_{1,2} = \left(1-\frac{T_s}{2RC}\right)\pm jT_s\left[\frac{D'^2}{LC}-\left(\frac{1}{2RC}\right)^2\right]^{1/2} \tag{15.5e}$$

$$\overline{i_L^s} = \overline{i_L}[(n+D)T_s] \quad , \quad \overline{v_C^s} = \overline{v_C}[(n+D)T_s] \tag{15.5f}$$

$$r = \overline{v_C^s}/\overline{i_L^s} \tag{15.5g}$$

This expression, while useful for accurate designs, is quite complicated and
hence is difficult to interpret. The analogous expressions for the other basic
converter topologies are equally complex. Fortunately, the fundamental design
requirement, first discussed in Chapter 2, of low switching ripple on the con-
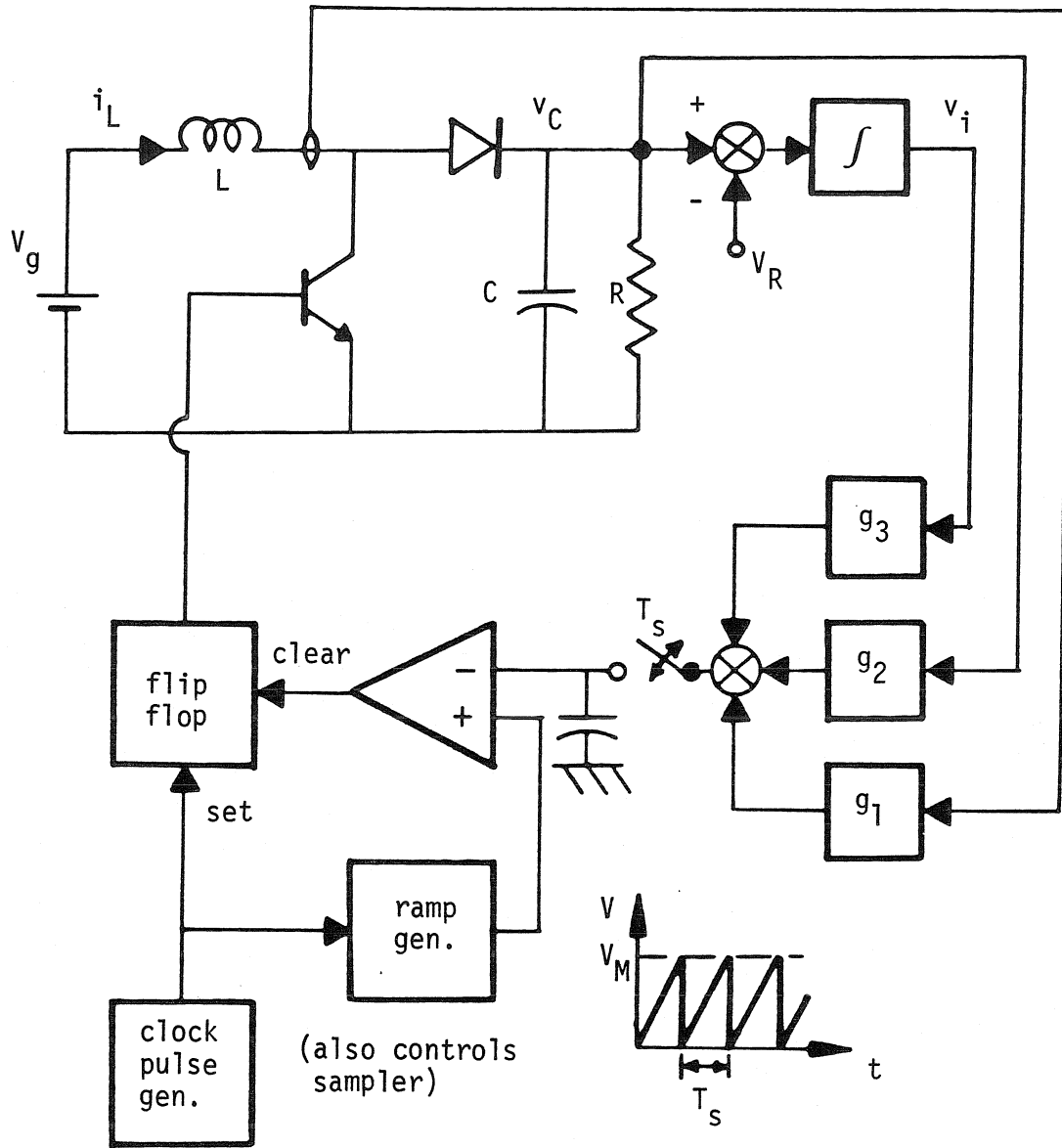
Figure 15.2. *Boost regulator, employing integral state feedback and uniformly sampling modulator.*

verter states allows considerable simplification to be accomplished. One conse-
quence of this requirement is that the switching period must be much less than
the natural time constants of the converter, and therefore many of the terms in
the loop gain can be neglected. One particular result of this simplification is
that the open-loop poles z_1 and z_2, originally close to $z=1$ in the z-plane, are
now positioned exactly on that point. A second, more direct consequence of low
switching ripple is that the steady-state values of state components at the
switching times $(n+D)T_s$ can be replaced by their average values. As was shown
in Chapter 3, these average values are quite easy to calculate.

With these approximations, the expression for the loop gain, Eq. (15.5),
appears much less formidable.

$$
T_z(z) \approx \frac{T_s}{V_M}\left\{ \frac{g_1 V_C}{L}\frac{1}{z-1} - \frac{g_2 I_L}{C}\frac{1}{z-1} \right.
$$

$$
\left. + \frac{g_3 T_s I_L}{C}\frac{-D'z^2 + (D'-D+\frac{D'T_s}{L}\frac{V_C}{I_L})z + D}{(z-1)^3} \right\} \tag{15.6}
$$

Similar simplifications of the expressions for the loop gains of regulators
employing the other basic converters can also be performed. The results of
these manipulations will be presented in the following chapter, where they will
be of immediate use in the determination of design procedures.

15.4 Sensitivity analysis

The approximate loop gain just developed permits an analysis of the effects of
changes in the converter's steady-state operating condition on the dynamic
behavior of the regulator to be undertaken. That such changes occur can be
seen from an inspection of the general form of the loop gain, repeated here as

Eq. (15.7).

$$T_z(z) = H_s^T(zI - e^{A_2 D'T_s}e^{A_1 D'T_s})^{-1}e^{A_2 D'T_s}KT_s \qquad (15.7a)$$

$$K = (A_1 - A_2)\bar{x}[(n+D)T_s] + (b_1 - b_2)V_g \qquad (15.7b)$$

The vector K depends, in general, on the steady-state values of the converter state components and input voltage V_g. When these quantities change, owing to, for example, an increase in input voltage, the vector K changes also. This variation in turn leads to a change in the regulator loop gain, affecting the closed-loop pole locations and hence the dynamic characteristics of the system.

For this present treatment, changes in three circuit quantities, the load resistance R, input voltage V_g, and output capacitance C, will be considered. These variations mirror the principal types of changes seen in a regulator's external environment. The boost regulator will again serve as an example; similar analyses can, of course, be carried out for the other converter topologies. First, the effects of these three changes on the regulator's loop gain will be discussed. The insight obtained from this qualitative treatment will then allow the development of a formula which predicts, approximately, the movement of the closed-loop system poles in response to these changes.

One effect of a change in the load resistance R is, of course, a change in the value of R used in the loop gain. This change is not the most important one, however. A change in the regulator load implies a change in output current, and consequently the steady-state inductor current will also change. On the other hand, the input voltage is assumed constant, and the regulator should, after a transient interval, maintain the output voltage at the same level as before the load change. It is easily determined that the relationship between the two

voltages depends solely on the duty ratio for an ideal, lossless converter.

$$\frac{V_C}{V_g} = \frac{1}{1 - D} \qquad (15.8)$$

Hence, the steady state duty ratio is not affected to first order, by a load change.

If the variation is not in the load, but in the input voltage V_g, a change in the steady-state inductor current again occurs, a fact which is easily seen from a consideration of the power flow in the theoretically 100% efficient regulator. Changes in V_g do not affect the output voltage or the load, so the output power remains constant. To maintain the input power at the same constant level, the input current, which is just the inductor current in the boost converter, must fall as the input voltage V_g rises, and vice versa. In addition, since the regulator maintains the output voltage constant, Eq. (15.8) implies that the duty ratio must change if the input voltage changes.

Finally, the effects of a change in output capacitance can be examined. Since the capacitor is an open circuit in dc analysis, the average converter waveforms and duty ratio are not changed, by a variation in output capacitance, assuming, of course, that the regulator remains stable after the change. The only effect on the loop gain and, hence, on the regulator dynamics, is that arising from the change in the value C.

Variations in quantities other than these three could also be examined, but such changes do not occur in practical regulator systems. For example, a change of the inductance in a boost regulator will have some effect on the loop gain, but this quantity is extremely unlikely to vary in a working system. In contrast, a change in output capacitance will occur whenever a load with significant capacitance is attached to the regulator output.

This discussion has served to indicate how variations in certain quantities affect the steady-state operation of a boost regulator, and hence its loop gain. However, the important question of the degree of change, and the resulting effect on the closed-loop system poles, has not yet been addresed. This topic can be discussed with the help of the approximate loop gain formulated in the previous section. The boost regulator's approximate loop gain, Eq. (15.6), is repeated here, for easy reference, as Eq. (15.9).

$$T_z(z) \approx \frac{T_s}{V_M} \left\{ \frac{g_1 V_C}{L} \frac{1}{z-1} + \frac{I_L}{C} \left[-\frac{g_2}{z-1} \right. \right.$$

$$\left. \left. + \frac{g_3 T_s}{(z-1)^3} \left(-D'z^2 + \left(D' - D + \frac{D'T_s}{L} \frac{V_C}{I_L} \right) z + D \right) \right] \right\} \qquad (15.9)$$

The notation is as in Fig. 15.2. This expression, although a simplified form of the original equation, is still rather complicated. Several of its components, however, including the average output voltage V_C, the inductance L, the switching period T_s, and the artificial ramp height V_M, are easily identified as constants. The only potentially variable quantities are the average inductor current I_L, the capacitance C, and duty ratio D. In fact, the quantity I_L/C appears prominently as a factor of the last two terms of this expression. An approximate relation describing how changes in this quantity affect the system poles can be developed by the treatment of this quantity I_L/C as the only variable, with everything else held constant. Some errors are introduced by this procedure, but the loss of accuracy is outweighed by the simplicity and usefulness of the resulting expression.

The development of this relation begins by the separation of the quantity I_L/C into a nominal value plus a fractional change δ.

$$\frac{I_L}{C} = (1 + \delta)\left(\frac{I_L}{C}\right)_n \qquad (15.10)$$

Here $(I_L/C)_n$ is the value of I_L/C under nominal circuit operating conditions, that is, those conditions assumed during the design of the system. Before this expression is substituted into the loop gain, it is useful to write an expression which connects the nominal loop gain $(T_z(z))_n$ to the nominal closed-loop poles p_1, p_2, and p_3.

$$1 + (T_z(z))_n = \frac{(z - p_1)(z - p_2)(z - p_3)}{(z - 1)^3} \qquad (15.11)$$

This equation is easy to verify. The zeros of the expression $1+(T_z(z))_n$ are the nominal closed-loop poles p_1, p_2, and p_3, and the denominator of $(T_z(z))_n$ and hence $1+(T_z(z))_n$ is approximately $(z - 1)^3$. The only remaining possibility for this expression is an overall multiplicative constant, and this factor must be unity, because the order of the polynomial in the numerator $T_z(z)$ is less than that of the polynomial $(z-1)^3$ in its denominator.

Insertion of the rewritten form of the quantity I_L/C, Eq. (15.10), into the loop gain expression, Eq. (15.9), and extraction of the nominal part $(T_z(z))_n$ yields an expression which shows how the fractional variation δ in I_L/C affects the loop gain.

$$T_z(z) = (T_z(z))_n + \delta\frac{T_s}{V_M}\left(\frac{I_L}{C}\right)_n\left[-\frac{g_2}{z-1}\right.$$

$$\left. + \frac{g_3 T_s}{(z-1)^3}\left(-D'z^2 + \left(D' - D + \frac{D'T_s}{L}\frac{V_C}{I_L}\right)z + D\right)\right] \qquad (15.12)$$

Substitution of this expression in the equation which defines the actual closed-loop poles in the presence of the perturbation, $1+T_z(z)=0$, and a further substitution for the nominal loop gain $(T_z(z))_n$ from Eq. (15.11) results in an equation whose roots are the closed-loop poles in the presence of the perturbation and which depends on the perturbation δ and various parameters of the system under nominal operating conditions.

$$(z-p_1)(z-p_2)(z-p_3) = -\delta \frac{T_s}{V_M} \left(\frac{I_L}{C} \right)_n \left[-g_2(z-1)^2 + g_3 T_s \left(-D'z^2 \right. \right.$$

$$\left. \left. + \left(D' - D + \frac{D'T_s}{L} \frac{V_C}{I_L} \right) z + D \right) \right] \qquad (15.13)$$

As a simple check of this equation, note that if $\delta=0$, the case of no variation in the operating condition, the roots are just p_1, p_2, p_3, the nominal system poles. Recall also that this equation is approximate, since it does not account for changes in duty ratio, nor for variations in the quantity I_L appearing within the integral feedback term. Indeed, even the origin of this equation was only an approximate form of the loop gain. In many cases, however, the effects of these errors will be small, and, in any case, this relation is valuable for its ability to compare the sensitivities of different designs. The sensitivity is estimated by the assumption of a small fractional change in the quantity I_L/C, that is, $\delta \ll 1$, and the calculation of the resultant small change ε in the location of a pole.

For convenience, take p_1 to be the pole in question. Under the influence of the variation δ, this pole will move to a location $p_1+\varepsilon$, with $|\varepsilon| \ll |p_1|$. Suppose further that all three poles p_1, p_2, and p_3 are distinct. Then, because ε is small, $p_1+\varepsilon-p_2 \approx p_1-p_2$, and similarly for p_3, so ε may be found directly.

$$\varepsilon \approx -\delta \frac{\frac{T_s}{V_M}\left(\frac{I_L}{C}\right)n}{(p_1-p_2)(p_1-p_3)}\left[-g_2(p_1-1)^2\right.$$

$$\left. + g_3\left(-D'p_1^2 + \left(D'-D+\frac{D'T_s}{L}\frac{V_C}{I_L}\right)p_1 + D\right)\right] \tag{15.14}$$

The formula for the case of repeated poles is somewhat different from this expression, but is also easily found from Eq. (15.13).

An important feature of this expression is that the sensitivity increases with feedback gain. That is, for a given δ, higher gains g_2 and g_3 result in larger magnitudes of ε. If a system requiring such large feedback gains, in order to meet transient response specifications, must also work under wide ranges of input voltage and loading, the high sensitivity of the system may actually force the circuit into instability under certain operating conditions.

15.5 Conclusions

This chapter has investigated the sensitivity of switching regulators to changes in their operating conditions with the use of a boost regulator as an example. The discrete modeling technique was chosen for the analysis, owing to the finite number of closed-loop poles its model possesses. Uniformly sampling modulators were introduced as a means for the elimination of the dependence of the modulator gain on the switching ripple of the fed-back waveform, and the discrete model of systems employing such modulators was developed. With the boost converter serving as an example, the loop gain of such a system was exhibited, and it was shown that the requirement of low switching ripple on converter states can be used to simplify such loop gain expressions considerably.

With use of this simplified expression for the boost regulator's loop gain, the effects of changes in load resistance, input voltage, and output capacitance on the system's loop gain, and therefore on its dynamic behavior, were examined. It was seen that many of these effects are due to the appearance in the loop gain expression of a quantity consisting of the ratio of steady-state inductor current to output capacitance. From this fact an equation relating approximate closed-loop pole movement to changes in operating condition was developed, enabling quantitative estimates of stability to be made. It was seen that the sensitivity increases as the feedback gains used become larger, a characteristic which raises the possibility of excessive degradation of the dynamic behavior of high-performance regulators as operating conditions vary from their nominal values.

CHAPTER 16

APPLICATION OF ADAPTIVE CONTROL TO SWITCHING REGULATORS

16.1 Introduction

The preceding chapter has shown that a high-performance switching regula-
tor may display excessive sensitivity to changes in the operating condition of the
system's power converter. In this chapter, it will be shown that the application
of adaptive control to the regulator's feedback network can substantially reduce
this unwanted sensitivity. In Section 16.2 the boost regulator again serves as an
example in a demonstration that the appropriate use of adaptive control is
beneficial to the regulator's dynamic properties. Two adaptive schemes are
developed, offering different levels of performance, but also involving different
levels of complexity. An undesirable by-product of this use of adaptive control is
discussed in Section 16.3. There it is found that the adaptive portion of the
feedback network introduces a new feedback path, altering the effective feed-
back gain of one state component. Analysis of the situation indicates the neces-
sary compensation to correct the problem.

After this detailed treatment of the boost regulator, in Section 16.4 adaptive
possibilities for the other basic converter topologies, the buck, buck-boost, and
Ćuk converters, are examined. For each case a simplified loop gain expression
is given and various appropriate adaptive strategies are presented. Conclusions
are contained in Section 16.5.

16.2 Adaptive control of a boost regulator

The discussion in the previous chapter concerning the sensitivity of the boost
regulator, coupled with the existence of similar phenomena in the other basic

converter topologies, suggests that severe difficulties may be encountered in the design of a high-performance, high-gain switching regulator. In this present section, means for the alleviation of this problem will be sought, again with the use of the boost topology as an example. Two criteria will be used in this search. One requirement is, of course, that the remedy be effective in reducing excessive sensitivity. The second guide, as important as the first, is that any proposed technique be relatively simple, so that its implementation does not add substantially to the cost of a practical system.

The key to the conception of such a remedy for a boost regulator lies in the form of its approximate loop gain $T_z(z)$ in Eq. (15.9), repeated here as Eq. (16.1).

$$T_z(z) \approx \frac{T_s}{V_M} \left\{ \frac{g_1 V_C}{L} \frac{1}{z-1} + \frac{I_L}{C} \left[-\frac{g_2}{z-1} \right. \right.$$

$$\left. \left. + \frac{g_3 T_s}{(z-1)^3} \left(-D' z^2 + \left(D' - D + \frac{D' T_s}{L} \frac{V_C}{I_L} \right) z + D \right) \right] \right\} \tag{16.1}$$

Recall that, in the computation of the effects of sensitivity, variations in the quantity I_L/C, the ratio of the average inductor current to the output capacitance, were considered. Inspection of the loop gain in Eq. (16.1) shows that this quantity appears as a factor multiplying the two feedback gains g_2 and g_3. This observation suggests that the variations in the quantity I_L/C could be mitigated if the gains g_2 and g_3 were made inversely proportional to that quantity, since then the loop gain would be nearly invariant under variations affecting the quantity I_L/C. Two applications of this idea are discussed in the following paragraphs. One is relatively simple and provides protection against inductor current changes, while the other, at the expense of greater complexity, acts to

neutralize changes in both inductor current and output capacitance.

In the first technique, which protects solely against inductor current changes, the idea is to measure the inductor current i_L and to make the gains g_2 and g_3 inversely proportional to that current. A block diagram of this concept is shown in Fig. 16.1. In this figure, the fed-back variables are as in the diagram of the boost regulator in Fig. 15.2. The block labelled "i_{Ln}/i_L" serves as a nonlinear amplifier, with its gain set by the value of the inductor current i_L. The constant i_{Ln} is the value of the inductor current when the circuit operating condition is that for which the nominal feedback gains were calculated, g_{2n} and g_{3n} being two of those nominal gains. The result is that the effective values of the feedback gains g_2 and g_3 vary in the desired manner and therefore keep the quantities $g_2 i_L$ and $g_3 i_L$ constant.

$$g_2 = g_{2n}\frac{i_{Ln}}{i_L} \qquad\qquad (16.2a)$$

$$g_3 = g_{3n}\frac{i_{Ln}}{i_L} \qquad\qquad (16.2b)$$

The adaptive control thus prevents the loop gain from changing when the inductor current level changes, maintaining the system poles at their nominal values. Note that, as mentioned previously, this method does not provide protection against changes in output capacitance.

Variations in both the inductor current and the output capacitance C can be neutralized if the gains g_2 and g_3 are scaled by the quantity i_L/C, instead of just by i_L as in the previous method. However, while the measurement of i_L is straightforward, the quantity i_L/C is somewhat elusive. Continuous measurement of the capacitance C in a working circuit seems impractical at best.
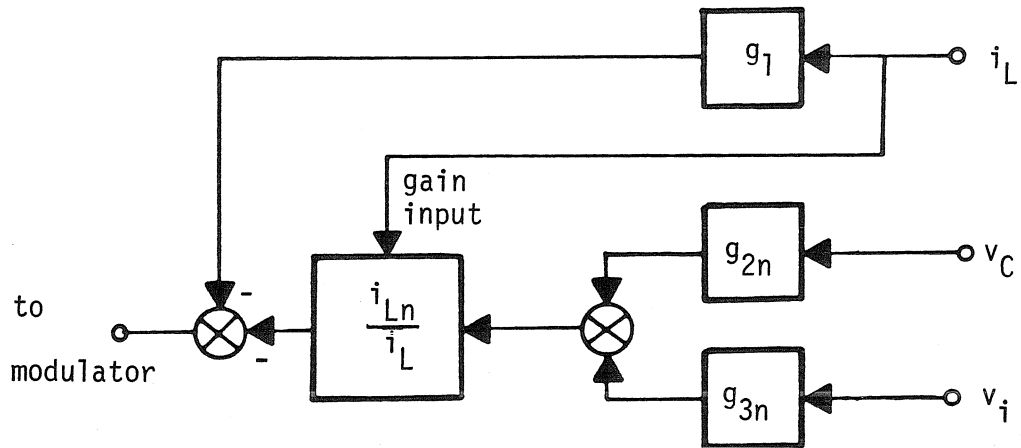
Figure 16.1. *Current-sensing adaptive control scheme for a boost regulator.*
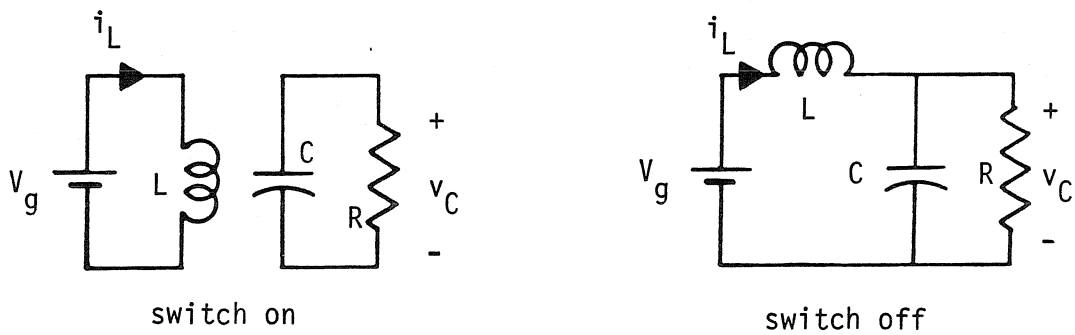
Figure 16.2. *Successive topologies assumed by a boost converter during its operation.*

However, there is another technique whereby the quantity i_L/C can be measured directly.

Consider the two topologies occurring in the boost converter during its operation, as illustrated in Fig. 16.2. It is straightforward to write the derivative of the output voltage v_C in these two conditions.

$$\frac{dv_C}{dt}_{(on)} = -\frac{v_C}{RC} \qquad \text{(switch on)} \qquad (16.3\text{a})$$

$$\frac{dv_C}{dt}_{(off)} = \frac{i_L}{C} - \frac{v_C}{RC} \qquad \text{(switch off)} \qquad (16.3\text{b})$$

If these two equations are subtracted, and it is assumed that the output voltage v_C is the same for both, the desired quantity results.

$$\frac{i_L}{C} = \frac{dv_C}{dt}_{(off)} - \frac{dv_C}{dt}_{(on)} \qquad (16.4)$$

From these considerations the configuration shown in Fig. 16.3 can be used to implement this adaptive control method. The notation is the same as in the block diagram, Fig. 16.1, of the previous adaptive control scheme. However, in this case the constant in the non-linear amplifier is the nominal value of i_L/C, $(i_L/C)_n$, and the quantity i_L/C is constructed as the difference between the values of samples taken at the differentiator output during the on and off periods of the converter switch. The sampling instants for these two sample-and-hold devices should be kept close together, as illustrated in Fig. 16.4, to assure that the output voltage v_C does not change appreciably between these two times, as assumed in the derivation of this construction technique.

Thus, two different adaptive control schemes have been devised for use with
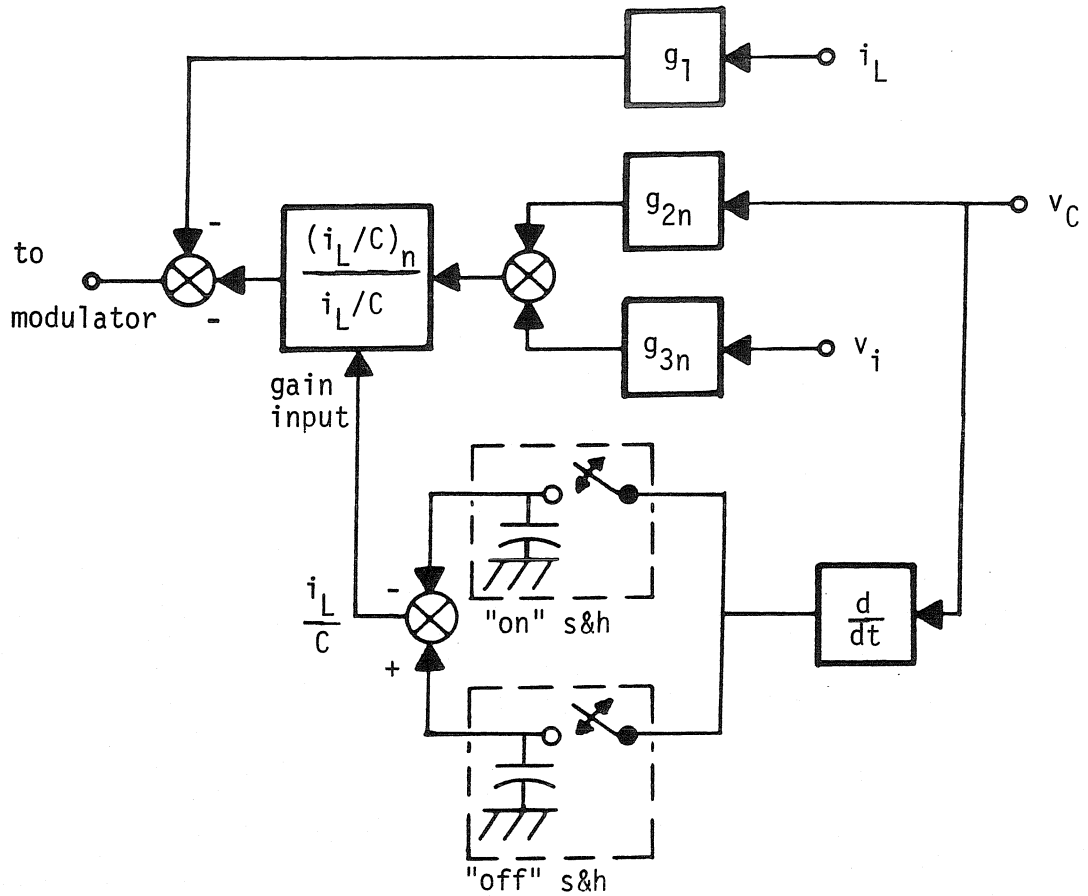
Figure 16.3. *Current-and-capacitance-sensing adaptive control scheme for a boost regulator.*
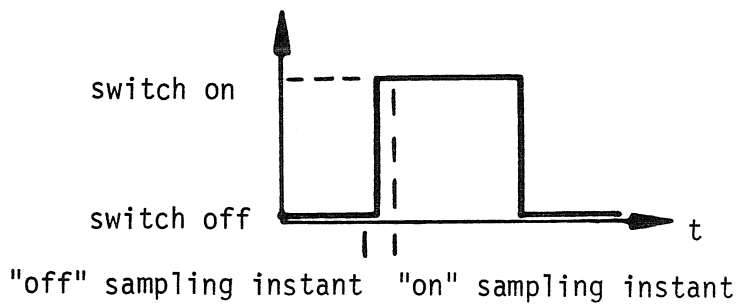
Figure 16.4. *Preferred locations of sampling instants in a switching cycle.*

boost regulators, the two methods differing in both power and complexity. A feature they possess in common, however, is the addition of extra circuitry in the regulator's feedback path. It is conceivable that these additions could affect some other aspect of the regulator's behavior, and the next section will investigate this possibility.

16.3 Effect of additional feedback paths in adaptively controlled regulators

In each of the adaptive schemes just discussed, inspection of the block diagram shows that the implementation of the system results in a new feedback path for the inductor current, through the nonlinear amplifier, that is not present in the non-adaptive case. To understand the effect of this additional feedback path, suppose that the output capacitance is at its nominal value. Then the feedback signal v_m sent to the modulator is the same in the two adaptive systems.

$$v_m = -[g_1 i_L + \frac{i_{Ln}}{i_L}(g_{2n} v_C + g_{3n} v_i)] \tag{16.5}$$

To evaluate the effects of this new appearance of the inductor current i_L, consider a small-signal perturbation of this quantity about a steady-state condition.

$$\hat{v}_m = -\left[g_1 \hat{i}_L + \frac{i_{Ln}}{\overline{i}_L}(g_{2n} \hat{v}_c + g_{3n} \hat{v}_i) \right.$$

$$\left. - \frac{i_{Ln}}{\overline{i}_L}(g_{2n}\overline{v}_C + g_{3n}\overline{v}_i)\frac{\hat{i}_L}{\overline{i}_L} \right] \tag{16.6}$$

Thus the adaptive control results in a change in the effective current feedback gain.

$$\hat{v}_m = -\left\{\left[g_1 - \frac{i_{Ln}}{\bar{i}_L^2}(g_{2n}\bar{v}_C + g_{3n}\bar{v}_i)\right]\hat{i}_L\right.$$

$$\left.+ \frac{i_{Ln}}{\bar{i}_L}(g_{2n}\hat{v}_C + g_{3n}\hat{v}_i)\right\} \tag{16.7}$$

This additional component of current gain appears to depend strongly on the converter operating condition, and thus adaptive control seems to be causing the very problem that it was supposed to eliminate. It can be shown, however, that in many cases this effect is easily taken into account. From the original feedback law, Eq. (16.5), the additional current gain in the small-signal feedback expression, Eq. (16.7), can be rewritten in terms of the modulator voltage, the inductor current gain, and the inductor current.

$$-\frac{i_{Ln}}{\bar{i}_L^2}(g_{2n}\bar{v}_c + g_{3n}\bar{v}_i) = g_1 + \frac{\bar{v}_m}{\bar{i}_L} \tag{16.8}$$

This expression can be substituted back into the small-signal feedback law.

$$\hat{v}_m = -\left[\left(2g_1 + \frac{\bar{v}_m}{\bar{i}_L}\right)\hat{i}_L + \frac{i_{Ln}}{\bar{i}_L}(g_{2n}\hat{v}_C + g_{3n}\hat{v}_i)\right] \tag{16.9}$$

In the high-gain systems considered in this thesis, it is often the case that the current feedback gain g_1 is much larger than the ratio of the modulator voltage to the inductor current, and the feedback law reduces to a simple from.

$$\hat{v}_m \approx -\left[2g_1\hat{i}_L - \frac{i_{Ln}}{\bar{i}_L}(g_{2n}\hat{v}_C + g_{3n}\hat{v}_i)\right] , \quad \frac{\bar{v}_m}{\bar{i}_L} \ll 2g_1 \tag{16.10}$$

In cases where this inequality holds, then, the effect of the extra current feed-

back path is just to double the current gain of the analogous non-adaptive system. Thus, in the construction of such an adaptive control system, the current feedback amplifier must have only one-half the value it would have in a non-adaptive cirucit in order for the system to possess the desired nominal dynamics.

16.4 Adaptive control possibilities for other topologies

The previous adaptive control schemes are, of course, suitable only for boost regulators, since the adaptive features employed depend on the characteristics of the system loop gain. The same ideas, however, may be applied to the other basic converter topologies. In this section, the simplified loop gains for each of these systems will be presented, and useful adaptive possibilities will be listed. In each case, the same uniformly sampling modulator used in the boost example is assumed, with V_M the magnitude of the modulator's artificial ramp.

For the buck converter, illustrated in Fig. 16.5, the state vector x and effective feedback gain vector H_e are defined analogously to the boost case.

$$x = \begin{bmatrix} i_L \\ v_C \\ v_i \end{bmatrix} \qquad H_e = \frac{1}{V_M} \begin{bmatrix} g_1 \\ g_2 \\ g_3 \end{bmatrix} \qquad (16.11)$$

The loop gain for this system can be evaluated and simplified in the same manner as that for the boost regulator.

$$T_z(z) \approx \frac{V_g T_s}{V_M L} \left\{ \frac{g_1}{z-1} + \frac{1}{C} \left[g_2 + \frac{g_3 T_s}{z-1} \right] T_s \frac{D'z + D}{(z-1)^2} \right\} \qquad (16.12)$$

Two adaptive possibilities can be seen. First, the sum of the feedback signals
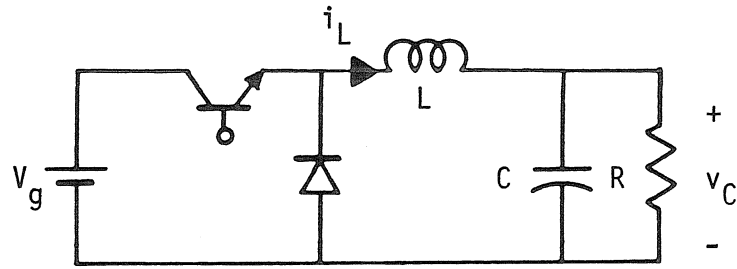
Figure 16.5. *Buck converter topology.*
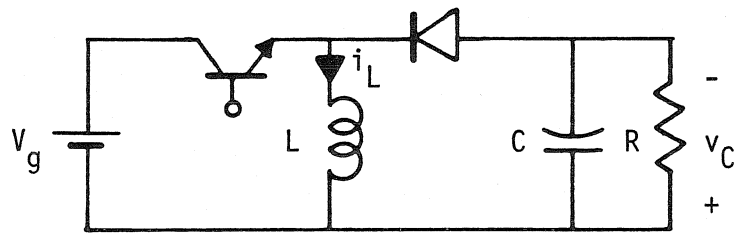
Figure 16.6. *Buck-boost converter topology.*
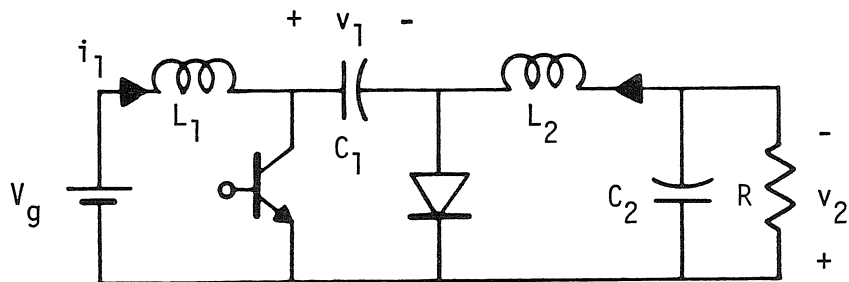
Figure 16.7. *Ćuk converter topology.*

might be scaled by the input voltage V_g, or, equivalently, the artificial ramp magnitude V_M might be made proportional to V_g. This technique would desensitize the regulator dynamics to input voltage changes. Second, the effects of variation in output capacitance could be reduced if the gains g_2 and g_3 were made proportional to the capacitance C. A measure of this capacitance might be obtained from the ratio of the capacitor current i_C to the rate of change of the output voltage v_C.

$$C = \frac{i_C}{\dfrac{dv_C}{dt}} \tag{16.13}$$

Treatment of the buck-boost converter proceeds in exactly the same fashion. From its representation in Fig. 16.6, the buck-boost's state vector x and effective feedback gain vector H_e are formulated.

$$x = \begin{bmatrix} i_L \\ v_C \\ v_i \end{bmatrix} \qquad H_e = \frac{1}{V_M} \begin{bmatrix} g_1 \\ g_2 \\ g_3 \end{bmatrix} \tag{16.14}$$

Calculation of the loop gain for such a buck-boost regulator gives the following approximate form.

$$T_z(z) \approx \frac{T_s}{V_M} \left\{ g_1 \frac{V_C + V_g}{L} \frac{1}{z-1} - \frac{I_L}{C} \left[\frac{g_2}{z-1} + g_3 T_s \frac{D'z + D}{(z-1)^2} \right] \right\} \tag{16.15}$$

Examination of this expression shows that the effects of input voltage variations can be reduced if the gain g_1 is scaled by the sum of the output and input voltages. In fact, since the output voltage is held constant by the regulator, only a constant need be added to the input voltage V_g to obtain the desired effect. In

addition, as for the boost case, a second potential source of high sensitivity is the appearance of the ratio of inductor current i_L to the output capacitance C. Similar problems have similar solutions, and here the sensitivity is alleviated if the gains g_2 and g_3 are scaled by the quantity i_L/C, measured in the same manner as for the boost converter. Note that, as in the boost case, the extra inductor current feedback path will result in a change in the effective inductor current feedback gain. The analysis of this effect follows that for the boost regulator exactly, with the same factor of two increase in the resulting effective inductor current gain.

Finally the Ćuk converter, illustrated in Fig. 16.7, is considered. The analysis in this case is complicated by the large number of states in this converter, but the procedure is the same as in the previous cases. The state vector x and effective gain vector H_e now have five components each.

$$
x = \begin{bmatrix} i_1 \\ i_2 \\ v_1 \\ v_2 \\ v_i \end{bmatrix} \qquad H_e = \frac{1}{V_M} \begin{bmatrix} g_1 \\ g_2 \\ g_3 \\ g_4 \\ g_5 \end{bmatrix} \tag{16.16}
$$

Similarly, the approximate loop gain $T_z(z)$ now has five terms.

$$
T_z(z) \approx \frac{T_s}{V_M} \left[\frac{g_1}{z-1} \frac{V_1}{L_1} + \frac{g_2}{z-1} \frac{V_1}{L_2} - \frac{g_3}{z-1} \frac{I_1+I_2}{C_1} \right.
$$

$$
\left. + \frac{V_1 T_s}{L_2 C_2} \left(g_4 + \frac{g_5 T_s}{z-1} \right) \frac{D'z+D}{(z-1)^2} \right] \tag{16.17}
$$

Here a variety of possibilities for adaptive control present themselves. The gains g_1, g_2, g_4, and g_5 can be scaled by the voltage v_1 across the capacitor C_1, which

effectively helps to desensitize the circuit to changes in the input voltage V_g, since, as is easily shown, the sum of the input and output voltages is just the average voltage across C_1. Second, the sum of the inductor currents i_1+i_2 can be used to scale the gain g_3, and, finally, protection against changes in the output capacitance C_2 can be obtained if the gains g_4 and g_5 are made proportional to this capacitance. Note that, if quantities are scaled according to v_1 and the sum i_1+i_2, additional state feedback paths will be introduced. These new paths must be taken into account in the determination of the effective feedback gains. Obviously, these techniques do not all have to be used simultaneously; a sensitivity analysis would indicate which methods would be most effective for a particular design.

16.5 Conclusions

This chapter has presented various applications of adaptive control to high-performance switching regulators, with the aim of reducing the possibly excessive sensitivity of these systems. Two different techniques were introduced for the boost regulator, which again in this chapter served as an example for the discussion. One method protects against changes in steady-state inductor current, while the other, at a cost of greater complexity, also provides a defense against changes in output capacitance. A by-product of both schemes was discovered in the form of an additional feedback path introduced by the adaptive circuitry; this new path modifies one of the effective feedback gains in an undesirable manner. Fortunately, it was found that, in the high-performance systems where these adaptive schemes are valuable, this gain modification can be easily taken into account and neutralized.

Analogous adaptive strategies were then discussed for the other basic con-

verter topologies. While differing in detail from the boost regulator methods, the techniques used in the developments of these schemes are the same as those used in the boost case. For a regulator with several different adaptive possibilities, it was pointed out that sensitivity analyses of the type illustrated previously for the boost regulator can be applied to determine which methods are appropriate for a given design.

CHAPTER 17

EXPERIMENTAL PERFORMANCE OF ADAPTIVELY CONTROLLED REGULATORS

17.1 Introduction

The previous chapters of this third part of this thesis have introduced the problem of sensitivity in high-performance switching regulator systems and proposed adaptive control systems as a means for the reduction of this sensitivity. In this present chapter these findings will be illustrated for a specific boost regulator.

In Section 17.2 a design procedure for a conventional, non-adaptive system is summarized. The sensitivity of this design is then estimated for three choices of closed-loop dynamics. The degree of sensitivity is seen to grow with the level of feedback gain, as expected. A design of intermediate sensitivity is chosen for implementation in Section 17.3. There the experimental system, which can function with use of either conventional, non-adaptive control or one of the two adaptive schemes introduced in Chapter 16, is described. Also discussed is a method for the investigation of the nature of the dynamic behavior of these systems, which involves observation of the output voltage response to a step change in the load resistance.

The next three sections discuss the experimental characteristics of each of the possible configurations of the constructed system. In Section 17.4 the conventional, non-adaptive regulator is seen to suffer from acute sensitivity to changes in load resistance, input voltage, and output capacitance. In contrast, the current-sensing adaptive technique, investigated in Section 17.5, vastly reduces the sensitivity to load and input changes, although the effects of a change in output capacitance are unmitigated. In Section 17.6 the current-

and-capacitance-sensing adaptive technique, while vulnerable to noise problems owing to a differentiator employed in the circuit, is shown to be successful in moderating the effects of all three changes in external conditions. Finally, conclusions are presented in Section 17.7.

17.2 Design and sensitivity of an experimental boost regulator

The boost converter of Fig. 17.1 will serve as the basis for the experimental investigations of this chapter. The nominal voltage conversion is from 15 to 30 V at a nominal duty ratio of 0.5. The switching frequency is 50 kHz, and the power level is 12 W. The feedback arrangement is also shown in this figure, and the notation illustrated there will be used in the following discussion.

With use of the values for the power stage components defined in Fig. 17.1 and a value for the magnitude of the artificial ramp of $V_M=2.75$ V, the regulator loop gain $T_z(z)$ of Eq. (15.5) can be explicitly calculated as a function of the feedback gains g_1, g_2, and g_3 and the variable z. Since the equation $1+T_z(z)=0$ defines the closed-loop poles p_1, p_2, and p_3 and since the loop gain is linear in the feedback gains, it is possible to write a matrix equation for these gains in terms of the closed-loop poles.

$$\begin{bmatrix} g_1 \\ g_2 \\ g_3 \end{bmatrix} = Q \begin{bmatrix} 2.94 - (p_1+p_2+p_3) \\ -2.89 + (p_1p_2+p_1p_3+p_2p_3) \\ 0.953 - p_1p_2p_3 \end{bmatrix} \tag{17.1a}$$

$$Q = \begin{bmatrix} 191.1 & 159.4 & 133.9 \\ 17.14 & 14.68 & 11.89 \\ 2.105\times10^4 & 2.105\times10^4 & 2.105\times10^4 \end{bmatrix} \tag{17.1b}$$

Suppose all three closed-loop poles are assigned to the same location p.
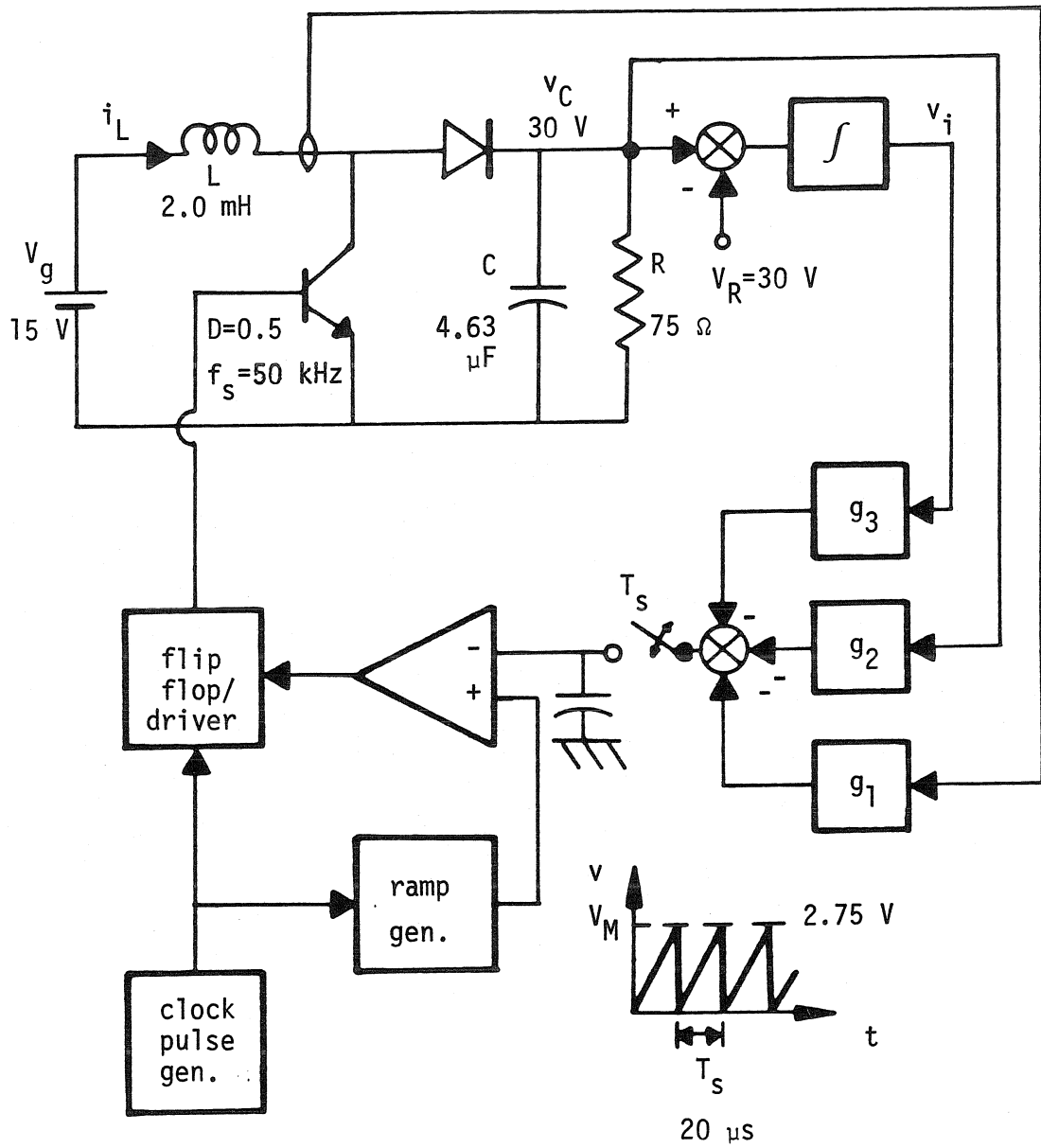
Figure 17.1. *Boost converter used in experimental investigations, with conventional feedback control.*

$$p_1 = p_2 = p_3 = p \qquad (17.2)$$

The necessary gains for three different values of p can be calculated from Eq. (17.1).

$$
\begin{aligned}
p=0.9:\ & g_1=2.53, && g_2=0.0334, && g_3=842 \\
p=0.5:\ & g_1=44.9, && g_2=3.15, && g_3=26900 \\
p=0.0:\ & g_1=229, && g_2=19.4, && g_3=2.11\times10^5
\end{aligned}
\qquad (17.3)
$$

The case in which all poles lie at $z=0.9$ corresponds to a slow system; this regulator will be relatively sluggish in responding to disturbances. A moderately fast system results if all the poles are placed at $z=0.5$, and a finite-settling-time system, briefly illustrated in Appendix A, is obtained when the closed-loop poles are all located at the origin of the z-plane. Note that, as mentioned previously, the fast systems require much larger feedback gains than the slow one.

The expression developed earlier to investigate the sensitivity of boost regulator systems, Eq. (15.13), can now be employed to predict the movement of the closed-loop poles in response to operating point changes. In this case, all three closed-loop poles coincide, unlike the previous case where they were assumed to be separated. Therefore, the relation between a fractional change δ in the quantity I_L/C and the resulting closed-loop pole shift ε is somewhat different from that derived previously. However, the new expression is easily determined. Upon substitution of the circuit parameter values, an expression for the pole shift ε in terms of the fractional change δ, the pole location p, and the feedback gains g_1, g_2, and g_3 is obtained.

$$\varepsilon = \{-1.32\delta[-g_2(p-1)^2 + g_3(10^{-5}p^2 + 3.51\times10^{-6}p + 10^{-6})]\}^{1/3} \qquad (17.4)$$

Suppose $\delta=0.01$, a 1% change in the quantity I_L/C from its nominal value. The resulting closed-loop pole movements for the three designs previously considered are then easily calculated.

$$
\begin{aligned}
p &= 0.9 &\rightarrow& \quad |\varepsilon| = 0.06 \\
p &= 0.5 &\rightarrow& \quad |\varepsilon| = 0.22 \\
p &= 0.0 &\rightarrow& \quad |\varepsilon| = 0.61
\end{aligned}
\tag{17.5}
$$

These results agree with the earlier qualitative finding that sluggish systems with small feedback gains display less sensitivity than fast systems with large gains. This calculation predicts that a fast system with no adaptivity will display wide variations in its dynamic characteristics as the operating conditions change.

17.3 Description of experimental circuit and measurement technique

To demonstrate the effects of adaptive control, the moderately fast system, with nominal pole locations all at $z=0.5$, was chosen to be implemented in the experimental system. This intermediate design is predicted to have high sensitivity, but not so high that the non-adaptive version is impossible to maintain in a stable configuration. A block diagram of the constructed system is presented in Fig. 17.2. With the switches S1, S2, and S3 in appropriate positions, any of the three boost regulator control schemes discussed previously, the non-adaptive, current-sensing adaptive, and current-and-capacitance-sensing adaptive systems, may be implemented. The switch S1 routes the feedback signal either through or around the adaptive circuit, and within that circuit the switch S2 chooses one of the quantities i_L or i_L/C to be scaled adaptively. The inductor current feedback gain is set by switch S3; for the adaptive schemes this gain is reduced by one-half relative to its value in the non-adaptive case. This adjust-
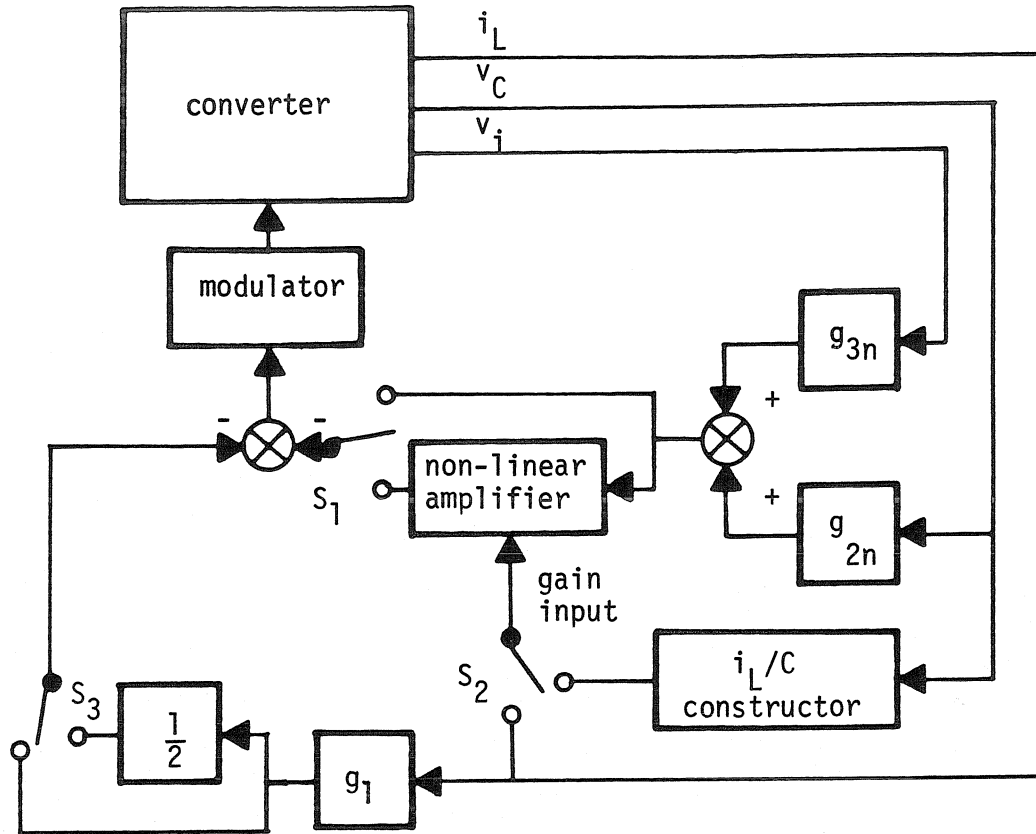
Figure 17.2. *Block diagram of experimental system.*
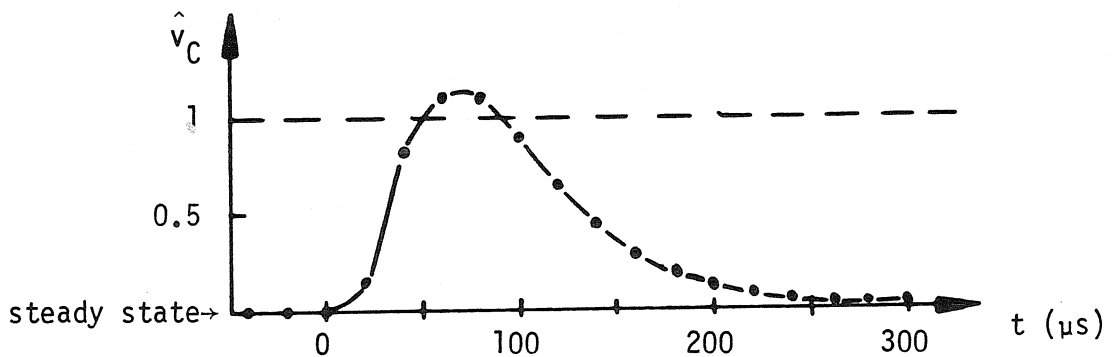
Figure 17.3. *Expected output voltage deviation from steady state, sampled at beginning of each switching period, for a load step from 69 Ω to 75 Ω.*

ment, as discussed earlier, compensates for the additional inductor current feedback path existing in the adaptive cases. For this circuit, the inequality requirement on the current gain, given in Eq. (16.10), for the simple compensation rule to hold is well-satisfied. Compared to the current gain of 45, the ratio $\overline{v}_m/\overline{i}_L$, which is never greater than 5, can be neglected.

The three implemented control schemes were all matched with respect to their dynamic behaviors under nominal circuit operating conditions, as will be evidenced in the measurements to be presented. Time-domain measurements, rather than frequency responses, will be used to compare the performances of these designs. This measurement technique allows the transient response of the system to be seen directly. The basic measurement is to monitor the output voltage response to a step change in load resistance. Before the load step, the regulator is in a steady-state condition corresponding to the value of the original load resistance. Immediately after the load step, the regulator state is unchanged, but this state is not in equilibrium with the new value of load resistance. The system therefore evolves, in accordance with its dynamic characteristics, into the appropriate new steady-state condition. Analytically, this process can be thought of as an initial value problem, with the load step occurring at time zero. The use of the original state equation, Eq. (15.3), together with the feedback law Eq. (15.2), allows predictions for this response to be formulated.

$$\hat{x}[(n+1)T_s] = [e^{A_2D'T_s}e^{A_1DT_s} - e^{A_2D'T_s}KT_sH_e^T]\hat{x}[nT_s] \qquad (17.6)$$

When specific values for circuit components and feedback gains are substituted into this expression, and the value of $\hat{x}[0]$ is determined from the steady-state condition before the load step, it is found that the expected output voltage response for a load step from 69 Ω to the nominal value of 75 Ω appears as in

Fig. 17.3. Because the discrete modeling technique only predicts the state at one instant in each switching cycle, the expected plot appears only as a series of points; the connecting curves containing the switching ripple are left out.

The following sections will examine the experimental performance of the non-adaptive, current-sensing adaptive, and current-and-capacitance-sensing adaptive feedback schemes. Output voltage responses to load steps will be examined under several operating conditions, including nominal operating conditions, high load, low and high input voltage, and with the addition of extra output capacitance. Comparisons of the responses in these various situations will reveal the differences between the three control methods.

17.4 Performance of non-adaptive control scheme

The performance of a conventional, non-adaptive design is illustrated in Figs. 17.4-17.7. In Fig. 17.4 both input voltage V_g and output capacitance C have their nominal values. Since the nominal load is 75 Ω, the top oscilloscope trace, showing the response to a load step from 69 Ω to 75 Ω, represents the nominal circuit response to a set of initial conditions and is comparable to the prediction of Fig. 17.3. The close agreement of these two waveforms confirms that the desired behavior has been achieved for nominal conditions.

On the other hand, the bottom trace of this figure, the output voltage response for the transition from 75 Ω to 69 Ω, illustrates the sensitivity problem. Even though the change in operating condition is relatively small, the regulator's dynamic behavior shows dramatic deterioration. A calculation of the pole positions for this set of circuit conditions (load resistance = 69 Ω) confirms the change; the poles originally clustered at 0.5 now appear at 0.75 and $0.54 \pm j0.51$. The complex poles lead to the oscillatory behavior observed in the

- 191 -

69 Ω → 75 Ω
(nominal response)

75 Ω → 69 Ω
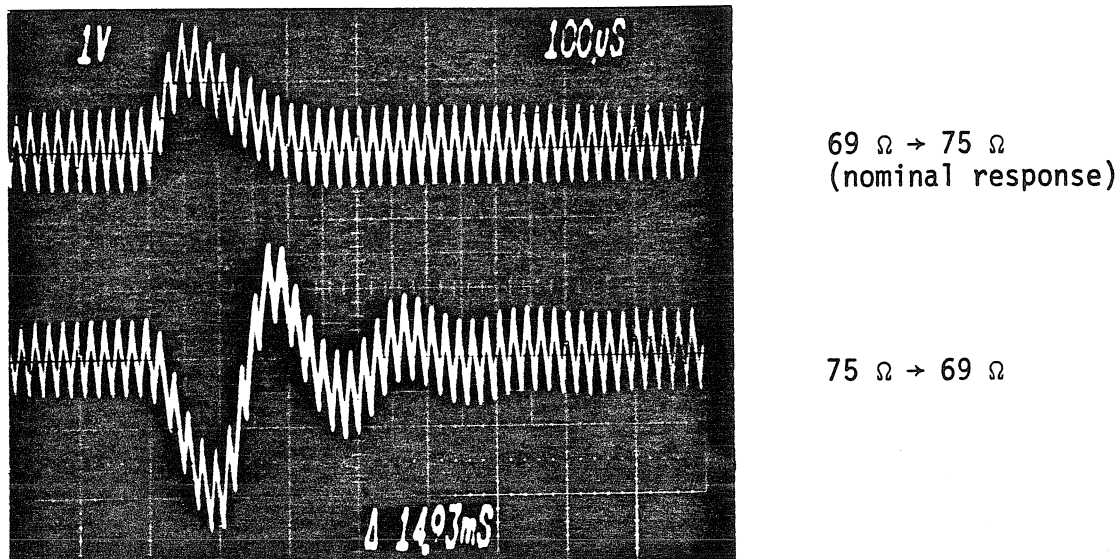
Figure 17.4. *Non-adaptive control performance: output voltage transient response under nominal conditions* $(V_g = 15\ V,\ C = 4.63\ \mu F)$.

70 Ω → 75 Ω

75 Ω → 70 Ω
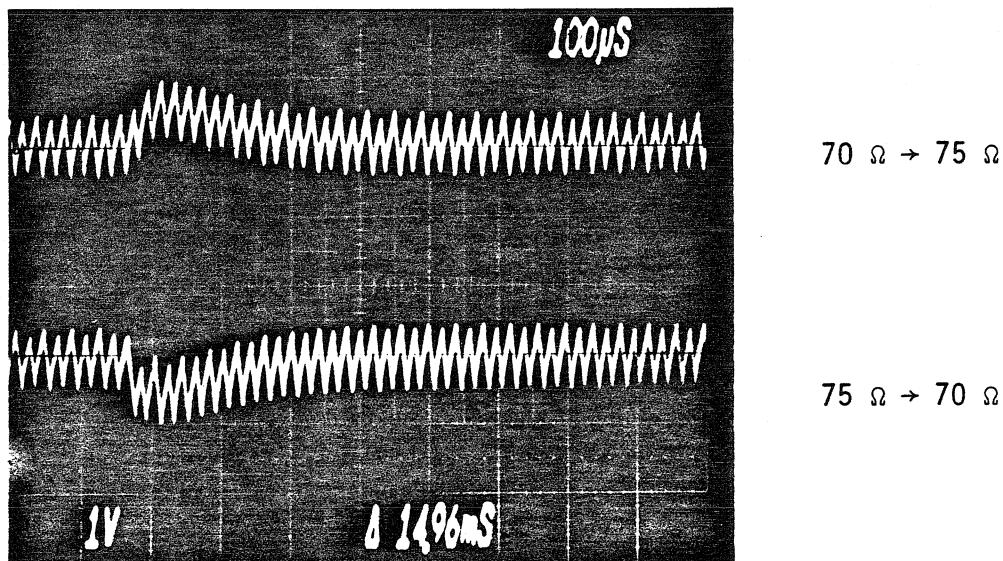
Figure 17.5. *Non-adaptive control performance: output voltage transient response under high input voltage* $(V_g = 20\ V)$.
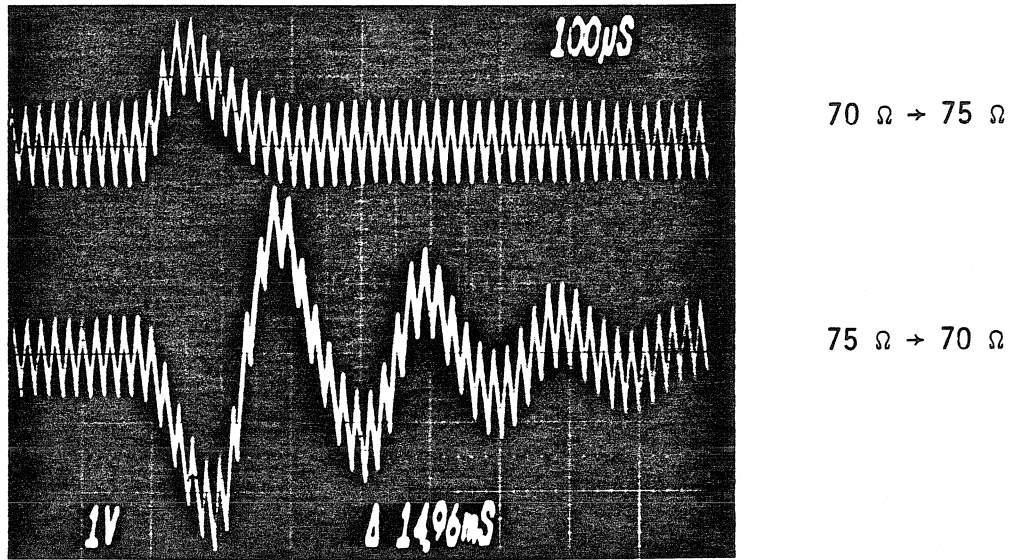
Figure 17.6. *Non-adaptive control performance: output voltage transient response under low input voltage (V_g=14.4 V).*
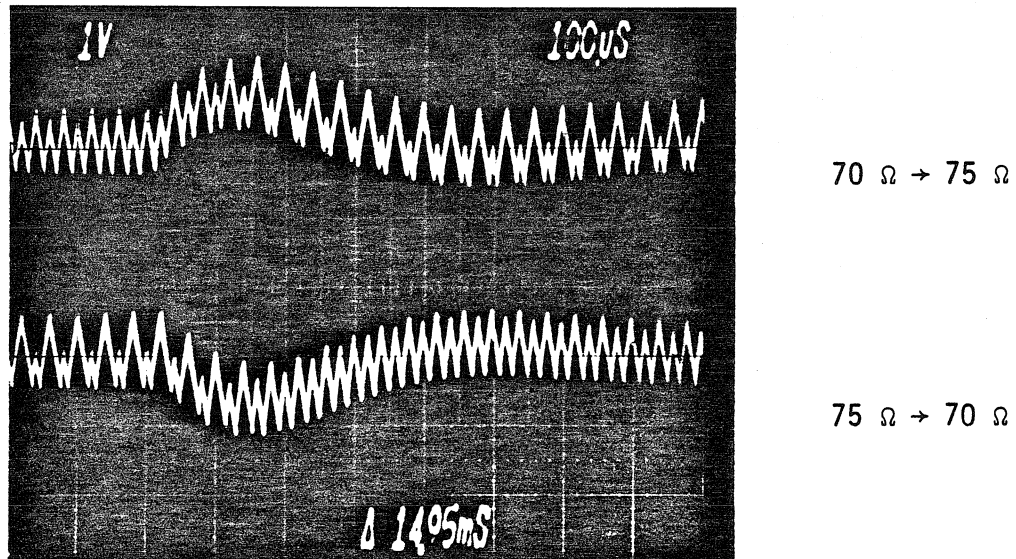
Figure 17.7. *Non-adaptive control performance: output voltage transient response under excess output capacitance (C=6.8 μF).*

photograph.

The next two photographs, Figs. 17.5 and 17.6, show the output response for load steps between 70 Ω and 75 Ω under high and low values of the input voltage V_g, which has a nominal value of 15 V. The system dynamics remain well-behaved for input voltages even well above nominal, as seen in Fig. 17.5, but the traces of Fig. 17.6 show that a fall in V_g aggravates the deterioration already encountered for load resistances below the nominal value. Indeed, for an input voltage any lower than the 14.4 V of Fig. 17.6, the regulator becomes unstable.

Finally, Fig. 17.7 shows the result of an increase in the output capacitance by 50%. A severe subharmonic oscillation occurs in this instance, making the regulator unusable. Thus, in all three categories of operating point change considered, the conventional, non-adaptive regulator possesses extreme sensitivity. The following sections will demonstrate the effectiveness of adaptive control in the reduction of this sensitivity.

17.5 Performance of current-sensing adaptive control technique

The photographs of Figs. 17.8-17.11 correspond to the oscilloscope traces of Figs. 17.4-17.7, but now the current-sensing adaptive control scheme is employed. The nominal output response, represented by the top trace of Fig. 17.8, matches that of the non-adaptive case closely, confirming the equality of the nominal dynamics of the two systems. However, the contrasts between the bottom traces of Figs. 17.8 and 17.4 and between Figs. 17.10 and 17.6, demonstrate the benefits resulting from the adaptive scheme.

With current-sensing adaptive control, little or no degradation in dynamic performance occurs as the input voltage or load resistance of the converter changes. Thus, in the bottom trace of Fig. 17.8, the output voltage response

69 Ω → 75 Ω
(nominal response)

75 Ω → 69 Ω
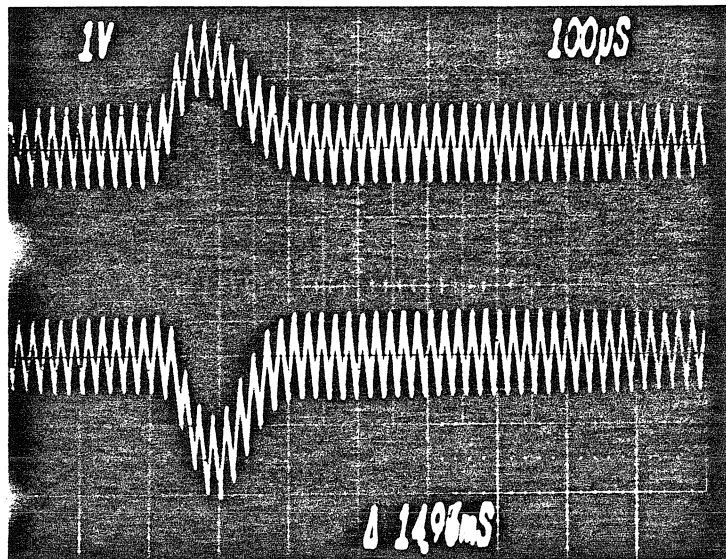
Figure 17.8. *Current-sensing adaptive control performance: output voltage transient response under nominal conditions (V_b=15 V, C=4.63 μF).*

70 Ω → 75 Ω

75 Ω → 70 Ω
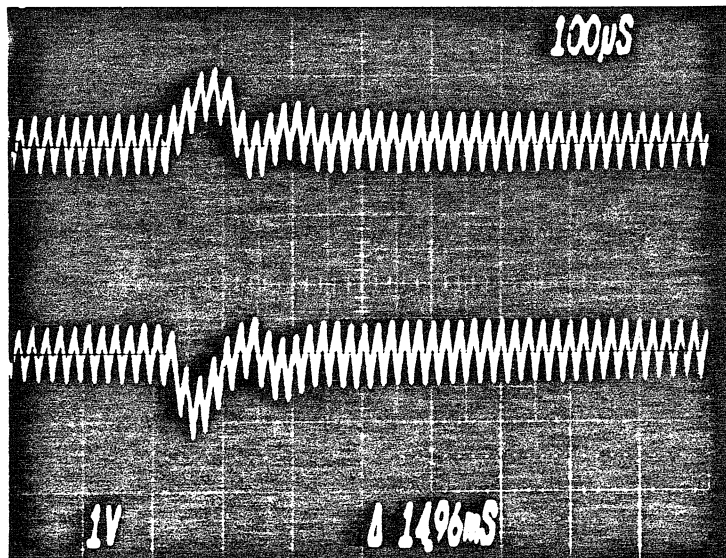
Figure 17.9. *Current-sensing adaptive control performance: output voltage transient response under high input voltage (V_g=20 V).*

70 Ω → 75 Ω

75 Ω → 70 Ω
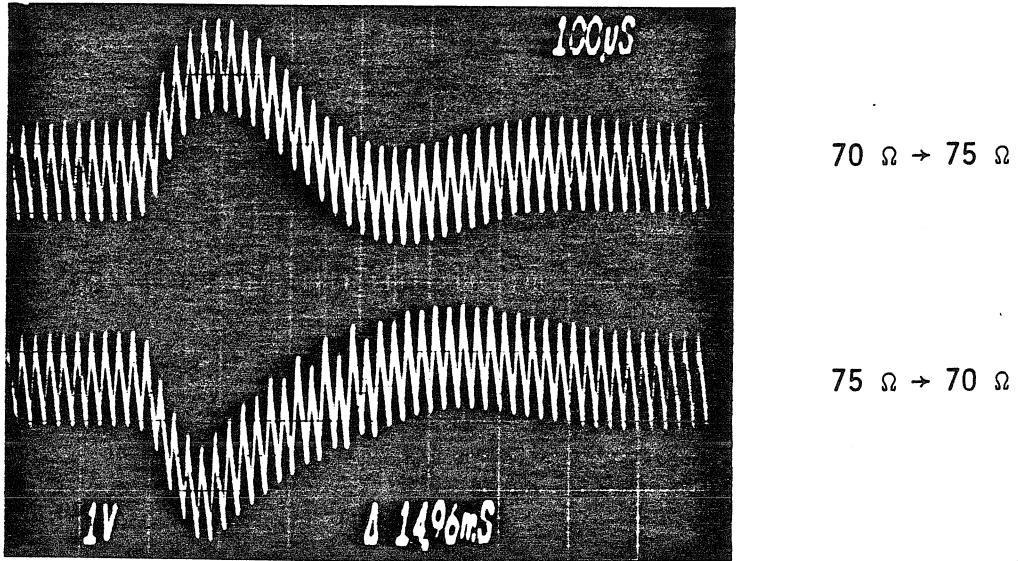
Figure 17.10. *Current-sensing adaptive control performance: output voltage transient response under low input voltage (V_g =12 V).*

70 Ω → 75 Ω

75 Ω → 70 Ω
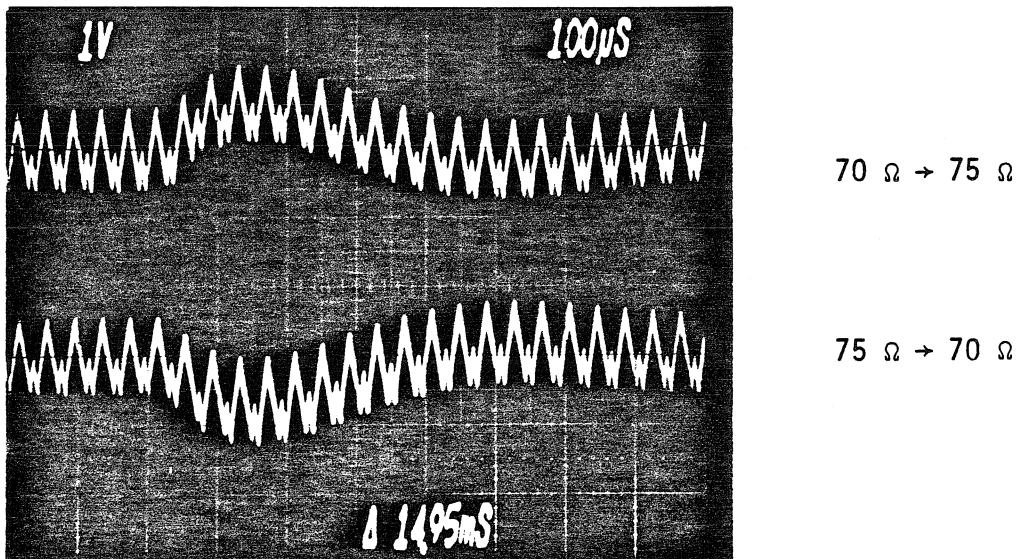
Figure 17.11. *Current-sensing adaptive control performance: output voltage transient response under excess output capacitance (C =6.8 μF).*

mirrors the nominal characteristic of the upper trace, in contrast to the oscilla-
tory waveform observed in the non-adaptive system. Furthermore, note that in
Fig. 17.10 the input voltage V_g has been reduced to 12 V, at which point the
power inductor is in danger of saturating. Only a small deviation from the nomi-
nal dynamic behavior of the regulator is observed in this situation, contrasting
sharply with the non-adaptive responses of Fig. 17.6, in which the input voltage
could not be reduced below 14.4 V without encountering instability. Like the
non-adaptive case, performance remains good when the input voltage is raised
above nominal.

The current-sensing adaptive control technique does not cure all ailments,
however. For example, it will not alter the feedback gains if the output capaci-
tance is changed. This shortcoming is illustrated in Fig. 17.11; as expected,
subharmonic oscillations again arise when extra output capacitance is added to
the output of the current-sensing adaptive regulator. Improvement in this
situation requires current-and-capacitance-sensing adaptive control, which is
examined in the next section.

17.6 Performance of current-and-capacitance-sensing adaptive control technique

The third system to be investigated experimentally employs the current-and-
capacitance-sensing adaptive network. Before the discussion of the performance
in this case, a few words should be said about the hardware implementation of
this technique. As was mentioned earlier, the measurement of the quantity i_L/C
in this method requires the use of a differentiator. As is common when
differentiators are employed in noisy environments, noise amplification prob-
lems result. The situation is aggravated by the requirement that the
differentiator respond in a few microseconds to step changes in input slope, so

70 Ω → 75 Ω
(nominal response)

75 Ω → 70 Ω
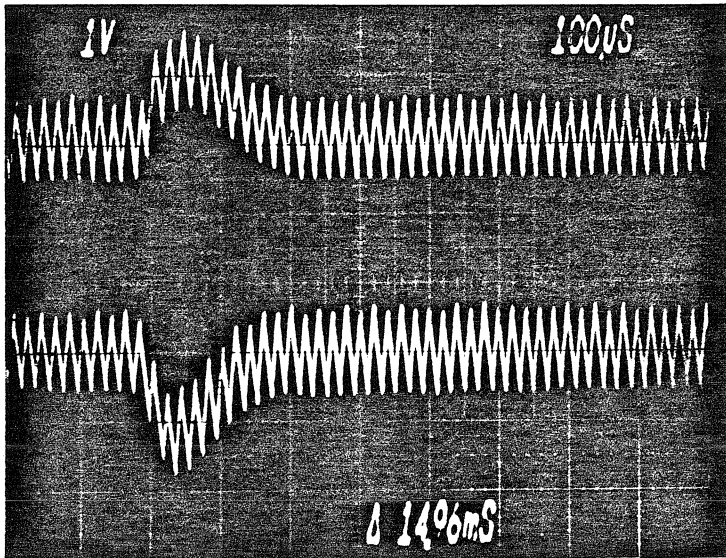
Figure 17.12. *Current-and-capacitance-sensing adaptive control performance: output voltage transient response under nominal conditions (V_g =15 V, C =4.63 μF).*

70 Ω → 75 Ω

75 Ω → 70 Ω
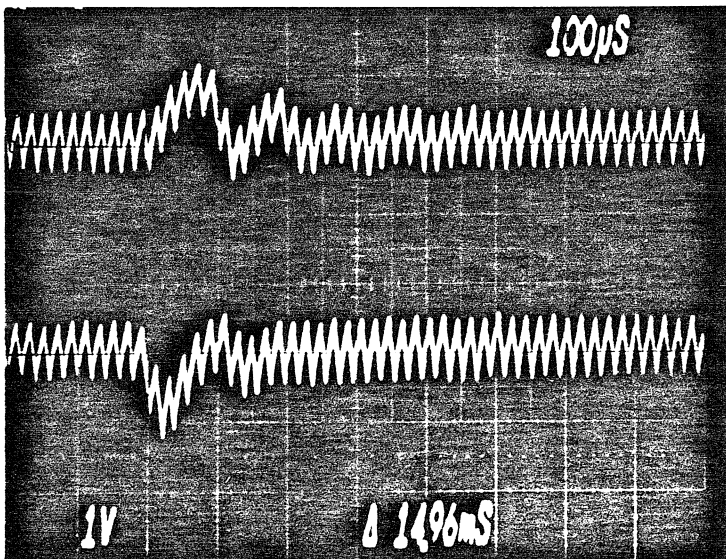
Figure 17.13. *Current-and-capacitance-sensing adaptive control performance: output voltage transient response under high input voltage (V_g =20 V).*
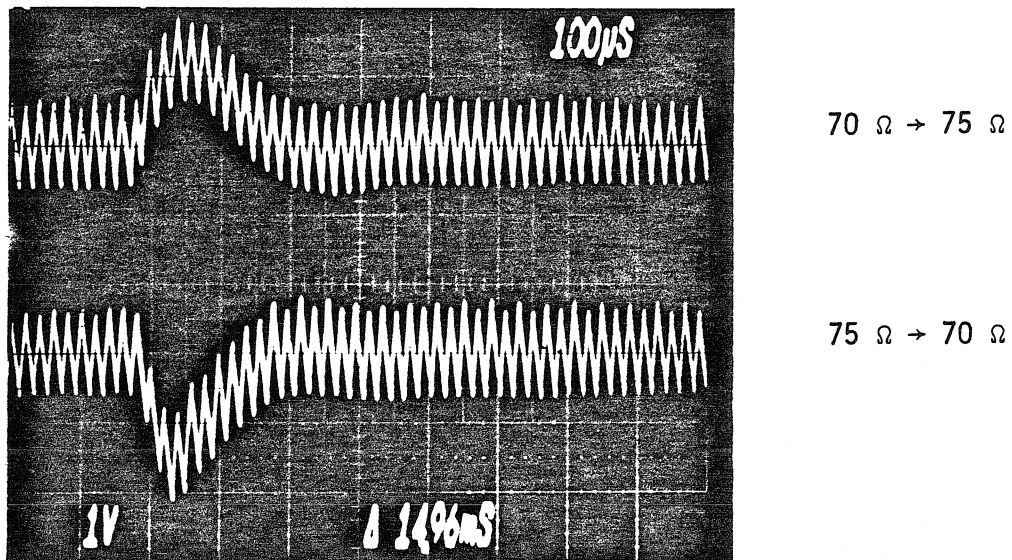
Figure 17.14. *Current-and-capacitance-sensing adaptive control performance: output voltage transient response under low input voltage (V_g =14 V).*
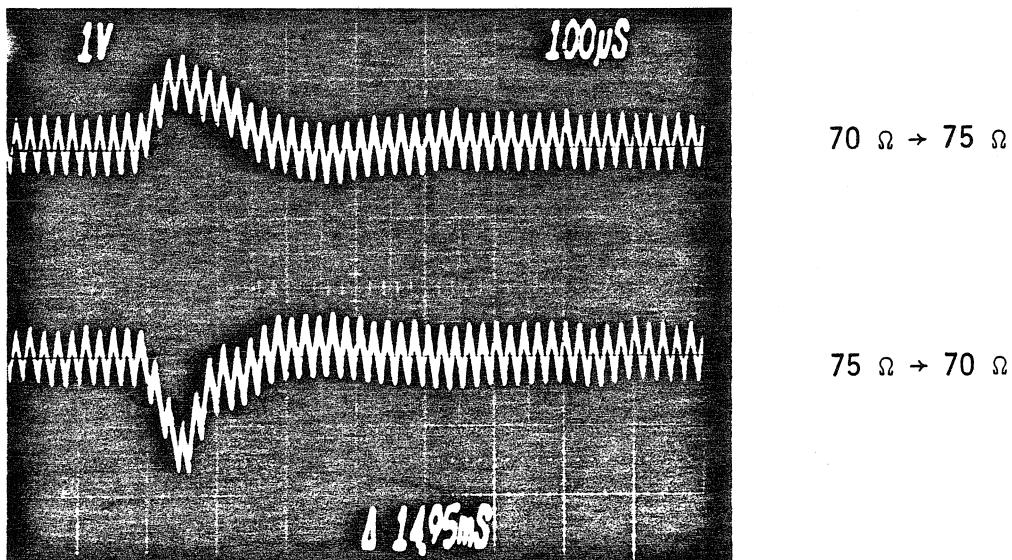
Figure 17.15. *Current-and-capacitance-sensing adaptive control performance: output voltage transient response under excess output capacitance (C =8.8 μF).*

that the samplers used to construct the quantity i_L/C receive the correct values. Thus, a large bandwidth for the differentiator is required. In the actual circuit, high-frequency filters and careful layout were used to reduce, but not entirely eliminate, noise effects.

The performance of the current-and-capacitance-sensing control scheme is illustrated in the photographs of Figs. 17.12-17.15, which correspond with the waveforms displayed for the other control schemes. The first three photographs, Figs. 17.12-17.14, show that the benefits accompanying the current-sensing adaptive control scheme are also found here, although the range of allowable parameter variation is not as great in the present case, a probable result of the noise effects discussed earlier. The additional value of this scheme appears in Fig. 17.15, where, in spite of the 50% increase in output capacitance, the regulator dynamics remain excellent, free of the subharmonic limit cycle which plagued the earlier systems. Thus, at the cost of a more complex feedback network and a greater need for careful layout procedures, the current-and-capacitance-sensing adaptive control scheme greatly reduces the sensitivity of boost regulators to all major forms of external operating condition changes.

17.7 Conclusions

This chapter has investigated the effects of three control methods, one non-adaptive and two adaptive, on the performance of an experimental boost regulator. Design equations giving the nominal feedback gains in terms of the desired pole locations were presented, and the sensitivity of the conventional, non-adaptive regulator was estimated for various pole locations, representing both low-performance and high-performance systems. The sensitivity was seen to increase greatly as the performance level increased.

A design of intermediate performance and sensitivity was chosen to be implemented experimentally, so that the sensitivity effects would be large enough to be seen but not too large to be controlled by the non-adaptive system. The experimental system constructed could be configured to employ either the non-adaptive control scheme or one of the two adaptive control techniques developed earlier, all with the same dynamics for the case of nominal circuit conditions. Time-domain measurements of the output voltage response to a load step were introduced as a means for the comparison of their performances, and a prediction for this response under nominal circuit conditions was presented.

The performances of the three control schemes were then examined for a set of conditions consisting of nominal conditions, high load, low and high input voltage, and excess output capacitance. The dynamic behavior of the conventional, non-adaptive regulator displayed extreme sensitivity to all these variations, confirming the earlier predictions. The current-sensing adaptive scheme, in contrast, greatly reduced the sensitivity to changes in load and input voltage, allowing a much greater dynamic range to be achieved. As expected, it was of no help in the case of increased output capacitance. However, the current-and-capacitance-sensing method, although suffering from noise problems owing to its use of a fast differentiator, succeeded in reducing the sensitivity of the regulator's dynamic properties with respect to all the variations employed. Through use of this system, the dynamic behavior of the regulator was made nearly independent of operating conditions.

CHAPTER 18

CONCLUSIONS

In this final part of this thesis, the sensitivity of high-performance switching regulators with respect to changes in their operating conditions was exposed. This undesirable behavior was shown to lead, in certain cases, to excessive degradation of the dynamic characteristics of these systems. Adaptive feedback control was introduced as a method for the reduction of this sensitivity, so as to maintain the desired regulator dynamic performance over a wide range of circuit environments.

Because the analysis of sensitivity deals with the movement of system poles, the discrete modeling technique was chosen for the analysis, since its representation has only a finite number of such poles, compared with the infinite number of poles in the sampled-data model. Uniformly sampling modulators were also introduced in order to eliminate the interaction between the artificial ramp of the modulator and the switching ripple on the fed-back waveform. Slight modifications of the discrete modeling process were developed to account for this type of modulator.

With this model examination of the sensitivity problem was undertaken. The boost converter topology was chosen as an example. A simplified expression for the loop gain of a regulator employing this converter was developed, from which the effects of changes in operating conditions on this loop gain, and hence on the regulator's dynamic behavior, could be easily examined. These observations suggested a simple technique for the quantitative estimation of the sensitivity of the system. This method predicts the closed-loop pole movement resulting from a small change in a composite quantity representing the important features of

the circuit operating point. Similar expressions can be developed for the other basic converter topologies.

The understanding of the sensitivity phenomenon gained in this manner also suggested a possible remedy for the problem. This approach makes certain feedback gains functionally dependent on crucial circuit quantities, in order to compensate for the loop gain changes which variations in these quantities induce. For the boost regulator the appropriate quantities are the inductor current and the output capacitance, and consequently the proposed adaptive scheme monitors these parameters and alters feedback gains to correct for changes in them. Two different implementations of this idea were proposed for the boost regulator. One method, simple in design, compensates for changes in inductor current only; the second, at a cost of greater complexity, adjusts for variations in both inductor current and output capacitance. A common feature of these designs is the introduction of a new feedback path in the regulator. Analysis of the resulting system showed that a consequence of this additional path is a modification of one of the effective feedback gains. Correction for this effect, however, was seen to be straightforward for most high-performance systems.

While the detailed analysis performed in the development of these adaptive techniques applies only to the boost regulator, the same ideas can be employed for the other basic converter topologies. Simplified loop gains for these other systems were presented, and appropriate adaptive strategies for each were suggested. Sensitivity analyses can determine which adaptive techniques are applicable in a given case.

For confirmation of the above findings, the performance of an experimental boost regulator was investigated. The design of the nominal feedback

configuration was outlined, and the sensitivity of various designs was estimated.
An intermediate level of performance and sensitivity was used for the actual im-
plementation. The non-adaptive control scheme and both adaptive methods
proposed earlier were incorporated in the construction, all with the same nomi-
nal dynamics, so that direct comparisons among the three could be performed.
These systems were subjected to changes in load, input voltage, and output
capacitance, with their dynamic characteristics being monitored by observa-
tions of the output voltage response to a step change in load resistance. As ex-
pected, the conventional, non-adaptive regulator displayed excessive sensitivity
to all these variations. When current-sensing adaptive control was employed,
great reductions were evident in the sensitivities to changes in input voltage and
load, but no benefits were observed in the case of altered output capacitance.
Finally, the more sophisticated current-and-capacitance-sensing method suc-
ceeded in preserving the nominal behavior of the regulator in the face of all
these variations.

Thus, the adaptive strategies introduced in this final part of this thesis have
been shown to be of great potential value in the design of switching regulators.
The increase in allowable operating region they bestow on high-performance sys-
tems should enable switching regulators to offer an even more attractive combi-
nation of efficiency and performance than they presently enjoy. Such improve-
ment would undoubtedly lead to more extensive use of switching regulators in
engineering technology.

CONCLUSION

It was mentioned in the Introduction to this thesis that the three corner-stones of engineering, analysis, measurement, and design, also form the founda-tions of this thesis and that, just as occurs in engineering, the three become in-terdependent in this work's development. In retrospect, it is possible to see more clearly how this fusion came about.

Initially, the problem was to explain the high-frequency behavior of switching regulators. Analysis was the dominant component in this endeavor, both in the comparison of the derivations and predictions of the existing modeling tech-niques, discrete and state-space averaged modeling, and in the creation of a new method, the sampled-data model, which combines the accuracy of the discrete modeling technique with the continuous form of state-space averaging.

With the development of this new model, the interpretation of high-frequency loop gain measurements became possible, and was the next topic to be ad-dressed. Thus, the concept of measurement dominated the second part of this thesis. Simultaneously, analysis continued to play an important role in the in-terpretation of the measurements. Through this interplay between analysis and measurement, it was found that various techniques for the measurement of loop gains in switching regulators differ in their utilities for regulator design. The most common type of closed-loop loop gain measurement was shown to yield a result which is different from the predictions previously formulated but which is nevertheless useful for the prediction of system stability.

The focus of attention shifted yet again after this investigation and now rest-ed on the problem of the sensitivity of the dynamic behavior of high-performance switching regulators to changes in operating condition. Here

analysis and measurement both played essential parts, but the dominant component was clearly design. The application of adaptive control to reduce excessive sensitivity was introduced and was shown to yield substantial benefits in these high-performance systems. The interdependence of the three basic processes in this development is illustrated by the use of analysis to uncover the dependencies of loop gain on operating condition and the employment of measurements to confirm the superior performance of the adaptive designs.

Thus, each part of this thesis has marked the introduction of one of these three components of the engineering process, while the previously introduced processes continued to play a vital role. In this sense, this thesis, and the process of engineering as a whole, can be likened to the musical form known as the fugue. The various voices in such a piece enter one at a time, proclaiming the theme. Then, as new voices are introduced, those already present continue to develop the theme and support one another, until the development is complete. In engineering, the theme is the problem to be solved, the voices are the analysis, measurement, and design processes, and the development is completed when the problem is solved. It is the interplay of these three components that leads to the solution, just as the interplay of the musical voices develops the theme of the fugue. Beauty resides in both.

APPENDICES

APPENDICES

The three Appendices attached to this thesis provide background and derivations of important results which are used in this work. The subjects addressed in these sections are the properties of the z-transform, the application of the Laplace transform to sampled-data systems, and the relation between the z-transform and the Laplace transform descriptions of a sampling system.

Appendix A provides a brief presentation of the definition and important properties of the one-sided z-transform employed in this thesis. Also, interpretations of several simple z-transforms are given, in order to provide some "feel" for this important tool.

The properties of the Laplace transforms of sampled functions are discussed in Appendix B, which is probably the most technical discussion of this thesis. This Appendix is divided into two unequal parts. The first, and by far the longest, section defines the Laplace transform of a sampled function and evaluates this transform in three different but equivalent ways. The second part demonstrates that the sampling operation does not affect the transform of a previously sampled signal.

Finally, in Appendix C, a connection is made between the first two Appendices. Specifically, for a sampled function, a transformation is derived which relates the z-transform of the waveform to the Laplace transform of the same function.

APPENDIX A

ONE-SIDED Z-TRANSFORMS

A.1 Definition and properties of one-sided z-transforms

For a sequence of numbers $x(n)$, $n = ..., -1, 0, +1, ...$, define the one-sided z-transform $Z[x(n)]$.

$$Z[x(n)] = X(z) = \sum_{n=0}^{\infty} x(n) z^{-n} \qquad \text{(A.1a)}$$

$$= x(0) + x(1)z^{-1} + x(2)z^{-2} + ... \qquad \text{(A.1b)}$$

Linearity is obvious.

$$Z[ax(n) + by(n)] = aX(z) + bY(z) \qquad \text{(A.2a)}$$

$$Z[x(n)] = X(z) , \quad Z[y(n)] = Y(z) \qquad \text{(A.2b)}$$

A shift rule for this z-transform is also easily established.

$$Z[x(n+1)] = x(1) + x(2)z^{-1} + x(2)z^{-2} + ... \qquad \text{(A.3a)}$$

$$= z\{Z[x(n)] - x(0)\} \qquad \text{(A.3b)}$$

A.2 Examples of z-transforms

An analysis of some simple examples of z-transforms can aid in the extraction of content from this important tool.

$$X(z) = \frac{1}{z - a} = \frac{z^{-1}}{1 - z^{-1}a} \qquad \text{(A.4a)}$$

$$= z^{-1}(1 + az^{-1} + a^2z^{-2} + \ldots) \qquad \text{(A.4b)}$$

The sequence corresponding to this transform can be written down directly.

$$x(n) = \{0, 1, a, a^2, \ldots\} \qquad \text{(A.5)}$$

Examination of this sequence for various choices of the pole position a provides an interpretation of the transform.

Cases	
$\|a\| < 1$	decaying sequence, stable
$\|a\| > 1$	growing sequence, unstable
$a = -1$	subharmonic oscillation $\{1,-1,1,-1,\ldots\}$
$a = 0$	finite sequence ("finite settling time")

APPENDIX B

LAPLACE TRANSFORMS OF SAMPLED SIGNALS

B.1 Evaluation of sampled Laplace transforms

Consider a function $v(t)$ with associated Laplace transform $V(s)$. Passage of this waveform through a sampler with period T_s gives a string of delta functions.

$$v^*(t) = v(t) T_s \delta_{T_s}(t) \tag{B.1a}$$

$$\delta_{T_s}(t) = \sum_{n=-\infty}^{\infty} \delta(t - nT_s) \tag{B.1b}$$

The problem is to evaluate the Laplace transform $V^*(s) = L\{v^*(t)\}$ associated with $v^*(t)$. There are several ways to proceed [11], and three different approaches will be discussed in this Appendix.

The first method works with the time domain representation of $v(t)$.

$$L\{v^*(t)\} = L\left\{ \sum_{n=-\infty}^{\infty} v(nT_s) T_s \delta(t - nT_s) \right\} \tag{B.2a}$$

$$= T_s \sum_{n=-\infty}^{\infty} v(nT_s) L\{\delta(t - nT_s)\} \tag{B.2b}$$

The first step follows from the nature of the delta function, while in the second, it is assumed that the summation and integration operations can be interchanged. The Laplace transform of a delta function is trivial.

$$L\{\delta(t - nT_s)\} = \begin{cases} 0 & n < 0 \\ e^{-snT_s} & n \geq 0 \end{cases} \tag{B.3}$$

The result is the sampled-data Laplace transform wherever the series converges.

$$V^{\bullet}(s) = T_s \sum_{n=0}^{\infty} v(nT_s)e^{-snT_s} \tag{B.4}$$

The evaluation method just discussed used the time domain representation of v. Other methods use the Laplace transform of v instead. In these techniques, the complex multiplication theorem for Laplace transforms, the counterpart of the convolution theorem, is applied to the defining relation, Eq. (B.1). The transform of the picket-fence function $\delta_{T_s}(t)$ is easy to find.

$$L\{\delta_{T_s}(t)\} = \frac{1}{1 - e^{-sT_s}} \tag{B.5}$$

Then the complex multiplication theorem gives an integral representation for the Laplace transform of $v^{\bullet}(t)$.

$$V^{\bullet}(s) = \frac{T_s}{2\pi j} \int_{c-j\infty}^{c+j\infty} \frac{V(p)}{1-e^{-(s-p)T_s}} dp \quad , \quad 0 < c < Re(s) \tag{B.6}$$

The contour is shown in Fig. (B.1). The poles of $V(p)$ depend on the form of $v(t)$, and are assumed to lie in the left-half p-plane. The poles of the integrand are all simple, and satisfy the following equation.

$$s - p = j\frac{2\pi n}{T_s} \tag{B.7a}$$

$$p = s + j\frac{2\pi n}{T_s} = s + jn\omega_s \tag{B.7b}$$

The integral in Eq. (B.6) can be evaluated in two different ways, corresponding to
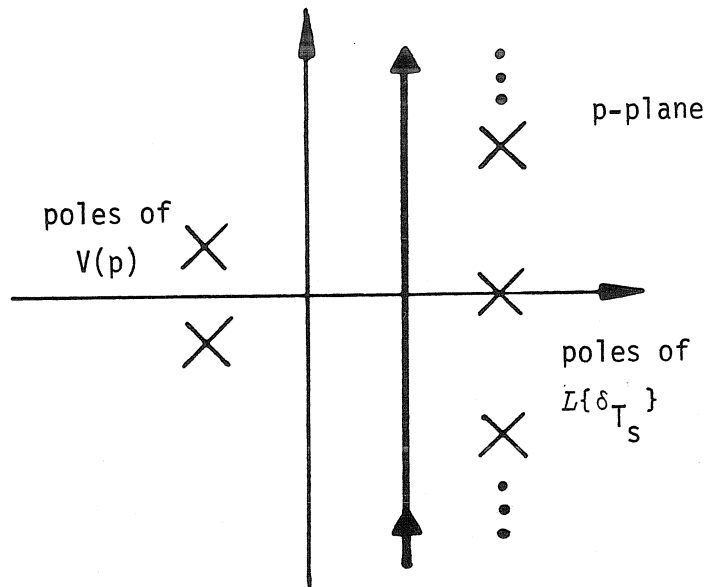
Figure B.1. *Basic contour for the sampled Laplace transform integral.*
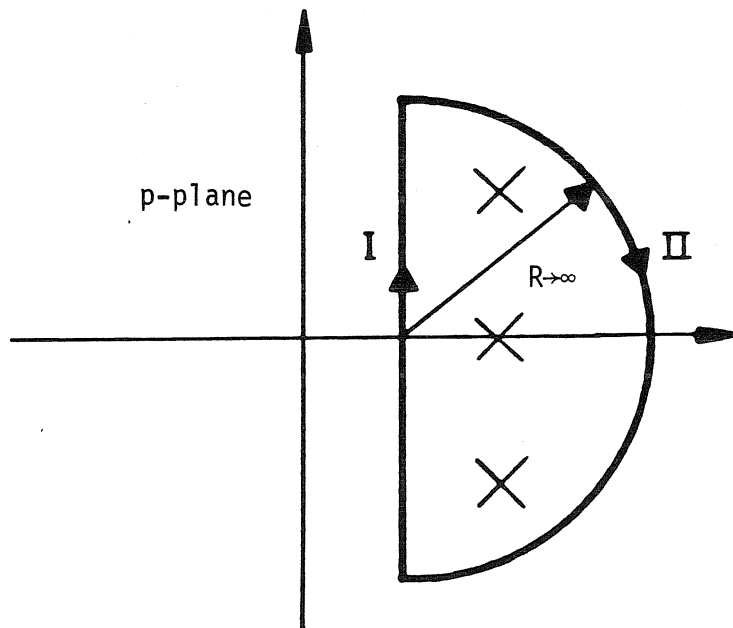
Figure B.2. *One choice of a closed contour for the evaluation of the sampled Laplace transform.*

two possibilities for the formation of a closed contour for the integration.

For the first possibility, consider the contour shown in Fig. (B.2).

$$V^{\circ}(s) = \frac{T_s}{2\pi j} \int_{\substack{I+II \\ R \to \infty}} \frac{V(p)}{1 - e^{-(s-p)T_s}} dp \; - \; \frac{T_s}{2\pi j} \int_{\substack{II \\ R \to \infty}} \frac{V(p)}{1 - e^{-(s-p)T_s}} dp \qquad (B.8)$$

Provided the contribution from poles outside the contour $I+II$ grows arbitrarily small as $R \to \infty$, so that the first integral converges, and provided the contribution from the second integral vanishes as $R \to \infty$, the following equation holds.

$$V^{\circ}(s) = -T_s \sum_{\substack{\text{poles within} \\ \text{contour}}} \left(\text{residue of } \frac{V(p)}{1-e^{-(s-p)T_s}} \right) \qquad (B.9)$$

Since the poles are simple, the residues are easy to find.

$$\left. \frac{V(p)}{\frac{d}{dp}[1-e^{-(s-p)T_s}]} \right|_{p=s+jn\omega_s} = \frac{1}{T_s} V(s+jn\omega_s) \qquad (B.10)$$

The first integral is thus reduced to a summation.

$$\frac{T_s}{2\pi j} \int_{I+II} = \sum_{n=-\infty}^{\infty} V(s+jn\omega_s) \qquad (B.11)$$

The contribution from the semi-circular path II must still be considered. With the use of a substitution, this integral can be rewritten.

$$p = Re^{j\vartheta} \qquad \frac{\pi}{2} > \vartheta > -\frac{\pi}{2} \qquad dp = jRe^{j\vartheta}d\vartheta \qquad (B.12)$$

$$-\frac{T_s}{2\pi j}\int_I = -\lim_{R\to\infty}\frac{T_s}{2\pi}\int_{\frac{\pi}{2}}^{-\frac{\pi}{2}}\frac{V(Re^{j\vartheta})Re^{j\vartheta}}{1-e^{RT_s\cos\vartheta}e^{jRT_s\sin\vartheta}e^{-sT_s}}d\vartheta \qquad (B.13a)$$

$$= \lim_{R\to\infty}\frac{T_s}{2\pi}\int_{\frac{\pi}{2}}^{-\frac{\pi}{2}}\frac{V(Re^{j\vartheta})Re^{j\vartheta}}{e^{RT_s\cos\vartheta}e^{jRT_s\sin\vartheta}e^{-sT_s}}d\vartheta \qquad (B.13b)$$

The last equality follows because the sign of $\cos\vartheta$ is positive. This integral will vanish if the integrand goes to zero as $R\to\infty$.

$$\left.\frac{V(Re^{j\vartheta})R}{e^{RT_s\cos\vartheta}}\right|_{-\frac{\pi}{2}<\vartheta<\frac{\pi}{2}} \to 0 \qquad \text{as } R\to\infty \qquad (B.14)$$

Again, since $\cos\vartheta > 0$ in this range, this condition holds for all $V(s)$ normally encountered. The final result can now be written.

$$V^\bullet(s) = \sum_{n=-\infty}^{\infty} V(s+jn\omega_s) \qquad (B.15)$$

Of course, the sum must converge for this statement to have meaning.

The technique just discussed simplified Eq. (B.6) by the closure of the integration contour on the right. Conversely, the third method of evaluating the sampled Laplace transform involves the closing of this contour on the left, as shown in Fig. B.3. A formula similar to Eq. (B.8) now applies.

$$V^\bullet(s) = \frac{T_s}{2\pi j}\int_{\substack{I+III\\R\to\infty}}\frac{V(p)}{1-e^{-(s-p)T_s}}dp - \frac{T_s}{2\pi j}\int_{\substack{III\\R\to\infty}}\frac{V(p)}{1-e^{-(s-p)T_s}}dp \qquad (B.16)$$

The contour now encloses the poles of $V(p)$.
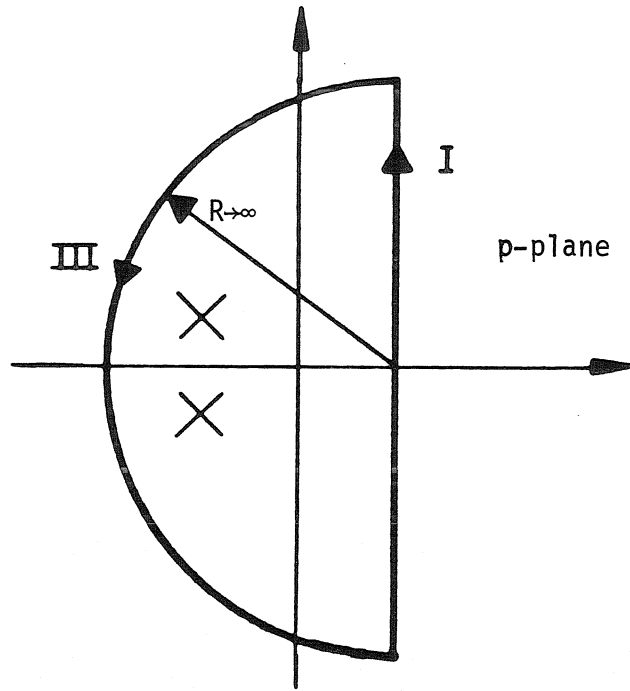
Figure B.3. *Another choice of a closed contour for the evaluation of the sampled Laplace transform.*
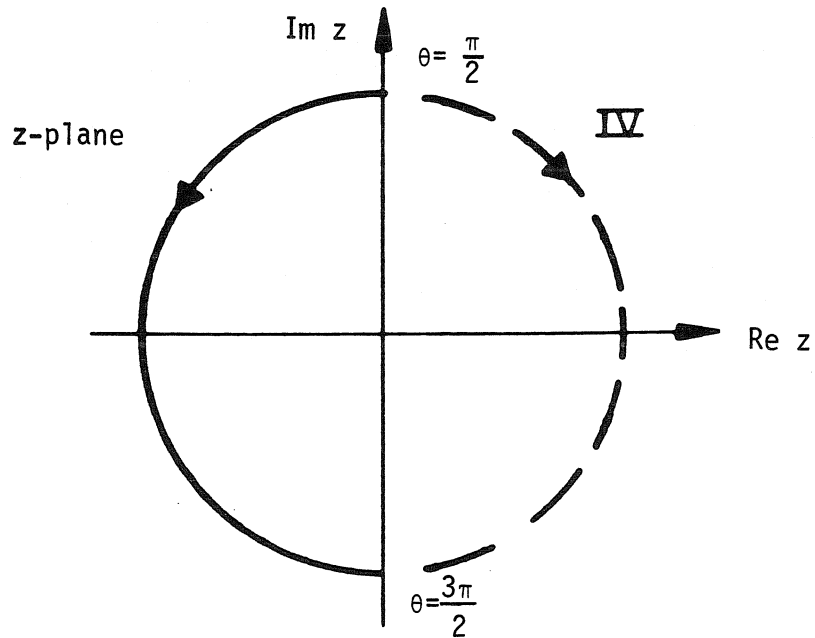
Figure B.4. *Contour for the evaluation of the quantity I.*

$$\frac{T_s}{2\pi j}\lim_{R\to\infty}\int_{I+III} = T_s \sum_{\substack{\text{poles } s_n \\ \text{of } V(s)}}\left(\text{residue of }\frac{V(p)}{1-e^{-(s-p)T_s}}\right)_{p=s_n} \tag{B.17}$$

The integral on the semicircular segment of the contour is evaluated with use of the same substitution as employed earlier.

$$p = Re^{j\vartheta} \quad \frac{\pi}{2} < \vartheta < \frac{3\pi}{2} \quad dp = jRe^{j\vartheta}d\vartheta \tag{B.18}$$

$$\lim_{R\to\infty}-\frac{T_s}{2\pi j}\int_{III} = \lim_{R\to\infty}-\frac{T_s}{2\pi}\int_{\frac{\pi}{2}}^{\frac{3\pi}{2}}\frac{V(Re^{j\vartheta})Re^{j\vartheta}}{1-e^{RT_s\cos\vartheta}e^{jRT_s\sin\vartheta}e^{-sT_s}}d\vartheta \tag{B.19a}$$

$$= \lim_{R\to\infty}-\frac{T_s}{2\pi}\int_{\frac{\pi}{2}}^{\frac{3\pi}{2}}V(Re^{j\vartheta})Re^{j\vartheta}d\vartheta \tag{B.19b}$$

The last step is possible owing to the behavior of the function $e^{RT_s\cos\vartheta}$, $\frac{\pi}{2} < \vartheta < \frac{3\pi}{2}$, as R gets large. A third formula is thus uncovered for the Laplace transform of $v^*(t)$, valid when the summation and integral converge.

$$V^*(s) = T_s \sum_{\substack{\text{poles } s_n \\ \text{of } V(s)}}\left(\text{residue of }\frac{V(p)}{1-e^{-(s-p)T_s}}\right)_{p=s_n}$$

$$- \lim_{R\to\infty}\frac{T_s}{2\pi}\int_{\frac{\pi}{2}}^{\frac{3\pi}{2}}V(Re^{j\vartheta})Re^{j\vartheta}d\vartheta \tag{B.20}$$

Unlike the previous case, however, the integral over the semicircular contour cannot, in general, be neglected. A special case of this third formula, of great interest in this thesis, is now discussed. Suppose that $V(s)$ represents a (possibly multiple) integrator, with an additional small delay ε.

$$V(s) = \frac{e^{-\varepsilon s}}{s^m} \quad , \qquad \varepsilon > 0 \ , \quad m = 1, 2, \ldots \qquad (B.21)$$

The integral in Eq. (B.20), which will be denoted I, can then be evaluated.

$$I = \lim_{R \to \infty} \left(-\frac{T_s}{2\pi} \int_{\frac{\pi}{2}}^{\frac{3\pi}{2}} \frac{e^{-\varepsilon R \cos\vartheta} e^{-j\varepsilon R \sin\vartheta} R e^{j\vartheta}}{R^m (e^{j\vartheta})^m} d\vartheta \right) \qquad (B.22)$$

Since $\varepsilon > 0$, this integral does not necessarily vanish. It can be investigated by the construction of yet another closed contour and substitution, illustrated in Fig. B.4.

$$z = e^{j\vartheta} \ , \qquad dz = j e^{j\vartheta} d\vartheta \qquad (B.23)$$

$$I = \lim_{R \to \infty} \left(-\frac{T_s}{2\pi j} \frac{1}{R^{m-1}} \int_{|z|=1} \frac{e^{-\varepsilon R z}}{z^m} dz + \frac{T_s}{2\pi j} \frac{1}{R^{m-1}} \int_{IV} \frac{e^{-\varepsilon R z}}{z^m} dz \right) \qquad (B.24)$$

On path IV, $e^{-\varepsilon R z} \to 0$ as $R \to \infty$, so this portion vanishes.

$$I = \lim_{R \to \infty} -\frac{T_s}{2\pi j} \frac{1}{R^{m-1}} \int_{|z|=1} \frac{e^{-\varepsilon R z}}{z^m} dz \qquad (B.25)$$

The only pole in the remaining integral is one of order m at the origin. The integral is evaluated by residue theory.

$$I = -\lim_{R \to \infty} \frac{T_s}{R^{m-1}} \frac{1}{(m-1)!} \frac{d^{m-1}}{dz^{m-1}} (e^{-\varepsilon R z}) \bigg|_{z=0} \qquad (B.26)$$

The differentiation is easily carried out.

$$I = \begin{cases} T_s & \text{if } m=1 \\ \dfrac{(-\varepsilon)^{m-1}}{(m-1)!} T_s & \text{if } m > 1 \end{cases} \qquad (B.27)$$

To summarize, this quantity I is a term in the sampled Laplace transform $V^\circ(s)$ for a special case of the unsampled transform $V(s)$.

$$V(s) = \frac{e^{-\varepsilon s}}{s^m} \qquad (B.28a)$$

$$V^\circ(s) = T_s \sum_{\substack{\text{poles } s_n \\ \text{of } V(s)}} \left(\text{residue of } \frac{V(p)}{1-e^{-(s-p)T_s}} \right)_{p=s_n} - I \qquad (B.28b)$$

Note that for $m > 1$, the additional term I vanishes in the limit $\varepsilon \to 0$, but that it does not vanish for $m=1$. Physically, this difference occurs because a step function, the time representation when $m=1$, results in a non-zero output from a sampler as soon as the step is applied to the sampler, while the higher-order polynomials occurring when $m > 1$ do not. The addition of a small delay eliminates this instantaneous propagation of a step function and consequently changes the sampled Laplace transform by the quantity I. Because of the slow rises of the higher-order polynomials corresponding to $m > 1$, the delay has no effect on the sampled Laplace transforms in these cases. In the context of the sampled-data modeling technique, this delay assures that no instantaneous propagation around a switching regulator's feedback loop can occur, thus guaranteeing causality. The sampled Laplace transform for the case where $m=1$ is used extensively in this thesis and is easily evaluated from the above equations.

$$V(s) = \frac{e^{-es}}{s} \tag{B.29a}$$

$$\lim_{e \to 0} V^*(s) = T_s \left(\frac{1}{1 - e^{-sT_s}} - 1 \right) = \frac{T_s}{e^{sT_s} - 1} \tag{B.29b}$$

B.2 Effect of the application of sampling to a previously sampled signal

It is shown in the following demonstration that a sampled Laplace transform can be factored out of any additional sampling operation, provided that the samplers are synchronous.

$$[A(s)B^*(s)]^* = \sum_{n=-\infty}^{\infty} A(s + jn\omega_s)B^*(s + jn\omega_s) \tag{B.30}$$

This first step uses the second expression for the sampled Laplace transform found in Section B.1. The second sampled transform is now expanded.

$$[A(s)B^*(s)]^* = \sum_{n=-\infty}^{\infty} A(s + jn\omega_s) \sum_{m=-\infty}^{\infty} B(s + jn\omega_s + jm\omega_s) \tag{B.31}$$

This expression is readily factored by substituted $l = m + n$.

$$[A(s)B^*(s)]^* = \sum_{n=-\infty}^{\infty} A(s + jn\omega_s) \sum_{l=-\infty}^{\infty} B(s + jl\omega_s) = A^*(s)B^*(s) \tag{B.32}$$

This result is used several times in Part I of this thesis.

APPENDIX C

RELATIONSHIP BETWEEN THE Z-TRANSFORM

AND THE SAMPLED LAPLACE TRANSFORM

Consider a time function $u(t)$ with Laplace transform $U(s)$. Suppose this function is passed through a sampler with period T_s, as defined in Appendix B.

$$u^*(t) = u(t)T_s\delta_{T_s}(t) = u(nT_s)T_s\delta_{T_s}(t) \tag{C.1a}$$

$$\delta_{T_s}(t) = \sum_{n=-\infty}^{\infty} \delta(t-nT_s) \tag{C.1b}$$

In Appendix B, three expressions for the Laplace transform $U^*(s)$ of this sampled signal were developed. The first of these is particularly useful here.

$$U^*(s) = T_s \sum_{n=0}^{\infty} u(nT_s)e^{-sT_s n} \tag{C.2}$$

The sampled values $T_s u(nT_s)$ in this equation are a sequence of numbers, and it is therefore possible to form a z-transform of the sampled function $u^*(t)$.

$$Z[u^*(t)] = U_z(z) = \sum_{n=0}^{\infty} T_s u(nT_s)z^{-n} \tag{C.3}$$

Comparison of Eqs. (C.2) and (C.3) reveals the relationship between the Laplace transform of a sampled function and the z-transform of the same function.

$$U^*(s) = U_z(z = e^{sT_s}) \tag{C.4}$$

In particular, the poles s_p of $U^*(s)$ are related to the poles z_p of $U_z(z)$ by a

simple relation.

$$z_p = e^{s_p T_s}$$

(C.5)

This correspondence is invoked in Chapter 7 in the comparison of the discrete and sampled-data modeling techniques.

REFERENCES

[1] Slobodan Ćuk, "Modelling, Analysis, and Design of Switching Regulators," PhD thesis, California Institute of Technology, November 1976; also, NASA Report CR-135174.

[2] Dennis J. Packard, "Discrete Modeling and Analysis of Switching Regulators," PhD thesis, California Institute of Technology, May 1976; also, Report No. M76-43, Hughes Aircraft Co., Aerospace Groups, Culver City, Calif.

[3] Slobodan Ćuk and R. D. Middlebrook, "A New Optimum Topology Switching Dc-to-Dc Converter," IEEE Power Electronics Specialists Conference, 1977 Record, pp. 160-179 (IEEE Publication 77CH1213-8 AES).

[4] Shi-Ping Hsu, Art Brown, Loman Rensink, and R. D. Middlebrook, "Modelling and Analysis of Switching Dc-to-Dc Converters in Constant-Frequency Current-Programmed Mode," IEEE Power Electronics Specialists Conference, 1979 Record, pp. 284-301 (IEEE Publication 79CH1416-3 AES).

[5] Cecil W. Deisch, "Simple Switching Control Method Changes Power Converter into a Current Source," IEEE Power Electronics Specialists Conference, 1978 Record, pp. 300-306 (IEEE Publication 78CH1337-5 AES).

[6] A. Capel, G. Ferrante, D. O'Sullivan, and A. Weinberg, "Application of the Injected Current Model for the Dynamic Analysis of Switching Regulators with the New Concept of LC^3 Modulator," IEEE Power Electronics Specialists Conference, 1978 Record, pp. 135-147 (IEEE Publication 78CH1337-5 AES).

[7] R. D. Middlebrook, "Modelling and Design of the Ćuk Converter," Proc. Sixth National Solid-State Power Conversion Conference (Powercon 6), pp. G3.1-G3.14, May 1979.

[8] Slobodan Ćuk and Robert W. Erickson, "A Conceptually New High-Frequency Switched-Mode Amplifier Technique Eliminates Current Ripple," Proc. Fifth National Solid-State Power Conversion Conference (Powercon 5), pp. G3.1-G3.22, May 1978.

[9] W. M. Polivka, P. R. K. Chetty, and R. D. Middlebrook, "State-Space Average Modelling of Converters with Parasitics and Storage-Time Modulation," IEEE Power Electronics Specialists Conference, 1980 Record, pp. 119-143 (IEEE Publication 80CH1529-7).

[10] Loman Rensink, Art Brown, Shi-Ping Hsu, and Slobodan Ćuk, "Design of a Kilowatt Off-Line Switcher Using a Ćuk Converter," Proc. Sixth National Solid-State Power Conversion Conference (Powercon 6), pp. H3.1-H3.26, May 1979.

[11] Eliahu I. Jury, *Sampled-Data Control Systems*, John Wiley & Sons, 1958.

[12] R. D. Middlebrook, "Measurement of Loop Gain in Feedback Systems," International J. of Electronics, vol. 38, no. 4, pp. 485-512, April 1975.

[13] R. D. Middlebrook, "Improved-Accuracy Phase Angle Measurement," International J. of Electronics, vol. 40, no. 1, pp. 1-4, Jan. 1976.

[14] Farhad Barzegar, Slobodan Ćuk, and R. D. Middlebrook, "Using Small Computers to Model and Measure Magnitude and Phase of Regulator Transfer Functions and Loop Gain," Proc. Eighth National Solid-State Power Conversion Conference (Powercon 8), pp. H1.1-H1.28, April 1981.